Multilevel Modeling Techniques for Time Domain Analysis of Microwave and High Speed Circuits

by

Huilian Du
B.Eng., Harbin Institute of Technology, China, 1988
M.S., Harbin Institute of Technology, China, 1991

A Dissertation Submitted in Partial Fulfillment of the
Requirements for the Degree of

DOCTOR OF PHILOSOPHY

In the Department of Electrical and Computer Engineering

SUPERVISORY COMMITTEE

Multilevel Modeling Techniques for Time Domain Analysis of Microwave and High Speed Circuits

by

Huilian Du
B. Eng., Harbin Institute of Technology, 1988
M. S., Harbin Institute of Technology, 1991

Dr. Wolfgang J. R. Hoefer,

Supervisor, Department of Electrical and Computer Engineering

Dr. Jens Bornemann

Departmental Member, Department of Electrical and Computer Engineering

Dr. Poman So

Departmental Member, Department of Electrical and Computer Engineering

Dr. Rodney Herring

Outside Member, Department of Mechanical Engineering

Supervisory Committee

Dr. Wolfgang J. R. Hoefer
Supervisor

Dr. Jens Bornemann
Departmental Member

Dr. Poman So
Departmental Member

Dr. Rodney Herring
Outside Member

ABSTRACT

Numerical methods are very important in the areas of microwave and RF engineering, antenna design, bio-electromagnetics, electromagnetic compatibility and interference (EMC/EMI). Among several techniques, time domain methods such as the Finite Difference Time Domain (FDTD) method and the Transmission Line Matrix (TLM) method are of particular interest, due to their high flexibility and ease of implementation, given the powerful computation resource available.

This dissertation is focused on the TLM method, a discrete time evolution scheme, based on the analogy between the discretized electromagnetic field and a mesh of transmission lines. Generally, in a numerical method, much effort is spent on reducing the computational burden, increasing the ability and flexibility to handle hybrid problems and to model various properties of materials. The objective of the proposed research is to a) develop, implement, and test several techniques aimed at enhancing the accuracy of time domain analysis of microwave and high speed circuits without increasing the computational load, b) to develop methods to embed circuits and devices into a field environment or to import field analysis into a circuit simulator, and c) enhance the modeling of a wide range of materials, including metamaterials with negative refractive index, and magnetized ferrites.

By making good use of these techniques it is possible to incorporate more information into the TLM solution, thus enabling more accurate, more efficient and more powerful CAD tools for industry and academia.

Table of Contents

List of Tables

List of Figures

List of Symbols

Symbols

c	speed of light
f	frequency
ω	angular frequency
t	time
ε	absolute permittivity
ε_0	permittivity of free space
ε_m	permittivity of medium
ε_r	relative permittivity
k	wave number or propagation constant (when used in the context of wave functions)
k	integer designating the number of time steps in a simulation (when used in the context of discrete time domain algorithms)
μ	absolute permeability
μ_0	permeability of free space
μ_m	permeability of medium
μ_r	relative permeability
$\Delta\ell$	mesh parameter or cell size
Δt	time step
[S]	scattering matrix
[C]	connecting matrix
$v_{\ell 0}$	phase velocity on TLM link lines
$Z_{\ell 0}$	characteristic impedance of TLM link line
$Y_{\ell 0}$	characteristic admittance of TLM link line
$\lambda_{\ell 0}$	wavelength along the link line
$\beta_{\ell 0}$	phase constant along the link line
$\alpha_{\ell 0}$	attenuation constant along the link line
v_m	phase velocity in TLM network
Z_m	characteristic impedance of TLM network or medium
Y_m	characteristic admittance of TLM network or medium
λ_m	wavelength in TLM network or medium
β_m	phase constant in TLM network or medium
α_m	attenuation constant in TLM network or medium
Z_0	characteristic impedance of free space
Y_0	characteristic admittance of free space
λ_0	wavelength in free space
V	voltage
C	capacitance
L	inductance
Z_ℓ	characteristic impedance of the stub representing an inductance
Z_c	characteristic impedance of the stub representing a capacitance
Z_s	series impedance
C_s	series capacitance
L_s	series inductance

Y_p	parallel admittance	H	magnetic field intensity
C_p	parallel capacitance	**E**	electric field vector
L_p	parallel inductance	**H**	magnetic field vector
E	electric field intensity		

Common Abbreviations

RF	Radio Frequency
TLM	Transmission Line Matrix
FDTD	Finite Difference Time Domain
2D	Two-Dimensional
3D	Three-Dimensional
ABC	Absorbing Boundary
SCN	Symmetrical Condensed Node
TEM	Transverse Electromagnetic
TE	Transverse Electric
TM	Transverse Magnetic
SPICE	Simulation Program with Integrated Circuits Emphasis
PSPICE	A PC version of SPICE (from MicroSim Corporation)
ABM	Analog Behavioral Model
A/D	Analog/Digital
S-parameters	Scattering parameters (Complex ratio of power waves incident and reflected at ports of microwave networks).

Acknowledgments

I would like to express my sincere thanks and heartfelt gratitude to all of the people who have helped me to complete this important part of my education and shared this experience with me.

I wish to express my gratitude to my supervisor, Prof. Wolfgang J. R. Hoefer for his tireless guidance, support and thoughtful advice throughout these years, for encouraging me during the difficult times, and for sharing with me the exciting times. I am grateful for his perseverance through the revisions and reviews. His caring attitude, both in academic and personal matters, contributed greatly not only to this work, but also to my personal development.

I would like to thank Prof. Jens Bornemann, whose presence throughout the tenure of my studies has been of great value.

I wish to express my special acknowledgments to Prof. Poman P.M. So for his precious suggestions and discussions during my studies, and his thoughtful help in all other aspects of my life at UVic.

I would like to thank Prof. Rodney Herring for his precious suggestions and time on my thesis.

My sincere thanks go to Ms. Donna Shannon, Ms. Roanna Chiu, Dr. Kris Caputa, Mr. Muhammad Zulfiker Alam, Dr. Rambabu Karumudi, Mr. Seng Young Yu, Ms. Marjan Mokhtaari, Mr. Douglas Henke, Dr. Hong Son Chu, Dr. Hongnian Wang and Dr. Jinye Zhang for their friendship, help and inspiring discussions, ideas and suggestions.

Many thanks to my friends who made my stay in Victoria pleasurable and memorable: Demin Tang and her family, Yue Wang, Guiyun Li, Jun Li, Ping Wan …

Last but not least, my heartfelt acknowledgments go to my family for loving, understanding and encouraging me to pursue my dreams.

Dedication

To my parents, husband and son

Chapter 1

Introduction

1.1 Motivation

The design of modern high performance electronic components and systems such as waveguide structures, digital signal interconnections, RF circuits and systems, requires careful attention to physical modeling. In this way, the intrinsic physical limitations of implementation processes can be accounted for, and undesirable effects such as substrate coupling, signal integrity problems, electromagnetic interference (EMI), and metallic edge effects can be minimized. A high degree of physical fidelity of the models is necessary and can only be achieved by detailed analysis employing electromagnetic field solvers. The time domain Transmission Line Matrix (TLM) method has proven to be a powerful tool for solving electromagnetic field problems and has been successfully applied to the analysis of various complicated planar and general three-dimensional structures[1].

The design of complex systems operating at high frequencies or clock rates requires that the design and analysis tools can handle circuit and field analysis at the same time since the designed system may include a combination of lumped circuits, transmission line components such as couplers, power dividers, interconnections, and waveguide components that may contain field singularities due to metallic sharp edges or corners. The field analysis of such a hybrid system is a difficult task for a space and time discrete numerical method like Finite Difference Time Domain (FDTD) or TLM method. The challenges for such a field solver lie in the following aspects: (1) it must have an embedding feature to connect lumped circuits to the field model, (2) it must be able to efficiently handle singularities to increase the accuracy and decrease the computational burden, (3) it must possess the ability to model complex material properties since the

transmission line and waveguide components may contain a variety of materials such as regular dielectrics, metamaterials, and ferrites, to name a few, (4) it must have the ability to extract circuit models from field simulation results of a substructure for inclusion into a circuit solver. To address these needs, multilevel modeling techniques, with TLM as the underlying time domain field modeling engine [10-14], have thus been developed.

These techniques can minimize the computational burden without decreasing the solution accuracy when tackling field singularities. Furthermore, the techniques have the ability to deal with hybrid problems containing lumped element circuits and distributed components as well as a wide range of material properties which include materials with negative permeability and permittivity or frequency dependent properties, such as metamaterials and magnetized ferrites.

1.2 Original contributions

The following original contributions to the enhancement of the TLM method in time domain analysis of microwave and high speed circuits are described in this dissertation:

- *Singularity correction in TLM (pages 18 to 29)*

  This robust and efficient approach deals with electromagnetic problems involving field singularities at sharp metallic edges and 90° corners. In this approach the permittivity and permeability of the cells adjacent to the singularity are modified by a scalar correction factor, which amounts to a quasi-static correction of the electric and magnetic energy stored in the TLM cells at the singularity. This correction is equally effective for TE-, TM- and hybrid field excitations of the singularity. Resonant frequency computations incorporating this correction procedure have been compared with data obtained with the regular TLM method. The comparison shows that the correction method reduces the singularity error by typically one order of magnitude without penalty in terms of computational burden. The effectiveness of the method for the accurate computation of structures with metallic strips (knife edges) or 90° edges and corners has been clearly demonstrated and is applicable to both homogeneous and inhomogeneous material properties in the singularity region.

- *Embedding of Current-Coupled Lumped Networks in TLM Models (pages 30 to 40)*

A modeling framework for embedding current-coupled lumped networks into time-domain TLM field models has been developed. The connection algorithm is based on the representation of the TLM network by equivalent Norton current sources. This framework complements the existing voltage-coupled methodology and is suitable for integrating general n-port lumped circuits into 3D field space. The lumped circuit can be modeled by state-space equations or by means of circuit solvers such as SPICE. A procedure for embedding current-coupled lumped networks into three-dimensional TLM field models has been developed, implemented and tested. The current-coupled embedding would be preferable in situations where terminal voltages cannot be defined in a unique way, but current flowing into a terminal is uniquely defined. This current-controlled embedding methodology is quite flexible and does not require the definition of a reference potential within the field model.

- *Analog Behavioral Module Linking TLM and PSPICE for Transient Analysis (pages 40 to 48)*

A new Analog Behavioral Module (ABM) for two-port networks characterized by frequency domain Scattering parameters (henceforth abbreviated as S-parameters) has been described. The proposed module has been implemented in the PSPICE environment for transient circuit simulation. The accuracy of this model has been validated by comparing the simulation results obtained with the ABM model and with the original circuit. This approach can be used to build field-based device models for SPICE-based circuit simulators without unwanted time-domain signal distortion. It is very useful for modeling of complex systems containing components represented at various levels, such as lumped circuits, distributed components and field-based models.

- *Inter-cell Network Framework in TLM (pages 49 to 63)*

The inter-cell network framework which allows embedding linear and nonlinear lumped or distributed elements in field space has been developed; this framework can model material properties without modifying the node scattering matrix. Traditionally, material properties are introduced in TLM by modifying the scattering procedure at the nodes. The inter-cell network framework is an alternative approach in which the

material properties are introduced in the connection phase of the TLM algorithm. This is realized by the insertion of an inter-cell network scattering feature. Its properties can be described by various means, such as equivalent circuits, differential equations, behavioral models, experimental data, or even nonlinear SPICE modules.

- *Metamaterial Modeling using the 3D-TLM SCN Node (pages 64 to 93)*

  Inter-cell network scattering matrices for 3D TLM modeling of the following materials, boundaries and interfaces have been developed:

  - Homogeneous metamaterials,
  - Metamaterials bounded by electric, magnetic and absorbing boundaries,
  - Interfaces between different metamaterials,
  - Interfaces between metamaterials and regular dielectric materials.

The resonant frequencies and guided wavelengths for structures filled with metamaterial have been computed with these new scattering procedures; the results are in good agreement with theoretical values. The dispersion errors of the models are well within the range of typical errors in conventional stub-loaded TLM models.

- *Dispersion analysis of TLM models of Metamaterial with Negative Refractive Index (pages 76 to 88)*

  The wave properties of 3D TLM models of metamaterials with negative refractive index have been analyzed and validated. The general dispersion relation for periodic transmission line networks with embedded lumped elements and reactive stubs has been formulated as a singular value problem and solved numerically using Matlab's symbolic matrix solver. The Matlab result agrees well with the corresponding TLM simulation with negligible difference between them after the fifth significant digit. The results also reveal the presence of directional dispersion that is strongest in diagonal direction for the 3D symmetrical condensed node models. This tendency reflects the behavior of the unloaded nodes upon which the metamaterial models are based. Since in most practical simulations the direction of wave propagation is not known, the dispersion error margin can be predicted by evaluating approximate

closed-form expressions for axial propagation. Such expressions have been presented and validated as well; they are derived using lumped embedded elements and are equivalent to expressions available in the literature.

- *Modeling of Gyromagnetic Materials in 2D-TLM Shunt Node (pages 94 to 107)*

  A new model to describe gyromagnetic materials with the 2D-TLM shunt node mesh has been developed. The dispersive and nonreciprocal properties of gyromagnetic materials are represented by inter-cell networks which contain LC resonators and voltage sources controlled by current flowing through the capacitor of the perpendicular arms. The scattering matrices are derived for homogeneous gyromagnetic materials and boundaries such as electric, magnetic and absorbing boundaries. This new model has been validated by comparing computed data with analytical results for phase constants in completely and partially ferrite-filled rectangular waveguides. The modeling error is compatible with that reported in the literature and is within the typical margin of error affecting the numerical modeling of regular materials.

1.3 Overview of this dissertation

Following this introduction, Chapter 2 gives basic information related to the TLM method with focus on the 2D-shunt node and the 3D-SCN node schemes.

Chapter 3 explores a new model to represent the field singularity in the vicinity of metallic wedges, sharp edges and 90° corners.

Chapter 4 illustrates a new scheme for embedding lumped networks into TLM by means of current controlled coupling, and a new analog behavioral model to introduce frequency domain S-parameters into a PSPICE circuit simulator. The former approach allows n-port SPICE circuits to be embedded into a TLM time domain field simulation environment while the latter enables field-based results to be embedded into a circuit simulation environment.

Chapter 5 investigates the new inter-cell network framework concept in TLM and provides details about the functionality of the inter-cell framework, the implementation method and its frequency and space dispersion properties.

Chapter 6 presents the modeling of metamaterials using the inter-cell network framework, and derives special inter-cell network scattering matrices required for bounding homogeneous metamaterial by electric, magnetic, and absorbing boundaries, and for interfacing different metamaterials with each other and with regular materials. The chapter also presents a dispersion analysis of the inter-cell loaded SCN implementation.

Chapter 7 explores a new method for modeling gyromagnetic materials by 2D-TLM shunt node networks. The dispersive and nonreciprocal properties are represented by an inter-cell network. Impulse scattering matrices are derived for bounding homogeneous gyromagnetic materials with electric, magnetic, and absorbing walls.

Finally, Chapter 8 summarizes the most important results given in this dissertation and presents potential future research directions for the development of multilevel modeling techniques in TLM.

Chapter 2

Theoretical Foundations of TLM

This chapter summarizes the theoretical foundations of the time domain TLM method, describing the basic 2D-Shunt Node, the 3D Symmetrical Condensed Node (3D SCN), the way to model material properties in TLM, and the different error sources in TLM.

2.1 Introduction

The Transmission Line Matrix (TLM) method evolved from early network representations of Maxwell's equations [2] and the use of physical transmission line meshes to model microwave components and discontinuities [3, 4]. Several numerical formulations, known by the generic name of "TLM methods" were pioneered by Johns and his co-workers, starting in 1971 with the first 2D formulation (2D Shunt Node) [5], followed in 1974 by the 3D Expanded Node [6] and in 1987 by the Symmetrical Condensed Node [7]. The Transmission Line Matrix Method (TLM) is based on Huygens' principle which is a localized recursive definition of electromagnetic wave propagation in the time domain. According to Huygens, a wavefront consists of a number of secondary radiators which give rise to spherical wavelets. The envelope of these wavelets forms a new wavefront which, in turn, gives rise to a new generation of spherical wavelets, and so on. The systematic application of this principle leads to an accurate description of wave propagation and scattering [8].

TLM is a space-and–time numerical method that belongs to the family of differential time domain techniques. Instead of discretizing Maxwell's equations directly, TLM is based on transmission line theory. In the same manner as a uniform electromagnetic plane wave can be associated with a single transmission line having a specific characteristic impedance and phase velocity, more complex electromagnetic phenomena can be modeled with a mesh of transmission lines. Such a mesh represents an equivalent

network of the structure under investigation, and classic circuit and network theory can be used for its analysis.

Several TLM nodes such as the 2D shunt node, 2D series node, 3D SCN node and others differ in the circuit topology used to model the junction of the transmission lines. A mapping between the voltages and currents of each node and the components of the electromagnetic field is available. Therefore, by solving a TLM network one can simulate the behavior of electromagnetic field in an arbitrary electromagnetic structure that is modeled by the TLM mesh.

Due to the discrete nature of the method, the field values in a TLM simulation are available only at periodic time intervals Δt often referred to as "time step". Furthermore, the field values are only defined at specific points in space with an interval of $\Delta \ell$, which is called mesh parameter, mesh resolution or cell size in the TLM literature. These time- and space-finite elements (Δt and $\Delta \ell$) are related by the velocity of propagation $v_{\ell 0}$ ($\Delta t = \Delta \ell / v_{\ell 0}$) on the TLM link lines.

The advantages of the TLM techniques reside in their flexibility, the capability of modeling a large class of media, and the possibility to handle complex, geometrically irregular structures.

A brief review of 2D and 3D free space TLM schemes will be given in the following section. The detailed method and applications of TLM can be found in references [7], [9], [10], [11], and [12].

2.2 TLM schemes

2.2.1 Basic 2D shunt node

Transmission line elements can be connected in parallel or in series. In the shunt node (shown in Figure 2.1), the transmission lines (also called link lines) are connected in parallel whereas in the series node the lines are connected in series. Voltage impulses injected at any point in the network can propagate directly to adjacent nodes through the transmission lines connecting them. Once the impulses arrive at the neighboring nodes, scattering occurs, and a new set of impulses will emerge and propagate toward their

neighbors. By virtue of the isomorphism [12] between the transmission line equations and Maxwell's equations, the impulse voltages and currents in the transmission lines model the components of the electric and magnetic fields in two-dimensional space (2.3). Since many wave problems are or can be formulated as two-dimensional, we can simulate a considerable number of electromagnetic structures by solving the 2D-TLM networks [9], [12].

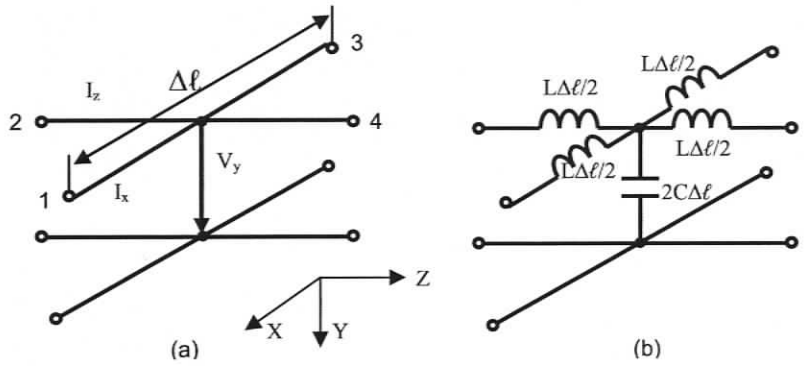

Figure 2.1 The building block of the two-dimensional square shunt TLM network [9]. (a) shunt node (b) the equivalent circuit of the shunt node.

The scattering matrix that relates the reflected voltages at time $k\Delta t$ (the integer k is the number of time steps) to the incident voltages at the same time instant, and the connection matrix that describes the propagation of voltage impulses to the neighboring nodes are defined as follows:

$$[{}_k v^r] = [S] \cdot [{}_k v^i] \quad \text{and} \quad [{}_{k+1} v^i] = [C] \cdot [{}_k v^r] \tag{2.1}$$

where:

$$[{}_k v^r] = \begin{pmatrix} V_1 \\ V_2 \\ V_3 \\ V_4 \end{pmatrix}^r_k \qquad [S] = \frac{1}{2}\begin{pmatrix} -1 & 1 & 1 & 1 \\ 1 & -1 & 1 & 1 \\ 1 & 1 & -1 & 1 \\ 1 & 1 & 1 & -1 \end{pmatrix}$$

$$[{}_k v^i] = \begin{pmatrix} V_1 \\ V_2 \\ V_3 \\ V_4 \end{pmatrix}^i_k \qquad [C] = \begin{pmatrix} 0 & 0 & 1 & 0 \\ 0 & 0 & 0 & 1 \\ 1 & 0 & 0 & 0 \\ 0 & 1 & 0 & 0 \end{pmatrix} \tag{2.2}$$

The transmission line equations and the corresponding two-dimensional field equations in an equivalent virtual medium are

Voltage and current relationship	Equivalent field quantities
$\frac{\partial V_y}{\partial x} = -L\frac{\partial I_x}{\partial t}$	$\frac{\partial E_y}{\partial x} = -\mu_m\frac{\partial H_z}{\partial t}$
$\frac{\partial V_y}{\partial z} = -L\frac{\partial I_z}{\partial t}$	$\frac{\partial E_y}{\partial z} = \mu_m\frac{\partial H_x}{\partial t}$
$\frac{\partial I_z}{\partial z} + \frac{\partial I_x}{\partial x} = -2C\frac{\partial V_y}{\partial t}$	$\frac{\partial H_x}{\partial z} + \frac{\partial H_z}{\partial x} = \varepsilon_m\frac{\partial E_y}{\partial t}$

$$E_y \equiv V_y; \quad H_z \equiv I_x; \quad H_x \equiv -I_z; \quad \mu_m \equiv L; \quad \varepsilon_m \equiv 2C \tag{2.3}$$

Here μ_m and ε_m are the permeability and permittivity of the medium modeled by the TLM network. The above equations show that in a 2D TLM mesh the velocity v_ℓ on the link lines is $\sqrt{2}$ times the velocity v_m of voltage waves on the TLM network or in medium, since

$$v_{\ell 0} = \frac{1}{\sqrt{LC}} = \frac{\sqrt{2}}{\sqrt{\varepsilon_m \mu_m}} = v_m\sqrt{2} \tag{2.4}$$

The relationship between the characteristic impedance $Z_{\ell 0}$ of the link lines and the characteristic impedance Z_{mo} of the network or in medium is

$$Z_{\ell 0} = \sqrt{\frac{L}{C}} = \sqrt{\frac{\mu_m}{\varepsilon_m}}\sqrt{2} = Z_{m0}\sqrt{2} \tag{2.5}$$

A series-connected mesh of transmission lines has similar wave properties. According to Babinet's principle, based on the dual nature of the electric and magnetic fields, one case can be transformed into the other by simply replacing E_y with H_y, ε with μ, and the impedances with the admittances[11]. Therefore, it is not necessary to discuss the series node in this thesis.

2.2.2 The basic 3D SCN node

The symmetrical condensed node (SCN) was first introduced by P. B. Johns in 1987 [7]. The topology of a 3D-SCN node is shown in Figure 2.2. This node consists of six arms; each arm has two orthogonally polarized ports. Hence, the 3D SCN node has a total of 12 ports. The voltage pulses corresponding to the two polarizations are carried in a pair of uncoupled transmission lines. All the transmission lines have the same characteristic impedance $Z_{\ell 0}$. The condensed node has the advantage that all six field components are available simultaneously at the center of the TLM cell as well as at the cell boundaries, providing maximum flexibility for embedding devices and creating TLM field models with complex boundary shapes.

The symmetrical condensed node has been widely used in TLM; it is suitable for solving most general types of wave problems involving nonlinear, inhomogeneous, anisotropic material properties and arbitrary geometries.

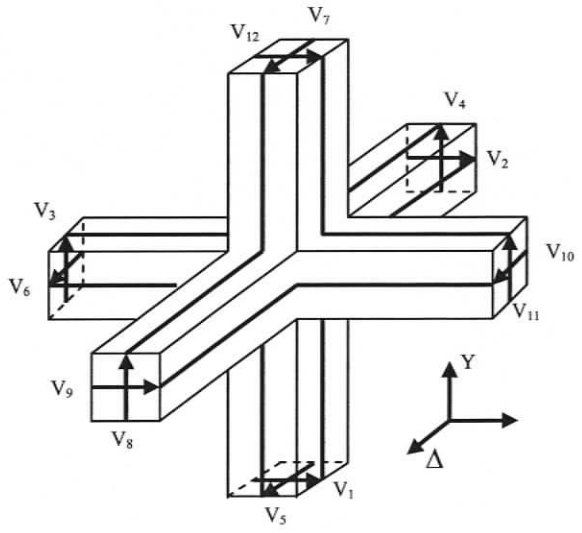

Figure 2.2 3D-TLM symmetrical condensed node topology [7]

The derivation of the scattering properties of the SCN is not as straightforward as in the 2D shunt node case. At the time when the SCN node was proposed, the 12 x 12 impulse scattering matrix was derived on the basis of symmetry considerations and by enforcing general energy and conservation principles [12]. In the late 1990's, Tardioli and Hoefer derived the SCN node scattering matrix from the integral formulation of

Maxwell's equations [13]. The resulting scattering matrix describing free space is shown in equation 2.8.

$$\begin{pmatrix} v_1 \\ v_2 \\ v_3 \\ v_4 \\ v_5 \\ v_6 \\ v_7 \\ v_8 \\ v_9 \\ v_{10} \\ v_{11} \\ v_{12} \end{pmatrix}_k^r = \frac{1}{2} \begin{pmatrix} 0 & 1 & 1 & 0 & 0 & 0 & 0 & 0 & 1 & 0 & -1 & 0 \\ 1 & 0 & 0 & 0 & 0 & 1 & 0 & 0 & 0 & -1 & 0 & 1 \\ 1 & 0 & 0 & 1 & 0 & 0 & 0 & 1 & 0 & 0 & 0 & -1 \\ 0 & 0 & 1 & 0 & 1 & 0 & -1 & 0 & 0 & 0 & 1 & 0 \\ 0 & 0 & 0 & 1 & 0 & 1 & 0 & -1 & 0 & 1 & 0 & 0 \\ 0 & 1 & 0 & 0 & 1 & 0 & 1 & 0 & -1 & 0 & 0 & 0 \\ 0 & 0 & 0 & -1 & 0 & 1 & 0 & 1 & 0 & 1 & 0 & 0 \\ 0 & 0 & 1 & 0 & -1 & 0 & 1 & 0 & 0 & 0 & 1 & 0 \\ 1 & 0 & 0 & 0 & 0 & -1 & 0 & 0 & 0 & 1 & 0 & 1 \\ 0 & -1 & 0 & 0 & 1 & 0 & 1 & 0 & 1 & 0 & 0 & 0 \\ -1 & 0 & 0 & 1 & 0 & 0 & 0 & 1 & 0 & 0 & 0 & 1 \\ 0 & 1 & -1 & 0 & 0 & 0 & 0 & 0 & 1 & 0 & 1 & 0 \end{pmatrix} \bullet \begin{pmatrix} v_1 \\ v_2 \\ v_3 \\ v_4 \\ v_5 \\ v_6 \\ v_7 \\ v_8 \\ v_9 \\ v_{10} \\ v_{11} \\ v_{12} \end{pmatrix}_k^i \tag{2.8}$$

The voltages reflected at each port of each node are exchanged with the voltages emerging from the adjacent nodes. At the next time step those voltages become incident pulses and are scattered by the node again.

In a 3D-SCN TLM network the velocity $v_{\ell 0}$ on the link lines is twice the velocity v_m of voltage impulses on the TLM network or medium ($v_{\ell 0} = 2v_m$), and the characteristic impedance $Z_{\ell 0}$ of the link lines is the same as the characteristic impedance Z_{mo} of the TLM network($Z_{\ell 0} = Z_{m0}$).

2.3 Modeling of Materials in TLM

2.3.1 Modeling of lossy dielectric materials with the 2D shunt node

In 2D-TLM, lossy dielectric media are usually simulated by introducing loss stubs and permittivity stubs. The length of the permittivity stubs is fixed at $\Delta\ell/2$ to ensure synchronism of impulses on all mesh elements, but their normalized characteristic admittance y_0 (the normalizing admittance is the characteristic admittance $Y_{l0} = \sqrt{C/L}$ of the main link lines) can take any value to describe an arbitrary dielectric constant. At low frequencies ($\Delta\ell/\lambda_m << 1$), the permittivity stubs add a lumped capacitance of $Cy_0\Delta\ell/2$ at each node. The total shunt capacitance at each node thus becomes $2C\Delta\ell(1+y_0/4)$. The real

loss stub conductance $g_0\sqrt{C/L}$ appears in parallel with that capacitance. Here g_0 is the normalized characteristic admittance of the shunt stubs. L and C are the inductance and capacitance per unit length of the main link lines. Therefore, the impulse scattering matrix for a stub-loaded shunt node becomes the one shown in equation 2.6, with the additional impulse v_5 on the permittivity stub [8].

$$\begin{pmatrix} v_1 \\ v_1 \\ v_1 \\ v_1 \\ v_5 \end{pmatrix}_k^r = \frac{1}{y}\begin{pmatrix} 2-y & 2 & 2 & 2 & 2y_0 \\ 2 & 2-y & 2 & 2 & 2y_0 \\ 2 & 2 & 2-y & 2 & 2y_0 \\ 2 & 2 & 2 & 2-y & 2y_0 \\ 2 & 2 & 2 & 2 & 2y_0-y \end{pmatrix} \cdot \begin{pmatrix} v_1 \\ v_1 \\ v_1 \\ v_1 \\ v_5 \end{pmatrix}_k^i \tag{2.6}$$

where

$$y = 4 + y_0 + g_o, \qquad \mu_m = L, \qquad \varepsilon_m = 2C(1 + y_0/4), \qquad \sigma_m = \frac{g_0\sqrt{C/L}}{\Delta\ell} \tag{2.7}$$

Parameter	Link lines/Elements	Network or in Medium
Cell Size	$\Delta\ell$	$\Delta\ell$
Time Step	$\Delta t = \Delta\ell/(c\sqrt{2})$	$\Delta t = \Delta\ell/(v_m\sqrt{2\varepsilon_r})$
Phase Velocity	$v_{\ell 0} = \Delta\ell/\Delta t = c\sqrt{2} = v_m\sqrt{2\varepsilon_r}$	$v_m = c/\sqrt{\varepsilon_r}$
Frequency	$f = \omega/(2\pi)$	$f = \omega/(2\pi)$
Wavelength	$\lambda_{\ell 0} = v_{\ell 0}/f = \lambda_0\sqrt{2} = \lambda_m\sqrt{2\varepsilon_r}$	$\lambda_m = \lambda_0/\sqrt{\varepsilon_r}$
Attenuation Constant	$\alpha_{\ell 0} = \alpha_m/\sqrt{2\varepsilon_r}$	$\alpha_m = \sigma_m Z_m/2$
Phase Constant	$\beta_{\ell 0} = \beta_m/\sqrt{2\varepsilon_r}$	$\beta_m = \omega/v_m$
Link Line C	$C = \varepsilon_0/2 = \varepsilon_m/(2\varepsilon_r)$	$\varepsilon_m = \varepsilon_0\varepsilon_r$
Link Line L	$L = \mu_0 = \mu_m$	$\mu_m = \mu_0$
Link Line $Z_{0\ell}$	$Z_{\ell 0} = \sqrt{L/C} = \eta_0\sqrt{2} = Z_m\sqrt{2\varepsilon_r}$	$Z_m = \eta_0/\sqrt{\varepsilon_r}$
Permittivity Stub Z_{s0}	$Z_{s0} = Z_{\ell 0}/y_0 = Z_{\ell 0}/(4(\varepsilon_r - 1))$	$\varepsilon_m = \varepsilon_0\varepsilon_r$
Loss Stub R_0	$R_0 = Z_{\ell 0}/g_0 = Z_{\ell 0}/(\eta_0\sigma_m\Delta\ell)$	σ_m

Table 2.1 Relationships between the characteristics of mesh lines/elements and the properties of the resulting 2D-TLM shunt network model at low frequencies [8].

Table 2.1 relates the characteristics of link lines and stubs to the properties of the 2D shunt network formed by them. These relationships will be used in the following chapters involving 2D shunt nodes.

2.3.2 Modeling dielectric materials in 3D SCN TLM

In 3D SCN TLM, the properties of materials are traditionally described by six reactive stubs. Ports 1-12 are exactly the same as for the node without stubs (Figure 2.2) and are connected to neighboring nodes to form the mesh. The stub ports 13 to 18 couple only with the fields E_x, E_y, E_z, H_x, H_y, and H_z, respectively. The E-field stub ports are open-circuited and add capacitance to the node, while the H-field stub ports are short-circuited and add inductance to the node. The time taken for a pulse to travel from the port terminals to the center of the node, where scattering takes place, is $\Delta t/2$ for all transmission line legs 1 to 18, where Δt is the TLM time interval. The scattering equation $V^r = SV^i$ for the node with stubs now contains an 18×18 scattering matrix, which has the following form [7], [14]

#			1	2	3	4	5	6	7	8	9	10	11	12	13	14	15	16	17	18
	s		x	x	y	y	z	z	z	y	x	z	y	x	x	y	z			
		o	z	y	z	x	x	y	x	x	y	y	z	z				x	y	z
1	x	z	a	b	d						b		$-d$	c	g					i
2	x	y	b	a				d			c	$-d$		b	g				$-i$	
3	y	z	d		a	b				b			c	$-d$		g				$-i$
4	y	x			b	a	d		$-d$	c			b			g		i		
5	z	x				d	a	b	c	$-d$		b					g	$-i$		
6	z	y		d			b	a	b		$-d$	c					g		i	
7	z	x				$-d$	c	b	a	d		b					g	i		
8	y	x			b	c	$-d$		d	a			b			g		$-i$		
9	x	y	b	c				$-d$			a	d		b	g				i	
10	z	y		$-d$			b	c	b		d	a					g		$-i$	
11	y	z	$-d$		c	b				b			a	d		g				i
12	x	z	c	b	$-d$						b		d	a	g					$-i$
13	x		e	e							e			e	h					
14	y				e	e				e			e			h				
15	z						e	e	e			e					h			
16		x				f	$-f$		f	$-f$								j		
17		y		$-f$				f			f	$-f$							j	
18		z	f		$-f$								f	$-f$						j

(2.9)

where

$$a = \frac{-Y}{2(4+Y)} + \frac{Z}{2(4+Z)}; \qquad b = \frac{2}{(4+Y)}; \qquad c = \frac{-Y}{2(4+Y)} - \frac{Z}{2(4+Z)};$$

$$d = \frac{4}{2(4+Z)}; \qquad e=b; \qquad f = Z \cdot d;$$

$$g = Y \cdot b; \quad h = \frac{(Y-4)}{(Y+4)}; \qquad i = d; \qquad j = \frac{(4-Z)}{(4+Z)}$$

For the lossless case, the Y's and Z's are given by

$$Y_x = 4\left(\varepsilon_x \frac{vw}{u\Delta\ell} - 1\right) \qquad Y_y = 4\left(\varepsilon_y \frac{uw}{v\Delta\ell} - 1\right) \qquad Y_z = 4\left(\varepsilon_z \frac{vu}{w\Delta\ell} - 1\right)$$

$$Z_x = 4\left(\mu_x \frac{vw}{u\Delta\ell} - 1\right) \qquad Z_y = 4\left(\mu_y \frac{uw}{v\Delta\ell} - 1\right) \qquad Z_z = 4\left(\mu_z \frac{vu}{w\Delta\ell} - 1\right)$$

The subscripts of Y and Z designate the corresponding stub. For example, $S_{29} = c = \frac{-Y_x}{2(4+Y_x)} - \frac{Z_y}{2(4+Z_y)}$, since ports 2 and 9 are both associated with E_x and H_y. Y_x, Y_y, and Y_z are the characteristic admittances of the E_x, E_y , and E_z stub normalized to the characteristic admittance of free space Y_0, respectively. Z_x, Z_y, and Z_z are the characteristic impedances of the H_x, H_y, and H_z stub normalized to the characteristic impedance of free space Z_0, respectively. u, v, and w are the dimensions of the unit cell in the x, y and z-direction, respectively.

The field components can be calculated from the voltage impulses. They are

$$E_x = 2\left(V_1^i + V_2^i + V_9^i + V_{12}^i + Y_x V_{13}^i\right)/(u(4+Y_x))$$

$$E_y = 2\left(V_3^i + V_4^i + V_8^i + V_{11}^i + Y_y V_{14}^i\right)/(v(4+Y_y))$$

$$E_z = 2\left(V_5^i + V_6^i + V_7^i + V_{10}^i + Y_z V_{15}^i\right)/(w(4+Y_z))$$

$$H_x = 2\left(V_4^i - V_5^i + V_7^i - V_8^i - V_{16}^i\right)/(Z_0 u(4+Z_x))$$

$$H_y = 2\left(-V_2^i + V_6^i + V_9^i - V_{10}^i - V_{17}^i\right)/(Z_0 v(4+Z_y))$$

$$H_z = 2\left(-V_3^i + V_1^i + V_{11}^i - V_{12}^i - V_{18}^i\right)/(Z_0 w(4+Z_z)) \qquad (2.10)$$

2.4 Error sources in TLM

Like all other numerical techniques, the TLM method is subject to various sources of error and must be treated with caution in order to obtain reliable and accurate results. The accuracy of each TLM simulation is affected by those errors, and each of them can be more or less predominant, depending on several factors such as the type of structure under investigation, cell size, frequency of interest, etc.

A brief overview of errors related to the discrete nature in space and affecting the accuracy of the TLM method will be considered below, and possible techniques for their reduction will be described.

- Velocity or Dispersion Error

As long as the wavelength in the TLM network is large compared with the cell size, it can be assumed that the fields propagate with the same frequency-independent velocity in all directions, and the TLM network behaves like a continuous medium. However, when the cell size is increased, or the frequency of interest is increased, the TLM network can no longer be considered as a continuous medium and the network velocity becomes dispersive and depends more and more on the frequency and the direction of propagation. The error so introduced is referred to as velocity or dispersion error.

Based on the dispersion analysis for both the 2D and 3D TLM methods [15] [16] the rule of thumb is that a dispersion error of less than one percent can be obtained for a discretization of twenty cells per wavelength in most of the cases.

- Coarseness Error

When the TLM mesh is too coarse to resolve the highly non-uniform fields at corners and wedges where some components of the electromagnetic field are singular, the coarseness error occurs. Strictly speaking, the coarseness error is a form of dispersion error in the sense that the spatial wavelength needed to approximate the field at a singularity becomes much shorter than the free space propagating wavelength associated with the operating frequency [8].

Both dispersion error and coarseness error result in a shift in the frequency characteristics of the structures under investigation. This shift is usually towards lower

frequencies. However, some particular combinations of dielectric and magnetic materials may lead to a positive shift.

More details regarding the coarseness error and methods employed to minimize the coarseness error are discussed in Chapter 3.

2.5 Summary

In this chapter the fundamental concepts of the TLM method, its basic building blocks (2D shunt node and 3D SCN node), ways to model dielectric materials, and the principal error sources in those models have been presented. A number of approaches for enhancing the capabilities of the TLM method are presented in the following chapters.

Chapter 3

Singularity Correction in the TLM Method

In the previous chapter, the TLM theory and its dispersion and coarseness errors have been summarized. This chapter describes the errors caused by field singularities, and presents a numerically efficient way to reduce the errors.

3.1 Introduction

The TLM method discretized the computational domain into a finite number of small cells. The main sources of error related to the space discrete nature of TLM are dispersion and coarseness errors. If the wavelength in the TLM network is large compared with the discrete parameter or cell size $\Delta\ell$, it can be assumed that the fields propagate with the same velocity in all directions. However, when the wavelength decreases, the propagation velocity in the TLM mesh depends on the direction of propagation and on the frequency. At first glance, the resulting velocity error can be reduced only by choosing a very dense mesh, unless propagation occurs at a known angle with respect to the axial directions (e.g., rectangular waveguide), in which case the error can be corrected directly using the dispersion relation. Fortunately, the dispersive error responds to the same remedial measures as the coarseness error, and it therefore does not need to be corrected separately. The coarseness error occurs when the TLM mesh is too coarse to resolve highly non-uniform or singular fields as can be found at edges, corners and wedges. This error is particularly cumbersome when analyzing planar structures which contain such regions [17] [18].

3.1.1 Singularity effects

The modeling of electromagnetic structures with space discrete numerical methods is strongly affected by the presence of field singularities at sharp edges and corners [18]. Regular FDTD and TLM schemes are normally expected to be second-order accurate (the velocity error decreases as $(\Delta\ell/\lambda)^2$), but in the presence of singularities the results deteriorate to first-order accuracy. This is due to the inability of the grid to properly resolve the highly non-uniform fields at edges and corners [18],[19],[20]. As a result, the energy stored in the vicinity of the singularities is not properly modeled, resulting in significant errors in the properties of the structure such as cutoff frequencies, resonant frequencies, propagation constants, characteristic impedances, S-parameters, etc. This phenomenon is illustrated in Figure 3.1. It is clear that, although the discrete mesh parameter (cell size) is quite small compared to the wavelength of the propagating wave, the coarseness error is still relatively large. Therefore, it is important to develop and implement a model for singularity correction.

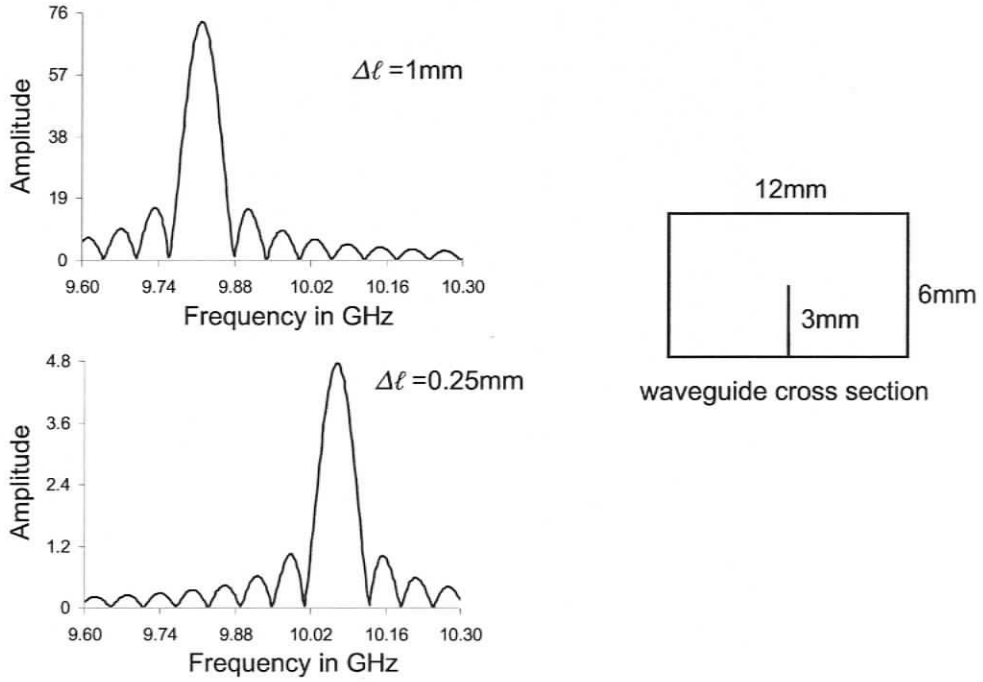

Figure 3.1 Cutoff frequencies of a finned rectangular waveguide obtained with different cell sizes. The shift towards lower frequencies with increasing cell size is clearly visible.

3.1.2 Previous approaches to singularity correction

Since the effect of field singularities is significant, many approaches have been proposed for dealing with the field singularities in the vicinities of metal edges in FDTD and TLM. A possible measure would be to choose a very fine mesh. However, this would lead to large memory requirements and a dramatic increase in computation time due to the smaller time step required for stability, particularly for three-dimensional problems. A better remedy is to introduce a network of variable cell size to provide higher resolution in the non-uniform field region. Graded mesh and multi-grid mesh are often applied intuitively to increase the resolution of the grid in the critical regions [19],[21], but the resulting computational cost is still quite high and often unacceptable; also the treatment of the interface between meshes of different sizes is a difficult task [22].

A smarter approach is to use basis functions at the discontinuities that resemble the singular fields at metallic edges and corners. The *a priori* knowledge used in this approach is that the singular field distribution is quasi-static since the time derivative of the fields is insignificant compared with their space derivative. Therefore the properties of the quasi-static field sub-region can be modified so that the stored energy is correct even though the field itself is poorly resolved. A variety of forms can be taken to represent the singular field. For instance, modifying the update equations in a FDTD algorithm or the scattering matrix of cells in the vicinity of singularities in TLM is one possible correction method [23],[24],[25],[26],[27],[28],[29]. Another method is to insert lumped reactive elements [30],[31] into nodes or cells near the metallic edges and corners, or one may use additional transmission line stubs at corner nodes for singularity correction [32]. But these approaches may increase computational burden or require complex algorithms, and may sometimes result in instability [22, 33].

3.2 Singularity correction by local modifications of ε and μ

It is important to remember that the singular field distribution is quasi-static. While some of the field components become infinite at sharp edges and corners, the energy they contain remains finite. The local character of the singularity fields implies that they are independent of boundary conditions several mesh cells away. Hence, a single correction

will be valid for all external boundary geometries, provided they are not in the near-field of the singularity. According to this *a priori* knowledge a simple method for singularity modeling (singularity correction) is proposed for TLM modeling. This method is based on the local modification of the constitutive parameters ε and μ in TLM cells directly surrounding the metallic edges and corners. It is numerically robust, independent of the type of singularity (quasi-TEM, TE or TM), can be easily implemented to function automatically, and has negligible computational overhead.

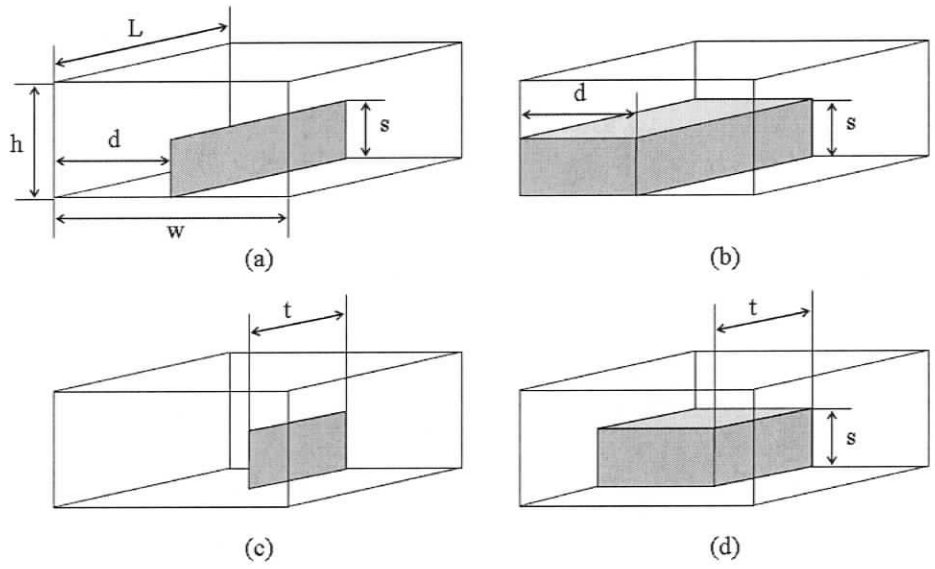

Figure 3.2 Four types of singularities for which correction coefficients have been determined. (a) Knife Edge (b) 90° Edge (c) Knife Edge Corner (d) 90° Edge Corner.

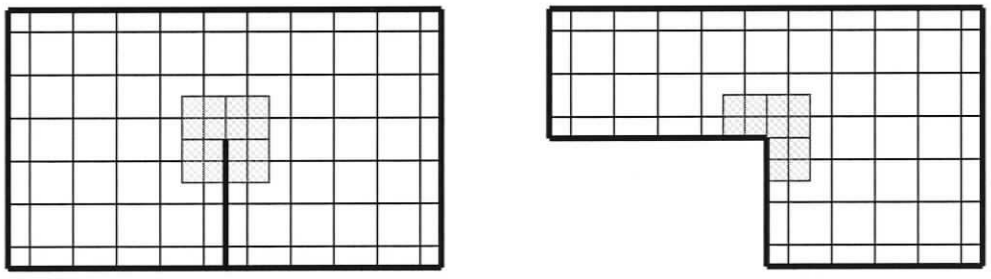

Figure 3.3 The singularities are corrected by changing the ε and μ in the cells surrounding the edge. (a) four edge cells are modified along the Knife Edge; (b) three cells are modified along the 90° Edge.

A correction procedure for all types of field singularities at sharp edges and 90° corners in 2D and 3D TLM models has been developed and implemented. The energy storage capacity of the TLM cells in the immediate vicinity of the edge is reduced by lowering the values of their dielectric permittivity and magnetic permeability. Figure 3.2 shows the four basic configurations studied in this thesis. Figure 3.3 shows the location of the modified cells.

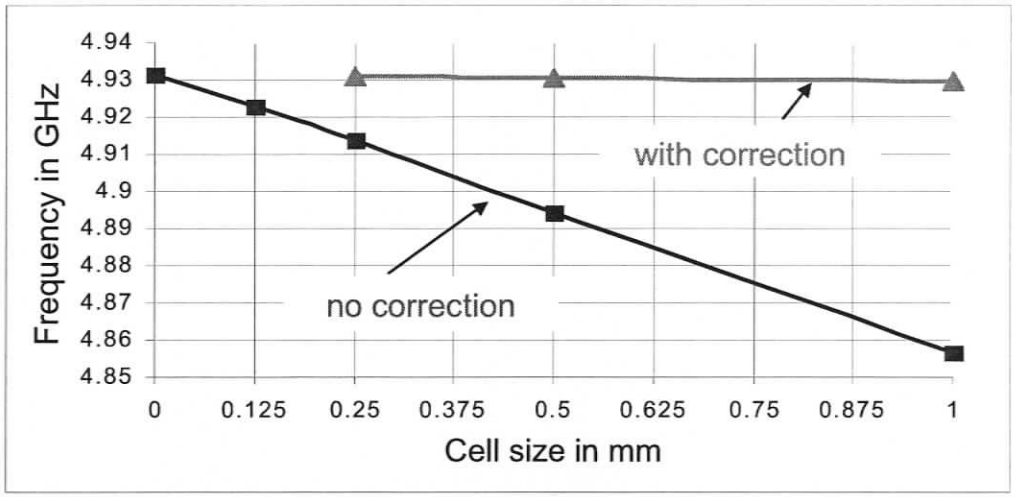

Figure 3.4 Resonant frequency of a cavity containing a Knife Edge singularity, as a function of the mesh parameter. If the singularity is not corrected, the frequency varies linearly with the mesh parameter (first order error). However, with proper modification of the edge cells, the computed resonant frequency is practically independent of the mesh parameter, showing only a slight second-order dispersion error.

Both constitutive parameters are reduced by the same relative amount in order to preserve the local intrinsic wave impedance of the field space. While the required change in ε and μ can be computed approximately using the known expressions for the quasi-static fields, it is straightforward to determine them by optimization. The ε and μ parameters of the edge cells are modified such that the resonant frequencies of a resonator that contains the edge singularity become virtually independent of the cell size, keeping the mesh parameter small enough for the dispersion error to be negligible ($\Delta\ell/\lambda < 1/20$) . This is illustrated in Figure 3.4 where the dominant resonant frequency of a cavity with a knife edge singularity has been drawn as a function of the mesh parameter (Δl= 1mm, 0.5mm, .25mm, 0.125mm) used to compute that frequency. If the singularity is not corrected, the frequency varies linearly with the mesh parameter (first order error).

However, with proper modification of the edge cells, the computed resonant frequency is practically independent of the mesh parameter as long as $\Delta\ell/\lambda < 1/10$, showing only a slight second-order dispersion error.

Using this optimization process, the following correction coefficients for the four types of singularities (Knife Edge, 90° Edge, Knife Edge Corner, and 90° Edge Corner) have been obtained. Note that the edge causing the largest singularity (Knife Edge Corner) needs the largest correction coefficient.

Singularity Type	Correction Coefficient for ε	Correction Coefficient for μ
Knife Edge (Figure 3.2 a)	0.808	0.808
90° Edge (Figure 3.2 b)	0.94	0.94
Knife Edge Corner (Figure 3.2 c)	0.708	0.708
90° Edge Corner (Figure 3.2 d)	0.827	0.827

Table 3.1 Correction coefficients for the four types of singularities shown in Figure 3.2.

The correction region is along the edge but contains only the immediately adjacent cells. This means that when the computational mesh parameter is reduced, the correction region is automatically reduced as well.

Furthermore, these correction coefficients are independent of the material properties. They are the same when a knife edge or corner is immersed in materials with arbitrary permittivity and permeability, or when the singularity lies at the interface between different materials such as in microstrip lines. The constitutive parameters in each corner cell are simply multiplied by the appropriate correction factor given in Table 3.1.

3.3 Validation results

The accuracy and efficiency of the correction method discussed in section 3.2 is validated in this section using discontinuities in rectangular waveguide and microstrip structures.

3.3.1 Resonant frequency calculation

The first example is a knife edge discontinuity in a rectangular cavity as depicted in Figure 3.5. Table 3.2 records the resonant frequencies obtained with and without the edge correction technique.

Cell size (mm)	$\Delta l = 1.0$	$\Delta l = 0.5$	$\Delta l = 0.25$	Infinitesimal (extrapolated value)
f (in GHz, without correction)	7.6541	7.7674	7.8235	7.88
Error relative to $\Delta l \to 0$	– 2.9%	– 1.4%	– 0.7%	0
f (in GHz, with correction)	7.8758	7.8776		7.88
Error relative to $\Delta l \to 0$	– 0.05%	– 0.03%		0

Table 3.2 Resonant frequencies of a rectangular waveguide cavity (L=15mm, w=20mm, h=10mm) containing a knife edge (d=10mm, s=5mm) with and without edge correction.

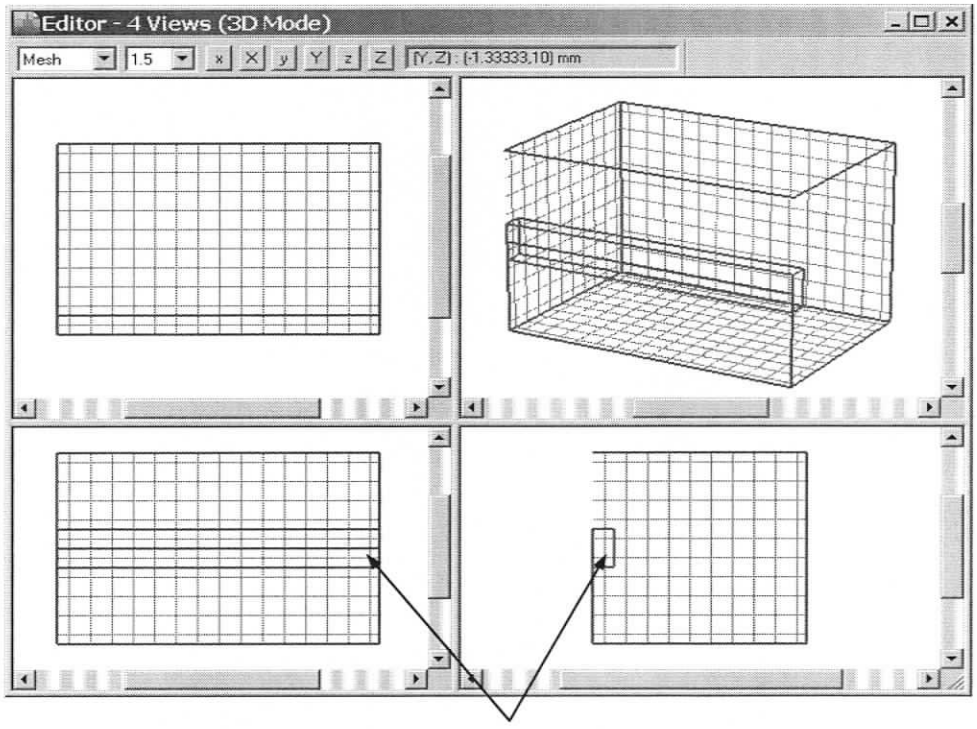

Figure 3.5 The discretized view of a Knife Edge inside a waveguide resonator (due to symmetry property, only one-half of the structure is needed to compute the resonant frequency); the indicated region identify SCN cells along the Knife Edge. The dimensions of the structure are defined in Figure 3.2 and given in Table 3.2.

Similarly, Table 3.3, Table 3.4 and Table 3.5 depict the resonant frequencies for cavities with a 90° edge, a knife edge corner and a 90° edge corner, respectively. The validation results indicate that the edge correction method increases the accuracy in the resonant frequency by one order of magnitude in most of the cases.

Cell size (mm)	$\Delta l = 0.5$	$\Delta l = 0.25$	$\Delta l = 0.2$	Infinitesimal (extrapolated value)
f (in GHz, without correction)	23.0805	23.998	24.1572	24.79
Error relative to $\Delta l \rightarrow 0$	– 6.9%	– 3.2%	– 2.6%	0
f (in GHz, with correction)	24.7694	24.7741		24.79
Error relative to $\Delta l \rightarrow 0$	– 0.08%	– 0.06%		0

Table 3.3 Resonant frequencies of a rectangular waveguide cavity (L=10mm, w=6mm, h=2mm) containing a Knife Edge Corner (d=3mm, s=1mm, t=5mm) with and without edge correction.

Cell size (mm)	$\Delta l = 1$	$\Delta l = 0.5$	$\Delta l = 0.25$	Infinitesimal (extrapolated value)
f (in GHz, without correction)	16.9005	17.0653	17.1281	17.17
Error relative to $\Delta l \rightarrow 0$	– 1.6%	– 0.6%	– 0.3%	0
f (in GHz, with correction)	17.1592	17.1653		17.17
Error relative to $\Delta l \rightarrow 0$	– 0.06%	– 0.03%		0

Table 3.4 Resonant frequency of a rectangular waveguide cavity (L=14mm, w=10mm, h=6mm) containing a 90° Edge (d=5mm, s=3mm) with and without edge correction.

Cell size (mm)	$\Delta l = 0.5$	$\Delta l = 0.25$	$\Delta l = 0.2$	Infinitesimal (extrapolated value)
f (in GHz, without correction)	29.0281	29.1331	29.1677	29.26
Error relative to $\Delta l \rightarrow 0$	– 0.8%	– 0.5%	– 0.3%	0
f (in GHz, with correction)	29.2466	29.2574		29.26
Error relative to $\Delta l \rightarrow 0$	– 0.05%	– 0.01%		0

Table 3.5 Resonant frequency of a rectangular waveguide cavity (L=10mm, w=6mm, h=4mm) containing a 90° Edge Corner (d=2mm, s=2mm, t=4mm) with and without edge correction.

3.3.2 S-parameter calculation

The edge correction method has been applied to analyze an inductive iris with two knife edges in a rectangular waveguide as shown in Figure 3.6.

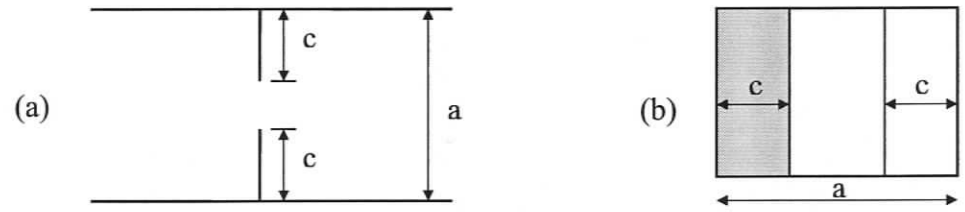

Figure 3.6 Inductive iris in a rectangular waveguide a=10mm, c=3mm: (a) top view (b) front view.

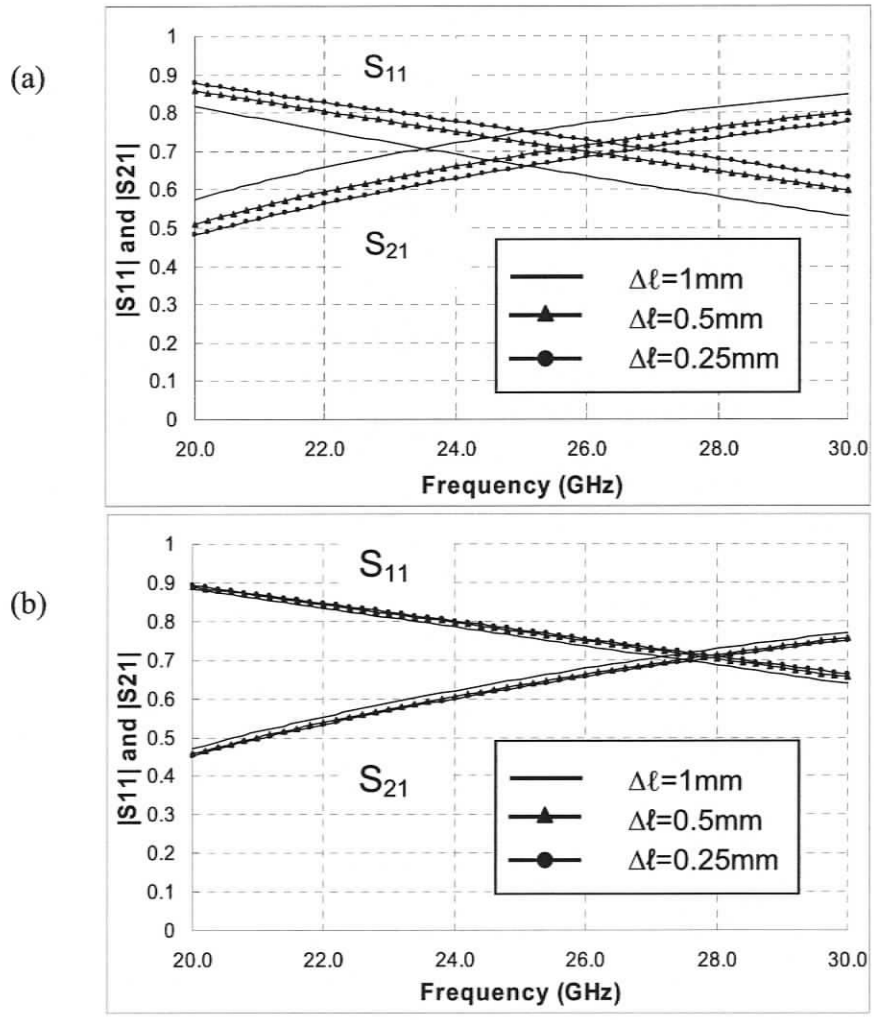

Figure 3.7 S-parameters for the thin iris in a rectangular waveguide obtained with (a) regular TLM without singularity correction, (b) TLM with singularity correction, making results much less sensitive to the mesh parameter.

The scattering parameters obtained for different discretizations are shown in Figure 3.7. Note that the accuracy of the TLM algorithm has been improved considerably by this singularity correction approach even when a very coarse mesh is used.

In order to experimentally validate this approach for the case when a metallic edge lies in the interface between materials with different properties, the singularity correction technique has been used to analyze the microstrip patch antenna shown in Figure 3.8. The geometry of the antenna is exactly the same as in [34] and [35] so that the results can be compared. The feed line of the antenna is a 50Ω microstrip (e = 2.334mm, h = 0.794mm, ε_r = 2.2 and tan $\delta = 0$) and is 1.945mm from the edge of the rectangular patch. The absorbing boundaries are placed to form a computational space with a = 60Δx, b = 16Δy, and c = 130Δz.

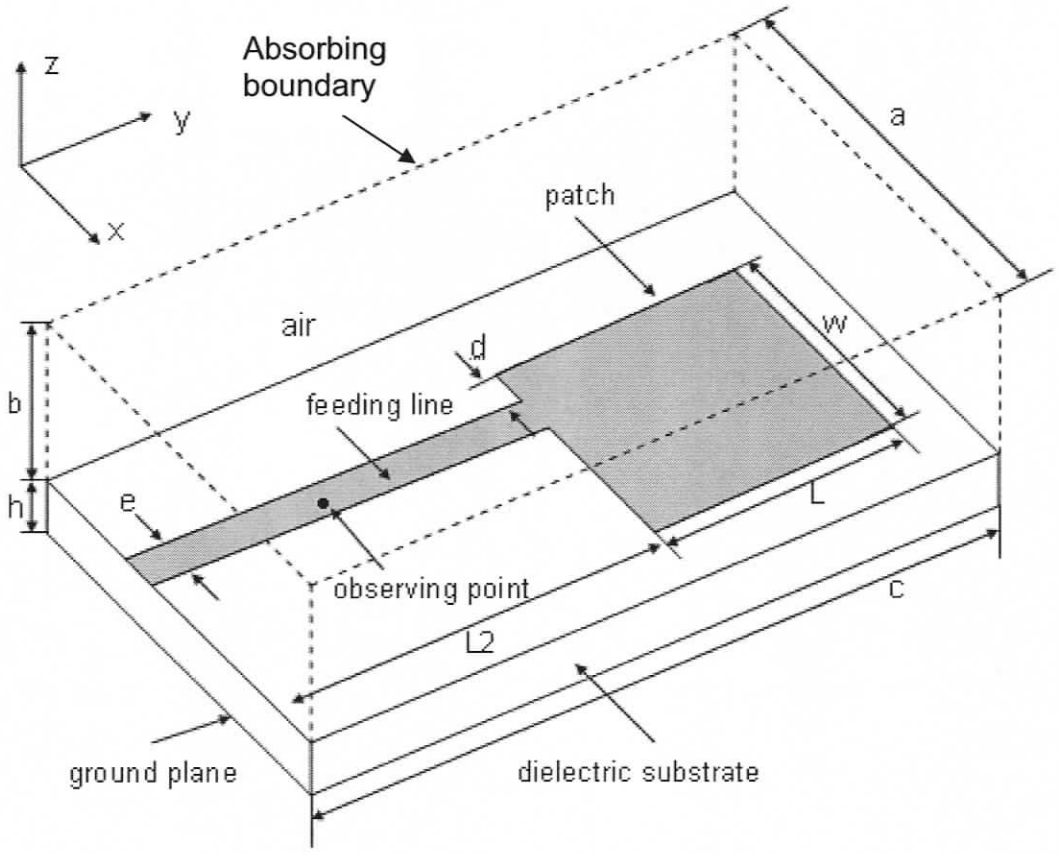

Figure 3.8 The microstrip patch antenna used to validate the proposed singularity correction method. L = 16mm, W = 12.448mm, d=1.945mm, e=2.334mm, h=0.794mm.

The return loss of the antenna has been computed using two different sets of cell sizes (First set: $\Delta x=L/40$, $\Delta y=W/32$, $\Delta z=h/4$. Second set: $\Delta x=L/80$, $\Delta y=W/64$, $\Delta z=h/8$.) with no edge correction. Results are shown in Figure 3.9 together with the results extrapolated for $\Delta\ell\rightarrow 0$ and with the edge-corrected results computed with the first set of mesh parameters. This comparison clearly shows that the edge-corrected results obtained with the coarse mesh (continuous trace) are virtually identical to those obtained with an extremely fine mesh as predicted by extrapolation (square dots). The savings achieved by the edge correction can be appreciated by considering that the computational expenditure increases by a factor of 16 whenever the number of cells is doubled in each coordinate direction.

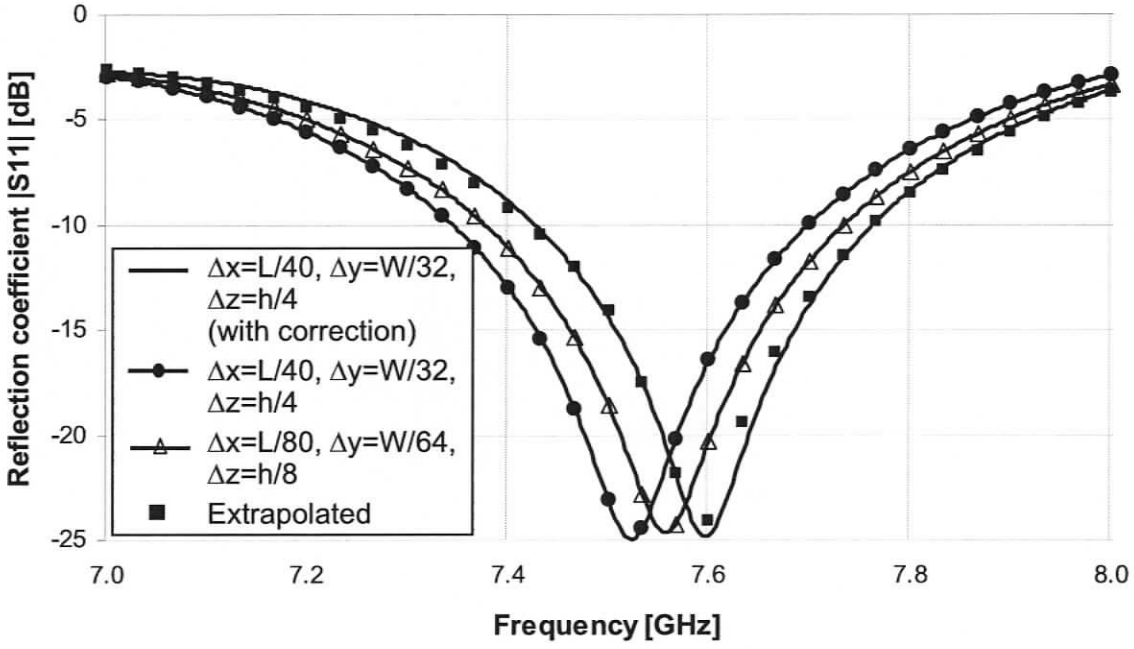

Figure 3.9 The frequency-dependent reflection coefficient $|S_{11}|$ of a microstrip patch antenna with and without singularity correction computed with TLM. The main effect of the correction is the shift in the resonant frequency of the antenna caused by the change in electromagnetic energy stored at the singularity, due to a local change in ε and μ.

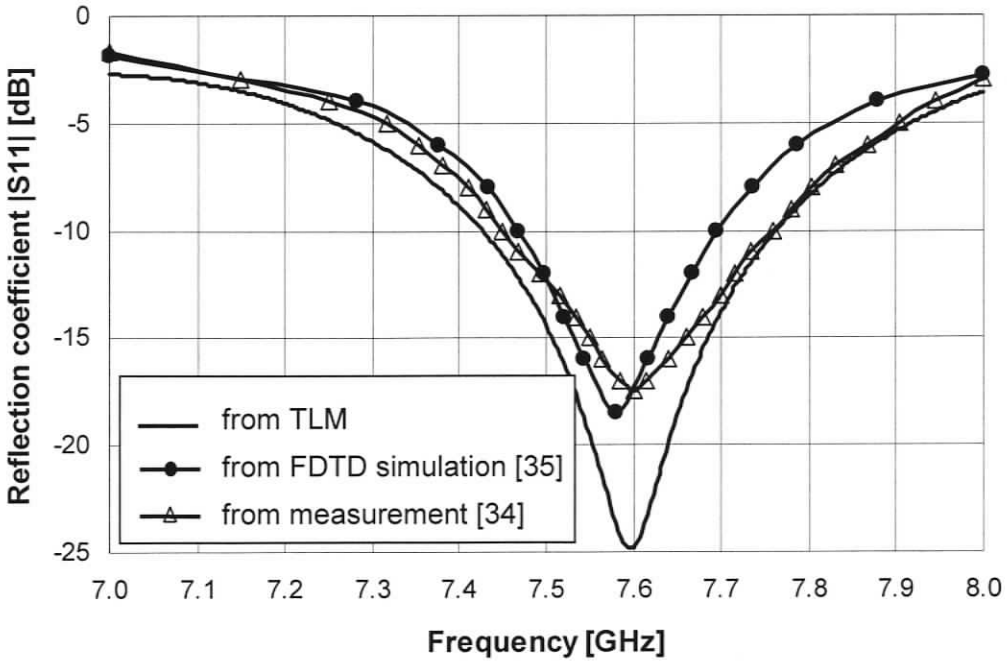

Figure 3.10 Comparison between edge-corrected TLM result, published edge-corrected FDTD simulation data [35] and published measurements [34].

Figure 3.10, compares the edge-corrected TLM results for the patch antenna with measured data published by Wu et al. [34] and FDTD simulation result by Kashiwa et al. [35]. Note that the measured and TLM values of the resonant frequency at 7.6 GHz (which is the key quantity affected by the edge singularity) agree very well. The depth of the minimum is very sensitive to the losses in both the antenna structure and the measurement system, and to the number of time steps employed in the FDTD simulation. Since the references [34] and [35] provide no information on these factors, no reliable comparison of the depth of the minimum values can be made.

3.4 Conclusions

In this chapter, an accurate and numerically robust singularity correction technique for TLM has been discussed. The permittivity and permeability of the cells adjacent to the singularity are modified by a scalar correction factor, which amounts to a quasi-static correction of the electric and magnetic energy stored in the TLM cells at the singularity. This correction is equally effective for quasi-TEM, TE-, TM- and hybrid field excitations of the singularity. Numerical validation shows that this correction method reduces the

coarseness error due to singularity by typically one order of magnitude without penalty in terms of computational burden. The effectiveness of this method for the accurate modeling of structures with metallic strips (knife edges) or 90^{o} edge corners has been clearly demonstrated and validated against published measurement and FDTD simulation data. This approach is applicable to both homogeneous and inhomogeneous material properties in the singularity region.

Chapter 4

Combinations of Field and Circuit Level Modeling

With the rapid progress of computer technology, the finite difference time domain (FDTD) and TLM methods have become very popular tools for the analysis of various electromagnetic problems, including microwave circuits. As the size of microwave circuits and spacing between circuit elements become smaller and smaller, coupling between closely spaced elements adds more parasitic effects to the circuit. Furthermore, proper models of lumped passive and active devices as well as their interaction with electromagnetic fields are critical for accurate EM simulations.

On the other hand, advanced electronic system design requires various types of modeling abstractions for system simulation; these models may include different levels of solutions such as digital/analog circuit analyses and full-wave field simulations. It is impractical to incorporate all the modules in one global simulation. A possible and practical method is to simulate some parts of the system separately, extract certain behavioral parameters like S-parameters, and then introduce these parameters into the full system simulation environment. This approach will reduce the complexity of the simulation and improve computational efficiency.

Therefore it is very important to have a bridge between field solvers and circuit simulators when designing complicated systems. In this chapter, two new methods for modeling field/circuit interactions are described. The first is a technique for embedding lumped circuits into a TLM field model, and the second is a method for introducing S-parameters computed with a TLM field simulator into a circuit model (PSPICE).

4.1 Introduction

4.1.1 Previous work on lumped element embedding in FDTD and TLM

In the 1990's many investigations aimed at extending the FDTD and TLM methods to include simple lumped devices such as resistors, capacitors, inductors and diodes in the full-wave analysis [36],[37],[38],[39],[40]. Since the beginning of the 2000's researchers began to seek a new way to combine time domain FDTD and TLM field solvers with circuit simulators such as SPICE in order to handle large scale circuits and systems. Kobidze [41] described an approach in which a master program is used to control two equal parts (Huilian, it is not clear what this means) of SPICE and FDTD. Orhanovic *et al* [42] introduced a tightly coupled combination of FDTD and SPICE. Ip *et al* [43] presented a full-wave enabled SPICE simulator with characteristic models.

In TLM, the field space is modeled by a network of transmission lines. The transmission lines can be used to create terminals for connecting lumped circuit elements to the field space. In recent years, a number of techniques for embedding two- and three-terminal lumped and distributed devices into TLM meshes have been developed. [44],[45],[46],[47]. So and Hoefer [47] have developed a Thévenin equivalent voltage coupling interface technique to combine TLM networks with SPICE circuits.

In section 4.2 of this thesis, a new Norton equivalent current-coupled technique that connects the TLM network to the device ports is described. This new framework allows n-port SPICE circuits to be embedded into a time domain TLM field environment.

4.1.2 Behavioral modeling in SPICE

Behavioral modeling is the process of developing a model for a system or device from the viewpoint of externally observed behavior rather than from a microscopic or physical description. Two important applications of Behavioral Modeling in the analog circuit simulation domain are the black-box modeling of complex systems and the modeling of new devices [48],[49],[50].

Analog simulators generally include built-in models in model libraries for a limited number of devices. Simulating a circuit containing a device which can not be found in the

model library requires extending the simulator in some ways. According to Sedra *et al.* [51] and [52], we can use polynomial controlled sources or macro-based methods to add new models to SPICE-based circuit simulators. PSPICE (A PC version of SPICE) provides a generic approach to extending its capability by means of an Analog Behavioral Model (ABM) which allows the simulator to be used like a programming language and to solve general mathematical problems by translating them into an electrical circuit with controlled current and voltage sources [53]. However, this built-in feature does not support the use of a complete set of S-parameters. Therefore, a new ABM model has been developed in this chapter to combine field-based computation results with PSPICE-based circuit analysis.

4.2 Lumped network embedding in TLM

This section describes the embedding of a circuit model into a field model in such a way that both the circuit equations and the field equations can be solved concurrently in the time domain.

4.2.1 The current-coupled interface technique

Lumped elements or circuits can be connected to a TLM mesh either at the nodes (center of the cells) or at the cell boundaries as reported in [45],[46,[47]. The major difference between these two approaches lies in the treatment of voltage impulses incident on the device. Both connection schemes give good results; however, the cell boundary implementation is less susceptible to spurious mode effects. Hence, the current-coupled scheme also uses cell boundary connection, placing the lumped network halfway between two nodes; the impulse scattering process at the nodes is thus not affected.

Figure 4.1 depicts the interconnection between a three-terminal lumped network and the TLM mesh represented by two Norton current sources. In general, if the lumped network has n terminals, there are n–1 such independent Norton current sources and one common terminal.

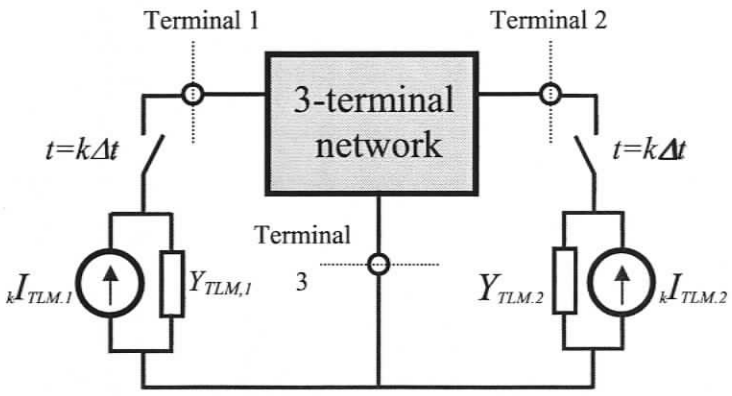

Figure 4.1 Interconnection between a lumped network and a TLM mesh represented by two Norton current sources.

The TLM network is physically much larger than the lumped element or circuit which may consist of resistors, capacitors, inductors and even active elements and sources. While the embedded networks must always remain quasi-lumped from a field perspective (meaning that the physical size of the embedded network must remain small with respect to the spatial wavelength), they can nevertheless occupy a small volume that exceeds the size of a TLM cell. In this case, a distributed interconnection between embedded device and field must be realized. The problem of interconnecting the network with the TLM mesh is reduced to finding the distributed equivalent current at their interfaces. Without loss of generality, Figure 4.2 uses a T-shaped device to illustrate this idea. Terminals 1 and 2 consist of closed dark surfaces surrounding the arms of the device. The currents in the transmission lines connected to these bands represent the tangential magnetic field at the interfaces. The total terminal currents are found by integration of the tangential field around the bands and constitute the currents injected into the device by the equivalent Norton sources.

There is no limitation on the number or orientation of terminals as long as all the link lines associated with the terminals are accounted for in the integration process. Furthermore, the link lines may all have different characteristic impedances. The remaining surface of the device is clad with electric walls in order to provide continuity for the tangential magnetic field at the device. The common terminal can be either connected to the ground or can be floating in the TLM network. The other terminals have

their own interface regions (dark rims shown in Figure 4.2) where they are coupled to the TLM network.

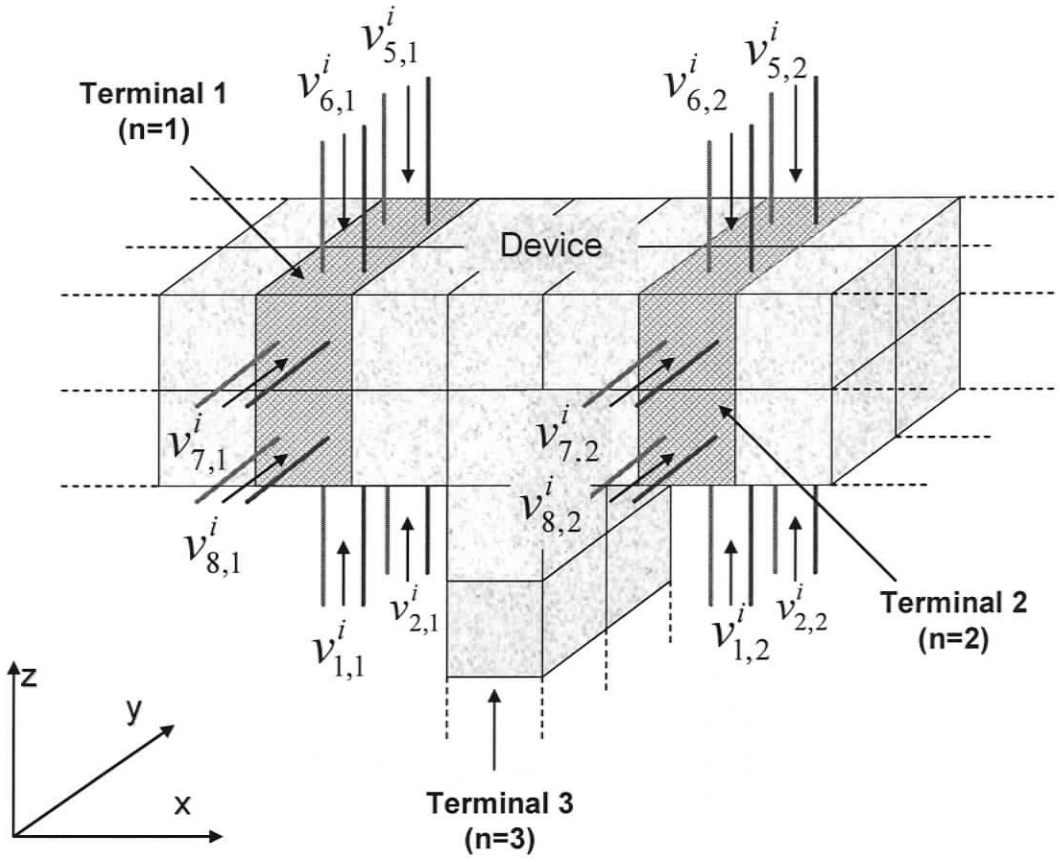

Figure 4.2 Currents in the TLM link-lines ending on the dark rings that surround the terminals of a quasi-lumped device are integrated over these interfaces to yield the Norton equivalent source currents.

In other words, the dark rims surrounding terminals 1 and 2 can be thought of as current probes coupled to the currents flowing in these terminals. Each pair of link lines that is polarized in the direction of the terminal current and ends on the dark rim of the terminal can be represented by a local Norton equivalent sub-source. All local Norton sub-sources form a loop around the terminal boundary. The total current of the resulting equivalent Norton source connected in series with the terminal is equal to the sum of the currents of all these sub-sources. The internal admittance $Y_{TLM,n} = 1/Z_{TLM,n}$ of the n^{th} Norton source is equal to the parallel combination of the characteristic admittances of all the link lines ending on the interface rim.

The switches in Figure 4.1 symbolize the discrete-time nature of the TLM impulses; they arrive at the terminals at time $k\Delta t$. The instantaneous short-circuited current of the Norton source is found by combining the currents incident in these lines that are coupled to the device. At time $k\Delta t$, the equivalent terminal sources for the n–1 terminals are characterized by:

$$Y_{TLM,n} = \frac{1}{Z_{TLM,n}} = \sum_m \frac{1}{Z_{m,n}} \tag{4.1}$$

$${}_kI^i_{TLM,n} = 2\sum_m \frac{{}_kV^i_{m,n}}{Z_{m,n}} \tag{4.2}$$

where ${}_kI_{TLM,n}$ is the total current produced by all voltage impulses incident on the link lines coupled to the device, and m is the number of cells forming the loop around the corresponding terminal. Positive current flow is always directed into the device.

Once the equivalent terminal current has been obtained, one can calculate the transient response of the lumped network for the duration of one TLM time step. The current reflected from a terminal interface back into the TLM network is the difference between the incident current and the total terminal current flowing into the device. The reflected current is split up equally into each link line and converted to voltage impulses that are injected back into the TLM mesh at the next time step.

$${}_{k+1}I^r_{TLM,n} = {}_kI^i_{TLM,n} - {}_kI_{TLM,n} \tag{4.3}$$

$${}_{k+1}V^r_{m,n} = Z_{m,n} \cdot \frac{{}_{k+1}I^r_{TLM,n}}{m} \tag{4.4}$$

The current-coupled device embedding mechanism is a dual of the voltage-coupled embedding scheme of So and Hoefer [47]. However, this current-coupled framework does have some practical advantages over its counterpart. For example, the current-coupled mechanism takes into account the entire magnetic field surrounding input and output lines to form the equivalent sources. The line integral is well defined and is not sensitive to the choice of the path of integration. On the other hand, voltage-coupled schemes rely on an appropriate choice of the integration path for the electric field.

Clearly, the choice of coupling mechanism will depend on the specific coupling situation and is subject to similar criteria as the appropriate choice of characteristic impedance in various types of transmission lines.

Both types of coupling have been implemented, tested and compared. Typical results are shown in the next section. Both methods yield identical results at low frequencies as expected. At higher frequencies, parasitic effects due to the finite size of the interface geometries are expected to appear, and they will be different for different configurations of the terminal interfaces.

4.2.2 Simulation results

In this subsection several examples are presented to compare the behavior of the two coupling methods.

A. Embedding a passive network

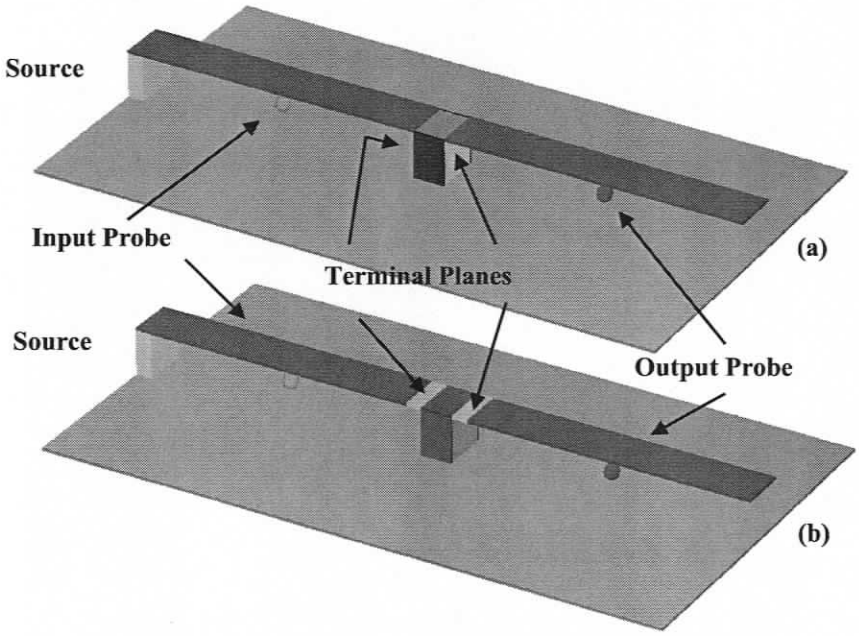

Figure 4.3 A two-port device embedded in a microstrip. The device is quasi-lumped; its dimensions are 3mm × 3mm × 2mm. The characteristic impedance of the microstrip is 126.12Ω. (a) voltage-coupled implementation. (b) current coupled implementation.

The first example in Figure 4.3 is a two-port device embedded in a microstrip line of 126Ω. Figure 4.3 (a) shows the voltage-coupled implementation in which the terminal

interfaces are the areas underneath the strips connected to the device. Figure 4.3 (b) shows the current-coupled implementation of the same device; the terminal interfaces are the rims surrounding the strips on either side of the device. Note that the device volume itself is either covered by an open-circuit boundary (a) or a short-circuit boundary (b), while the device terminals are physically located in the terminal planes.

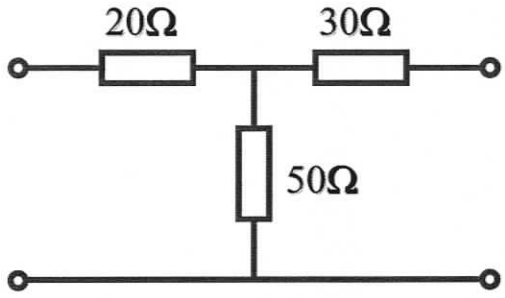

Figure 4.4 Equivalent circuit of the device embedded into the microstrip line shown in Figure 4.3.

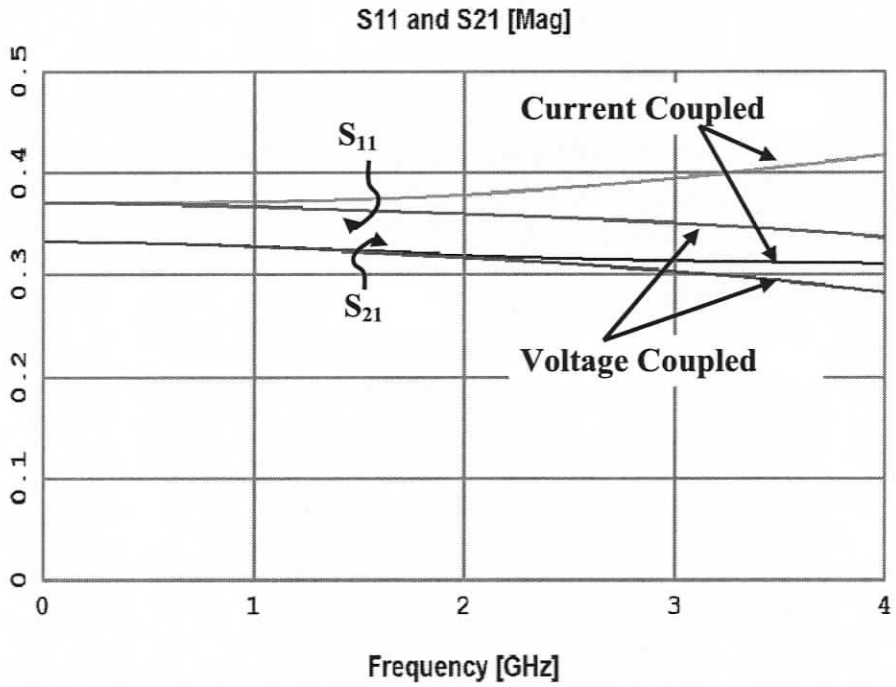

Figure 4.5 Magnitude of S-parameters of the T-network in Figure 4.4 connected to the 126 Ω microstrip line in Figure 4.3,. Results obtained with the two implementations agree at DC but diverge at higher frequencies due to parasitic and dispersive effects.

The quasi-lumped device in Figure 4.3 can be any two-port circuit such as a network of resistors, capacitors, inductors and other components. First the resistive T-network

shown in Figure 4.4 has been placed into the device volume in order to see the dispersive effects of the two implementations when computing the S-parameters of the device.

Figure 4.5 compares the S-parameters obtained with the two implementations using a 1mm resolution TLM mesh from 0 to 4 GHz. Both coupling schemes yield identical S-parameter values at low frequencies; they agree well with the theoretical values $|S_{11}|=0.371$ and $|S_{21}|=0.333$ within less than 0.1 percent. However, as the frequency increases, the two sets of results diverge from each other and also differ from the theoretical values which should be independent of frequency. This is due to the different parasitic effects introduced by the finite size terminal windows and the coarseness error produced by the rather coarse mesh used in this example.

B. Embedding an active network

In the second example the resistive T-network was replaced by the complete transistor amplifier shown in Figure 4.6 , and the transient responses obtained with the two coupling schemes are compared in Figure 4.7.

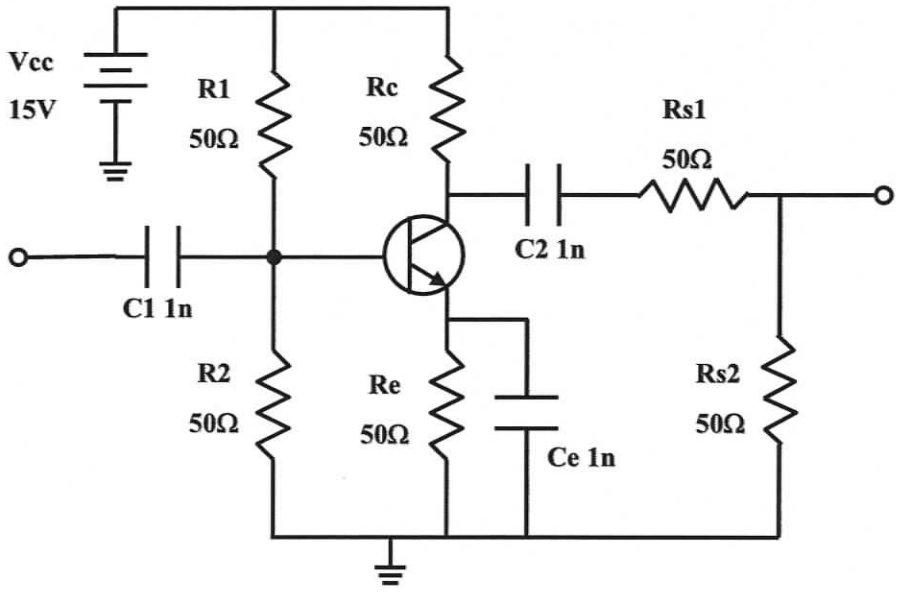

Figure 4.6 Transistor amplifier embedded into the microstrip line shown in Figure 4.3. The amplifier network is modeled by SPICE and the microstrip field space is modeled by 3D-TLM.

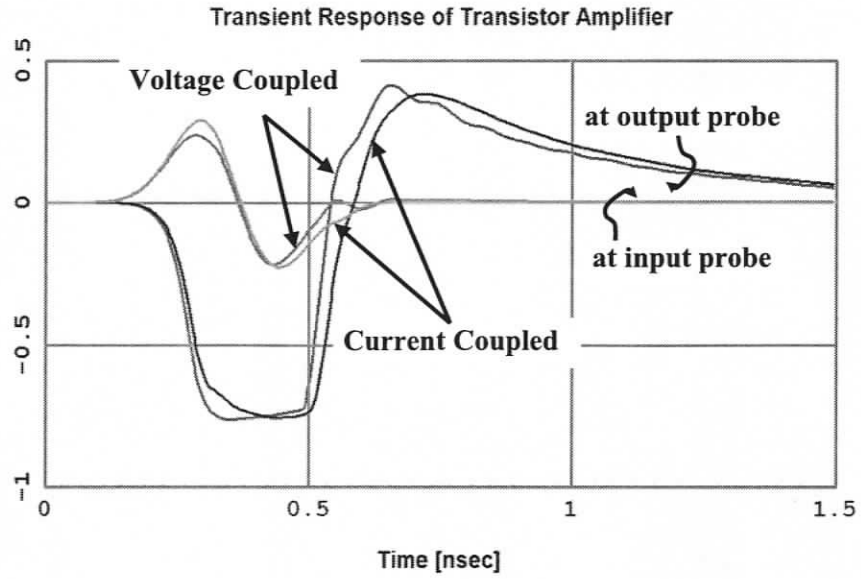

Figure 4.7 Transient response of the transistor amplifier embedded into the microstrip line shown in Figure 4.3 using SPICE and 3D-TLM.

Figure 4.7 shows the time response of the embedded amplifier to a Gaussian input of 1V amplitude and a 3 dB bandwidth of 4 GHz. Again, differences in the parasitic effects of the two embedding schemes result in slight differences in their transient responses.

The above numerical results indicate that both the voltage-coupled and the current-coupled schemes yield identical results at low frequencies. However, as frequency increases, differences between the embedding schemes become apparent. This reflects the difference in the parasitics associated with the schemes. The discrepancy is due to the difference in the coupling locations and mechanisms.

As a general rule, current-coupled embedding would be preferable in situations where terminal voltages cannot be defined in a unique way, but current flowing into a terminal is uniquely defined. On the other hand, voltage-coupled embedding yields excellent results when the fields are well contained and the mode of propagation is essentially TEM. Furthermore, current-controlled embedding methodology is quite flexible and does not require the definition of a reference potential within the field model.

4.3 Introducing S-parameter to PSPICE

This section describes the embedding of the results of a field simulation into a SPICE circuit simulation in the form of an analog behavioral model (ABM). The SPICE ABM is

characterized by its Scattering Parameters which are extracted from a full-wave time domain analysis.

4.3.1 Theoretical background

The ABM feature of PSPICE is a very powerful tool, but it has a hidden inherent non-causality problem. This problem is rooted in the definition of the Fourier transform. Equations (4.5) and (4.6) show the familiar Fourier transform pairs that yield frequency domain parameters from time-domain simulation results and vice versa.

$$F(j\omega) = \int_{-\infty}^{\infty} f(t) e^{-j\omega t} dt \tag{4.5}$$

$$f(t) = \frac{1}{2\pi} \int_{-\infty}^{\infty} F(j\omega) e^{j\omega t} d\omega \tag{4.6}$$

However, using these two equations to transform signals back and forth between the time domain and the frequency domain may give surprising results because of the infinite integral limits. Truncation of the integral limits and approximation of the residual errors often lead to results that are quite different from what one would expect intuitively.

In PSPICE, the Analog/Digital Equivalent Parts (A/D-Equivalent Parts), such as ELAPLACE, GLAPLACE, EFREQ, and GFREQ, are characterized by output that depends on the current input as well as the input history. These equivalent parts apply the inverse Fast Fourier Transform to an input frequency expression to obtain an impulse response, and then convolve the impulse response with a given dependent source to obtain the desired output in the time-domain. If the amplitude of the frequency expression, $A(\omega)$, for any reason, does not meet the Paley-Wiener criterion given in equation (4.7),

$$\int_{-\infty}^{\infty} \frac{\left|\ln A(\omega)\right|}{1+\omega^2} d\omega < \infty \tag{4.7}$$

the inverse Fourier Transform will result in a non-causal impulse response of the system. This means that the computed impulse response is non-zero even at times preceding the application of the stimulus, and the time convolution must be applied to both past and future samples of the input in order to properly construct a present time response [54].

The problem with the aforementioned convolution is that PSPICE only has the present and past values of the source; hence the convolution procedure can only account for the contribution due to these inputs, and the output due to the future input cannot be accounted for. Furthermore, PSPICE cannot compute the $f(t)$ in equation (4.6) to any desirable accuracy because the maximum number of frequency points allowed in its equivalent modules is 8192 [55]. PSPICE can detect, but cannot fix a non-causal condition; the software issues a warning message when this condition occurs. The message tells what percentage of the impulse response is non-causal. Non-causality in the order of 1% or less is usually not critical to the simulation results. If the error is larger than 1%, then PSPICE suggests adding a delay factor in the frequency response to slide the non-causal part into a causal region [55]. However, this would introduce unwanted distortion in the time-domain results. A new ABM has thus been developed to tackle the non-causality problem without using the delay factor.

4.3.2 Implementation of the new analog behavioral model

A new ABM based on the traditional microwave network theory for two-port elements has been developed. PSPICE does not have a built-in two-port element that can be used to model arbitrary two-port networks containing lumped element circuits and distributed element circuits, but its capability can be augmented by making use of its frequency-domain device model to build an analog behavioral module. This section discusses the key issues for building such a two-port module using PSPICE's A/D-Equivalent models for transient analysis; the approach can be applied to DC and AC excitations because they are just special cases of transient analysis.

Figure 4.8 depicts a schematic of the new two-port analog behavioral module connected to a generator with internal impedance Z_{ss} and a load impedance Z_{LL}, respectively. The ABM module comprises four PSPICE E-devices and necessary circuitry; together, they transform the frequency-dependent parameters S_{11}, S_{21}, S_{12}, and S_{22} into equivalent SPICE time domain responses. The internal details of the ABM module are shown in Figure 4.9.

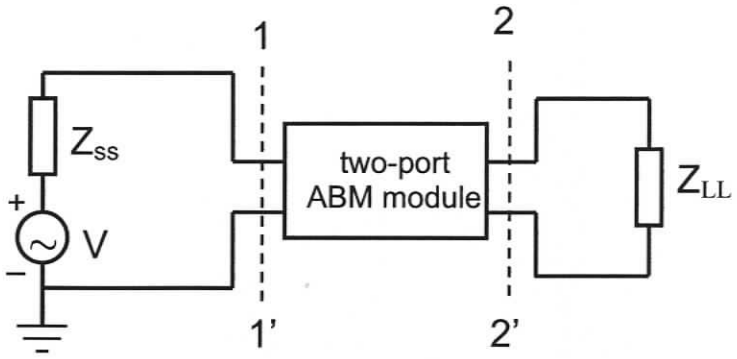

Figure 4.8 A schematic of the new two-port ABM module connected to source and load impedances.

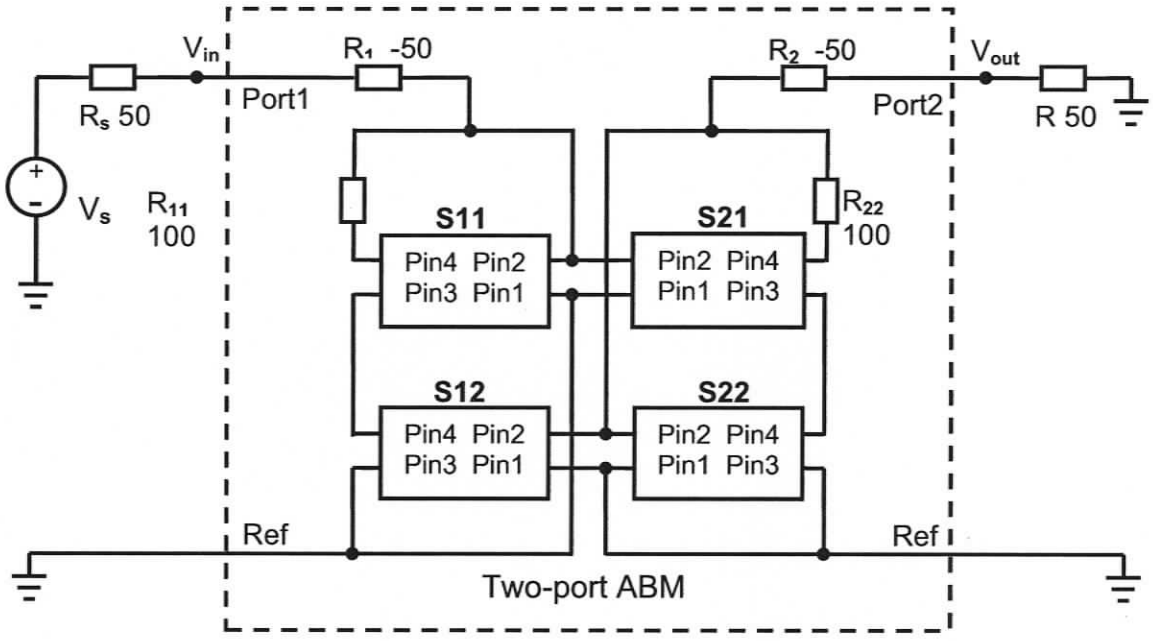

Figure 4.9 The internal detail of the new two-port analog behavioral module.

This ABM module in Figure 4.8 is capable of representing a two-port circuit with full electrical details from DC to the desired upper frequency. Any input signal with a frequency spectrum that lies within that frequency range can be used to excite the ABM circuit. In order for PSPICE to make use of the S-parameters, the data must be stored in a PSPICE readable library file formatted as a table which contains the amplitude and phase of the S-parameter at each frequency as shown in Figure 4.10.

```
S12.lib file:
.subckt S12 1 2 3 4
E1 4 3 FREQ{V(2,1)} MAG(
*S12 [Smith]
*Frequency Magnitude Phase
+(0,          0.996238   0)
+(2500310,  0.996236   -
0.124298)
+(5000630,  0.996232   -
0.248595)
+(7500940,  0.996225   -
```

Figure 4.10 An example of the library file.

Furthermore, the following criteria should be observed in order to obtain an accurate representation of the original circuit:

- The upper frequency limit in the S-parameter table must be at least five times the 3dB bandwidth of the excitation input signal. Lack of high frequency information leads to errors in the transient response. A sufficiently wide frequency range also can reduce non-causal percentage.
- The angle of the S-parameters in the library file should change continuously without 180 degree phase jumps.
- Frequency must increase monotonously from DC to the maximum frequency in the S-parameter table.
- Use as many frequency points as possible. The maximum number accepted by PSPICE is 8192.
- If the S-parameters are generated by a numerical field solver, the mesh parameter must be less than one tenth of the spatial wavelength corresponding to the highest frequency of interest. This frequency is referred to as the maximum frequency in the S-parameter table.

4.3.3 Validation results

A. . Resistive T-network

In the first validation example a resistive lumped-element two-port network as shown in Figure 4.11 is used to verify the ABM model. This network has two 50 Ω Thévenin equivalent voltage sources. The theoretically calculated S-parameters of this network are introduced in the ABM model by means of a library file as S-parameter tables. The S-parameter tables have five hundred frequency points spaced equally from DC to 20 GHz.

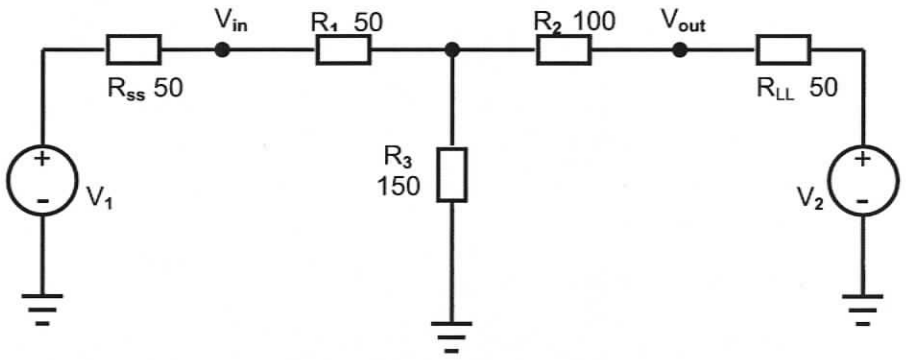

Figure 4.11 A two-port resistive T-network connected to two voltage sources.

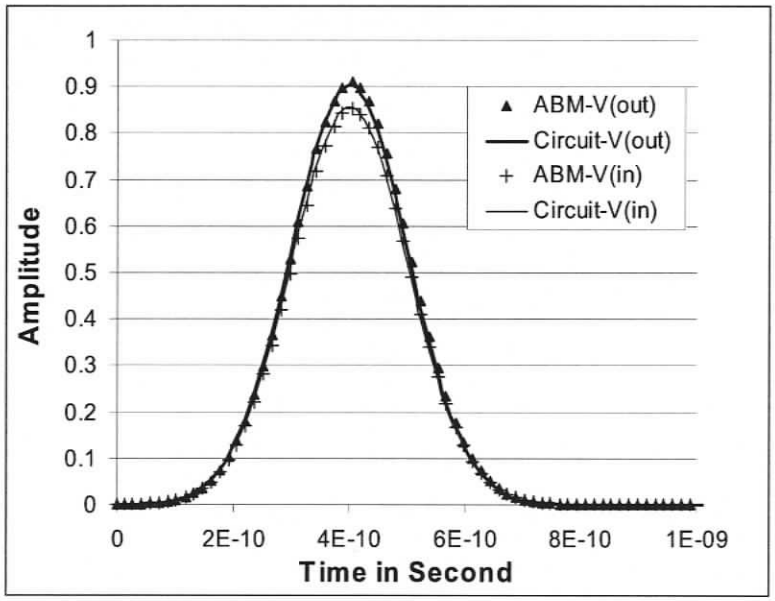

Figure 4.12 Comparison of the transient responses obtained from the ABM model and the original circuit.

The transient responses of the ABM and of the original lumped element circuit are compared in Figure 4.12. In both case, the excitation signals are Gaussian impulses of sigma (σ) = 0.1ns and mean (μ) = 0.4ns (which corresponds to a 3dB frequency bandwidth of 3.76GHz). Figure 4.12 shows that the responses obtained by these two methods are virtually identical.

B. General T network

In the second example a general RLC lumped-element two-port network containing inductances and capacitances as shown in Figure 4.13 is used to verify the ABM model. The example is quite similar to the previous one; the main difference between them is that the S-parameters in this example are frequency-dependent.

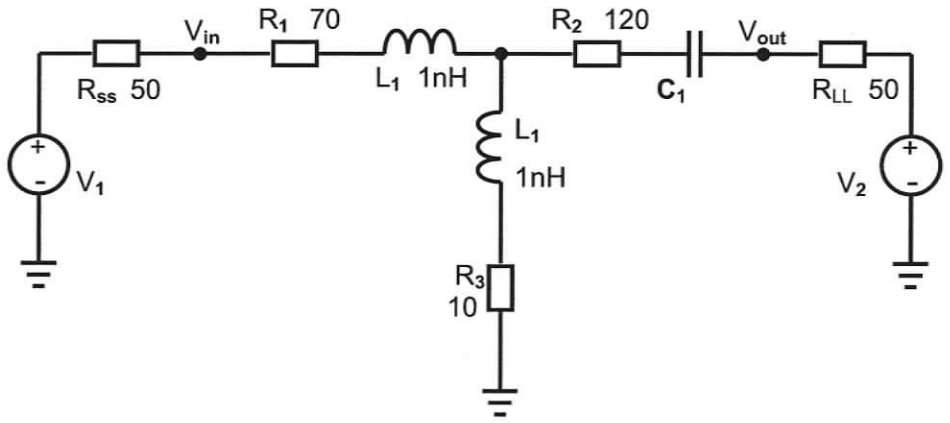

Figure 4.13 A two-port RLC T-network connected to two voltage sources.

In this case, the excitation is the same as in the previous validation example. The pre-calculated S-parameters of this network are introduced in the ABM model by means of a library file as S-parameter tables. As in the previous example, the S-parameter tables have five hundred frequency points spaced equally from DC to 20 GHz. The transient responses of the ABM and that of the lumped circuit model measured at the two probe locations are shown in Figure 4.14. The good agreement in this example demonstrates that this ABM implementation is valid even for two-port networks with dispersive S-parameters.

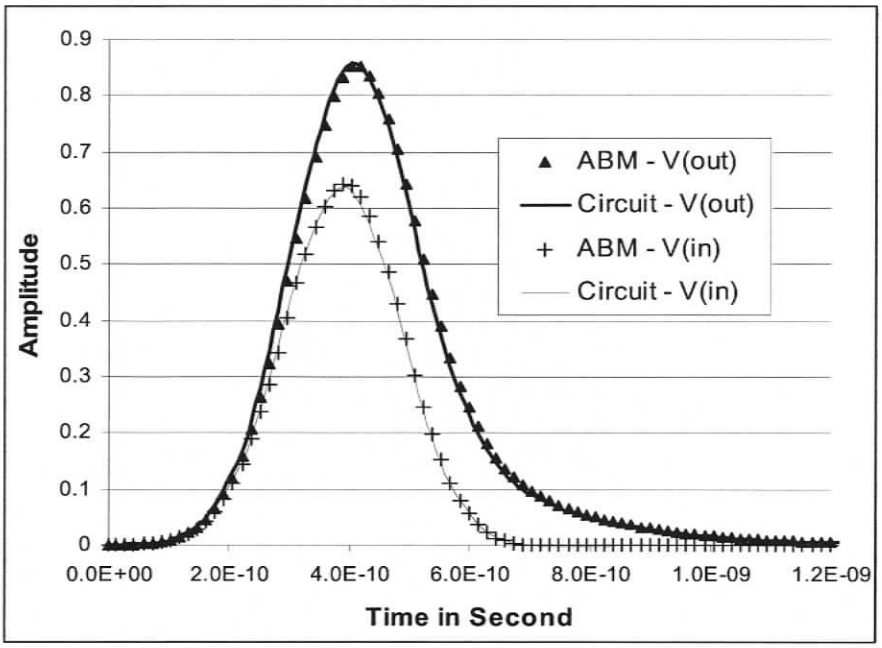

Figure 4.14 Comparison of transient responses of the ABM model and the original circuit.

C. Full-wave field simulation

In the third example a spiral inductor in a SOIC-8 package as shown in Figure 4.15 is modeled using a full-wave field solver, MEFiSTo-3D Pro, to obtain the S-parameters for introduction into the ABM in PSpice. The entire computational domain in Figure 4.15 is $6.0\times4.9\times1.5$ mm^3. The mother board substrate is 0.2mm thick, and its relative permittivity is 10. The housing dielectric is 0.8mm thick and has a relative permittivity of 4. In MEFiSTo-3D Pro a mesh of 0.025mm resolution has been used to calculate the S-parameters from DC to 150GHz at 8000 equally spaced frequency points.

Figure 4.16 shows the transient responses of the spiral inductor obtained with MEFiSTo-3D Pro and PSpice simulations due to a Gaussian impulse excitation ($\sigma = 13.25$ps and $\mu = 56.22$ps, which corresponds to a 3dB frequency band-width of 28.4GHz). The comparison shows that the PSpice-ABM accurately reproduces the full wave field simulation results.

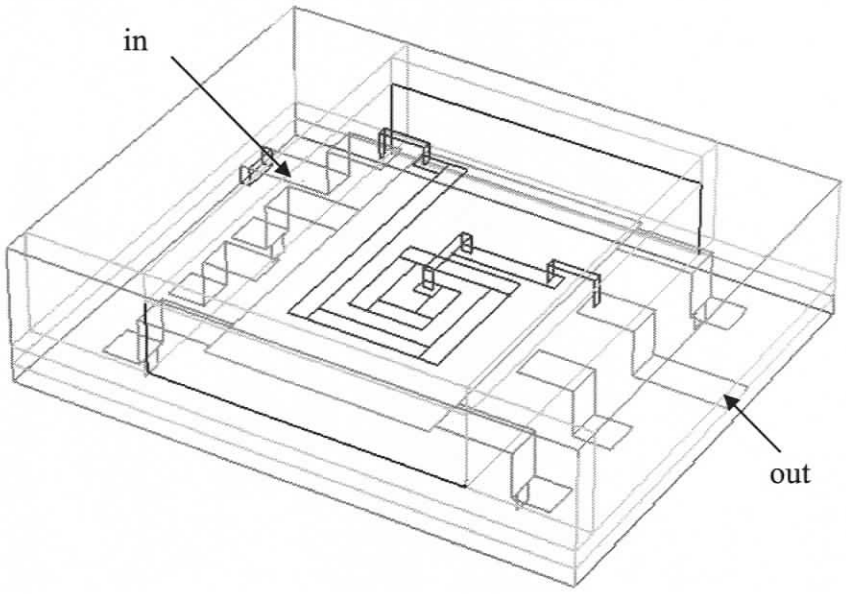

Figure 4.15 A spiral inductor in a SOIC-8 package.

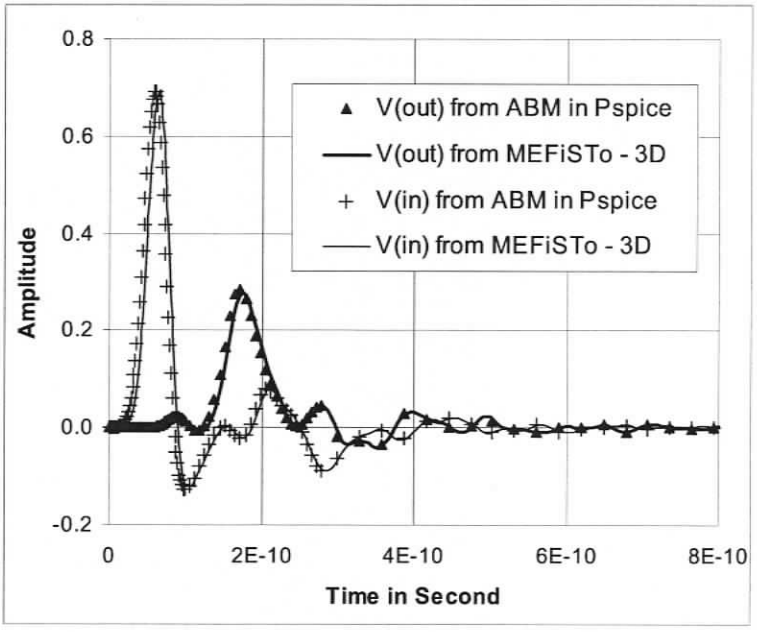

Figure 4.16 Transient responses of the packaged spiral inductor computed with MEFISTO-3D PRO and with the PSPICE behavioral model.

4.4 Conclusions

Two new methods for interfacing field and circuit models have been presented in this chapter. The first method is a current-coupled mechanism that embeds lumped network into three-dimensional TLM field space. The second method, on the other hand, embeds

the behavior of a three-dimensional full wave field simulation into a lumped PSPICE circuit model via S-parameter files. Both techniques link field analysis and circuit analysis in the time-domain by replacing the embedded substructure with a reduced-order model. The Analog Behavioral Model technique offers the capacity to model complex systems containing components represented at various levels, such as lumped circuits, distributed components and field-based models.

Chapter 5

Inter-cell Network Framework in TLM

5.1 Need for the inter-cell network framework

In Chapter 4, a current-coupled algorithm for embedding lumped element networks into TLM models has been developed. This method makes it possible for an equivalent SPICE circuit model or behavioral model to work with a TLM field solver. The restriction of this method is that the volume of the embedded lumped network should occupy at least one TLM cell. In certain situations, one may need to embed models that are smaller than the mesh resolution imposed by the field solver. This chapter addresses and tackles this restriction by means of the inter-cell network concept.

Another reason for developing the inter-cell network framework is that traditionally the properties of materials are introduced by adding shunt and/or series stubs to the nodes [56],[57]. This approach works well for simple material properties, but the scattering matrix can become quite large, especially in 3D-TLM modeling, when the materials have more complex properties. For example, the impulse scattering matrix of a 3D TLM SCN node modeling arbitrary positive permittivity and permeability is an 18x18 matrix. The modeling of negative permittivity and permeability requires a node impulse scattering matrix of size 9x9 in 2D TLM and 27x27 in 3D TLM [58]. Not only are those big matrices hard to derive, but they also increase the computational burden. Therefore, an alternative inter-cell network framework is needed to deal with problems such as modeling materials with unusual and/or complex properties.

5.2 Inter-cell network framework concept

The purpose of an inter-cell network is to introduce scattering elements in the form of lumped networks or other functional structures between cells to describe material properties without modifying the standard TLM scattering procedure at the nodes [59]. However, it involves additional processing of impulses exchanged between neighboring nodes and at boundaries. The inter-cell network is usually a two-port of zero physical length inserted between neighboring cells in a TLM mesh.

The inter-cell networks described in this chapter are suitable for both the 2D shunt node and the 3D SCN node. In the 2D shunt mesh (Figure 5.1), the two-port lumped circuit is located halfway between two nodes (at cell boundaries); for the 3D SCN mesh, two-lumped circuits are needed, one for each direction of polarization (Figure 5.2). Actually, the inter-cell network could be specified by various means, such as equivalent circuits, differential equations, behavioral models, experimental data, or even nonlinear SPICE modules. The inter-cell network may be used to model special boundaries, small material sub-regions or a general material occupying the entire computational domain.

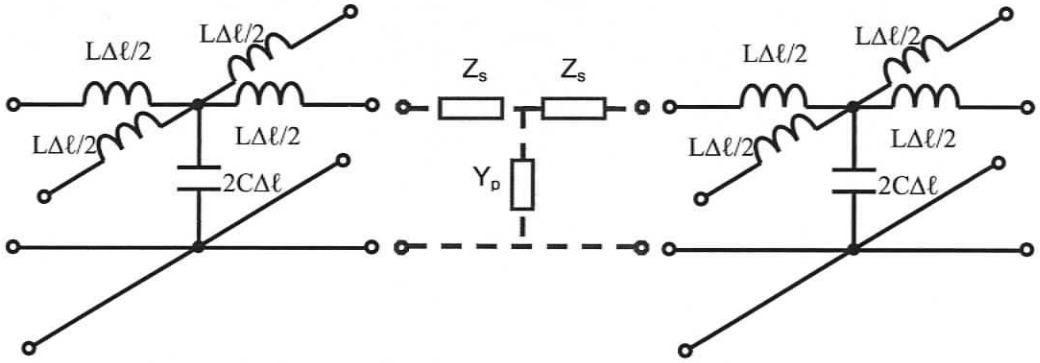

Figure 5.1 Inter-cell network inserted between two TLM shunt nodes.

Figure 5.1 and Figure 5.2 depict the connection between two shunt nodes and two SCN nodes, respectively, via a two-port inter-cell network. In general, the lumped network may contain a combination of shunt and series resistances, capacitances and inductances. These can model losses, dielectric permittivity and magnetic permeability, Debye dispersion, Lorentz dispersion and metamaterial (negative refractive index) properties. For example, the inter-cell networks shown in Figure 5.3 may model materials with positive (a) and negative (b) constitutive parameters, respectively.

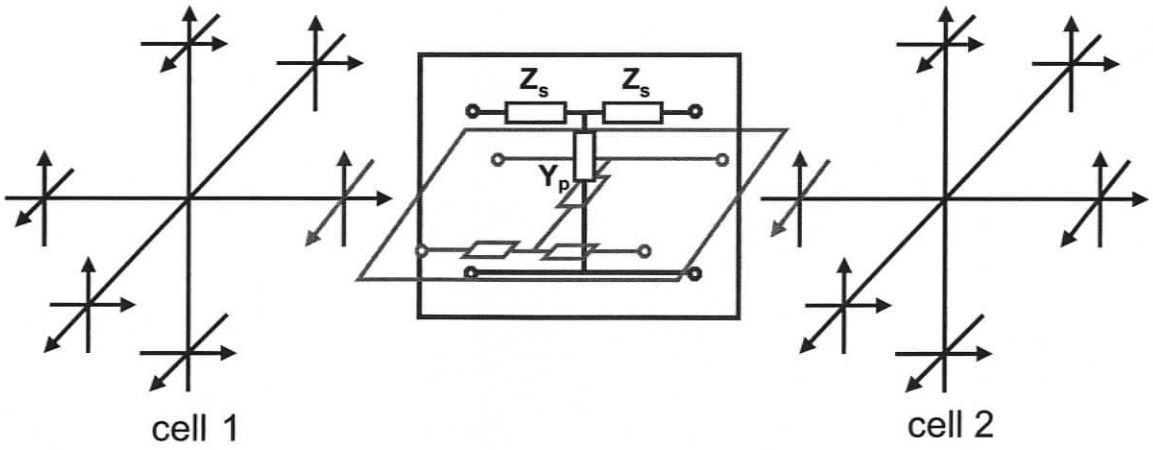

Figure 5.2 Inter-cell networks inserted between two SCN nodes in 3D TLM (one for each polarization).

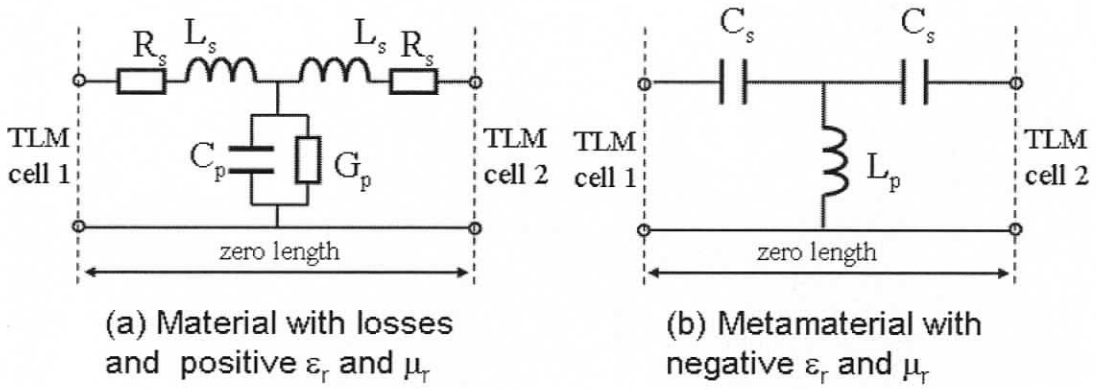

Figure 5.3 Inter-cell LCR T-networks for modeling materials (a) with losses and arbitrary positive permittivity and permeability, (b) with negative permittivity and permeability.

5.3 A new interpretation of material properties in TLM

5.3.1 Distributed network model of a 2D continuous medium

A generic network model for 2D electromagnetic wave propagation in an isotropic medium of permittivity ε_m and permeability μ_m is shown in Figure 5.4 [60].

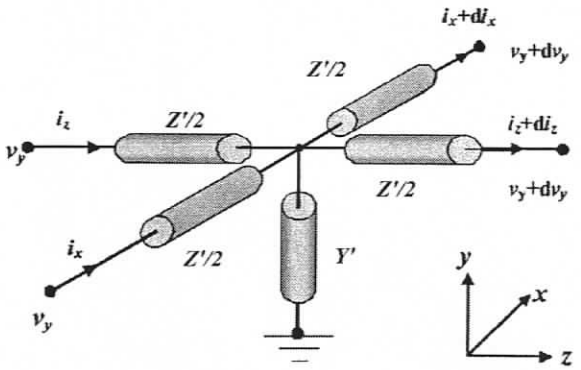

Figure 5.4 Unit cell of a 2D distributed network that models a two-dimensional continuous medium at low frequencies (wavelength >> cell size). The elements are labeled in units of impedance and susceptance per unit length, respectively. (After Eleftheriades *et al.* [60]).

The series and shunt elements Z' and Y', given in units of complex impedance (Ω/m) and complex admittance per unit length (S/m), are related to the constitutive parameters of the modeled continuous medium by the following equivalences [60]:

$$j\omega\mu_m = Z'; \qquad j\omega\varepsilon_m = Y' \tag{5.1}$$

The shunt admittance Y' is, in fact, the sum of the shunt admittances of the two orthogonal transmission lines. If both ε and μ are positive the material is also called a right-handed medium (conventional material), but if both ε and μ are negative the material is called a left-hand medium (metamaterial) because the E, H and k vectors form a left-handed triplet, and the phase velocity is anti-parallel to the flow of energy and the group velocity.

From TLM theory we know that in a 2D TLM shunt node mesh that models a material with a phase velocity v_m and characteristic impedance Z_m, both the link-line velocity $v_{\ell 0}$ and the link-line impedance $Z_{\ell 0}$ are equal to $\sqrt{2}$ times these values (see Table 5.1). (Note that the index m refers to the properties of the material, while the index ℓ refers to the properties of the TLM link lines. The impedance Z_m is also known as the Bloch impedance in the theory of periodic structures).

This relationship can be interpreted by assuming that in the 2D TLM model, the link-lines have a permeability equal to the material permeability μ_m, and a permittivity half that of the material permittivity ε_m. Hence:

$$Z' = Z'_\ell , \quad Y' = 2Y'_\ell \tag{5.2}$$

	Phase velocity	Impedance
Material	$v_m = 1/\sqrt{\varepsilon_m \cdot \mu_m}$	$Z_m = \sqrt{\mu_m / \varepsilon_m}$
2D TLM link lines	$v_{\ell 0} = \sqrt{2}/\sqrt{\varepsilon_m \cdot \mu_m}$	$Z_{\ell 0} = \sqrt{2} \cdot \sqrt{\mu_m / \varepsilon_m}$

Table 5.1 Relationship between the properties of a material and those of the link lines of its 2D TLM model.

The generic network model for 2D electromagnetic wave propagation in an isotropic medium of permittivity ε and permeability μ is shown in Figure 5.5. Hence:

$$Z'_\ell = j\omega\mu_m \quad , \quad Y'_\ell = j\omega\frac{\varepsilon_m}{2} \tag{5.3}$$

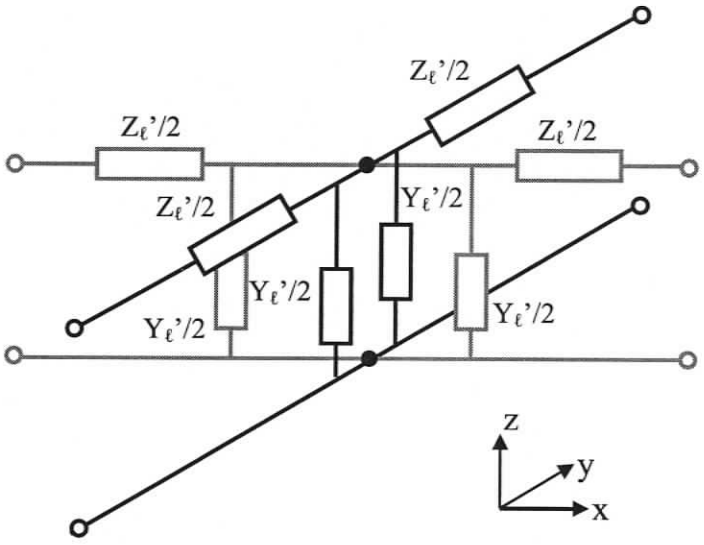

Figure 5.5 Unit cell of a 2D TLM network that models a two-dimensional continuous medium using the shunt node. The elements are labeled in units of impedance and susceptance per unit length, respectively.

The above situation can also be represented by an unloaded 2D shunt node connected to inter-cell networks as shown in Figure 5.6. There, $Z'_{\ell 0} = j\omega\mu_0$ and $Y'_{\ell 0} = j\omega\varepsilon_0/2$ are the host TLM 2D shunt node parameters in each cell. In order to ensure that this model is equivalent to the model shown in Figure 5.5, we must have

$$Z_\ell' \Delta\ell = j\omega\mu_m \Delta\ell = Z_{\ell 0}' \Delta\ell + 2Z_{ssx} = j\omega\mu_0 \Delta\ell + 2Z_{ssx} \tag{5.4}$$

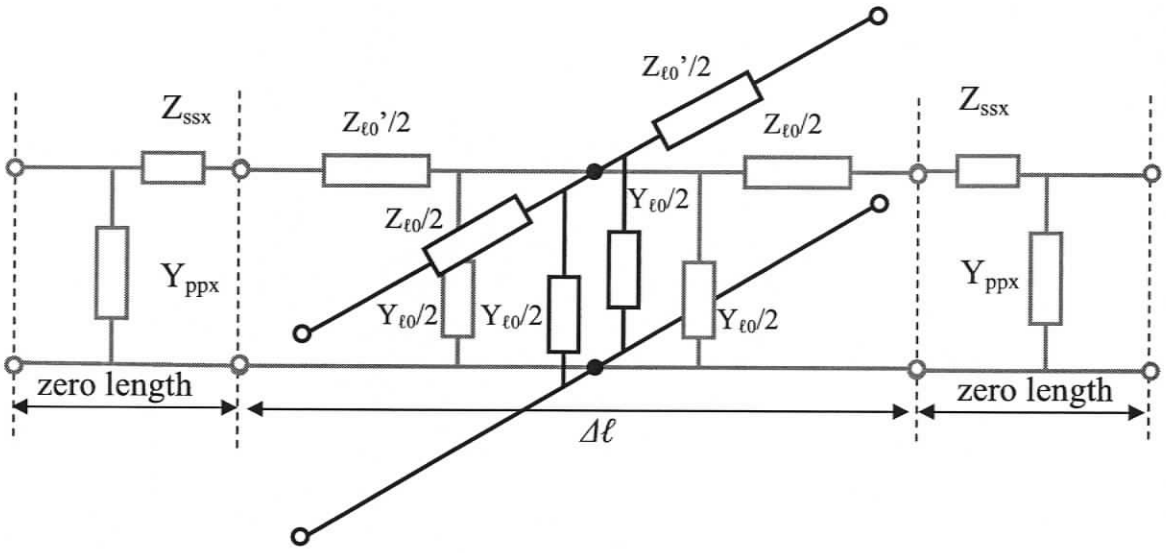

Figure 5.6 A shunt node with inter-cell networks to represent material properties in 2D TLM.

$$Y_\ell' \Delta\ell = j\omega \frac{\varepsilon_m}{2} \Delta\ell = Y_{\ell 0}' \Delta\ell + 2Y_{ppx} = j\omega \frac{\varepsilon_0}{2} \Delta\ell + 2Y_{ppx} \tag{5.5}$$

Solving (5.4) and (5.5) for Z_{ssx} and Y_{ppx} yields:

$$Z_{ssx} = \frac{j\omega\Delta\ell(\mu_m - \mu_0)}{2} \qquad Y_{ppx} = \frac{j\omega\Delta\ell(\varepsilon_m - \varepsilon_0)}{4} \tag{5.6}$$

Positive Z_{ssx} and Y_{ppx} can be represented by a lumped inductor ($Z_{ssx} = j\omega L_{ssx}$) and a lumped capacitor ($Y_{ppx} = j\omega C_{ppx}$) respectively. Hence:

$$L_{ssx} = \frac{\Delta\ell(\mu_m - \mu_0)}{2} \qquad C_{ppx} = \frac{\Delta\ell(\varepsilon_m - \varepsilon_0)}{4} \tag{5.7}$$

On the other hand, negative Z_{ssx} and Y_{ppx} can be represented by a lumped capacitor ($Z_{ssx} = 1/j\omega C_{ssx}$) and a lumped inductor ($Y_{ppx} = 1/j\omega L_{ppx}$) respectively. Hence:

$$C_{ssx} = -\frac{2}{\omega^2(\mu_m - \mu_0)\Delta\ell} \tag{5.8}$$

$$L_{ppx} = -\frac{4}{\omega^2(\varepsilon_m - \varepsilon_0)\Delta\ell} \tag{5.9}$$

Note that when Z_{ssx} and Y_{ppx} are positive, the capacities and inductance of the inter-cell network are independent of frequency, however, when Z_{ssx} and Y_{ppx} are negative, they are frequency dependent.

5.3.2 Distributed network model of a 3D continuous medium

The parameters for the three-dimensional SCN TLM model of such media can be derived using the same procedure. In the 3D SCN mesh, the velocity and characteristic impedance in the medium and on the link-lines are related as follows.

	Phase velocity	Impedance
Material	$v_m = 1/\sqrt{\varepsilon_m \cdot \mu_m}$	$Z_m = \sqrt{\mu_m / \varepsilon_m}$
3D TLM link lines	$v_\ell = 2/\sqrt{\varepsilon_m \cdot \mu_m}$	$Z_\ell = \sqrt{\mu_m / \varepsilon_m}$

Table 5.2 Relationship between the properties of a material and those of the link lines of its 3D TLM model.

This relationship can be interpreted by assuming that in the 3D TLM model the link-lines have a permeability of $\mu_m/2$ and a permittivity of $\varepsilon_m/2$. Hence:

$$Z_\ell^{'} = j\omega\mu_m/2 \quad , \quad Y_\ell^{'} = j\omega\varepsilon_m/2 \tag{5.10}$$

The generic network model for 3D electromagnetic wave propagation in an isotropic medium of permittivity ε and permeability μ is shown in Figure 5.7. This figure only shows the lumped element circuit deployed in x-direction and polarized in z-direction. Similar circuits can be drawn for the two other coordinate directions. Hence:

$$Z_{x\ell}^{'} = Z_{y\ell}^{'} = Z_{z\ell}^{'} = j\omega\mu_m/2 \qquad Y_{x\ell}^{'} = Y_{y\ell}^{'} = Y_{z\ell}^{'} = j\omega\varepsilon_m/2 \tag{5.11}$$

The inter-cell network in the previous section can be used to represent the relative permittivity and permeability of the above medium as shown in Figure 5.8. With that representation, the series and shunt elements at the SCN node would only be used to represent μ_0 and ε_0; that is that $Z_{\ell 0}^{'} = j\omega\mu_0/2$ and $Y_{\ell 0}^{'} = j\omega\varepsilon_0/2$ are the intrinsic 3D SCN node parameters. The line parameters for these two models are related as follows:

$$Z_{x\ell}^{'}\Delta\ell = j\omega\frac{\mu_m}{2}\Delta\ell = Z_{\ell 0}^{'}\Delta\ell + 2Z_{ssx} = j\omega\frac{\mu_0}{2}\Delta\ell + 2Z_{ssx} \tag{5.12}$$

$$Y'_{x\ell}\Delta\ell = j\omega\frac{\varepsilon_m}{2}\Delta\ell = Y'_{\ell 0}\Delta\ell + 2Y_{ppx} = j\omega\frac{\varepsilon_0}{2}\Delta\ell + 2Y_{ppx} \tag{5.13}$$

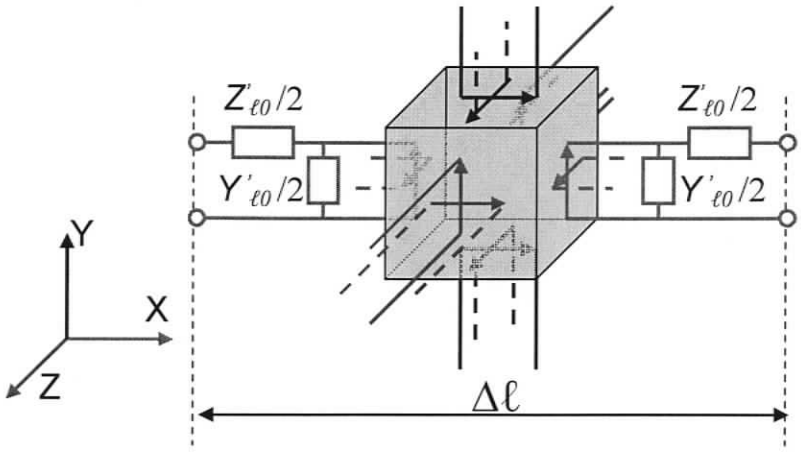

Figure 5.7 Unit cell of a 3-D TLM network that models a three-dimensional continuous medium using the Symmetrical Condensed Node (SCN). The elements are labeled in units of impedance and susceptance per unit length, respectively.

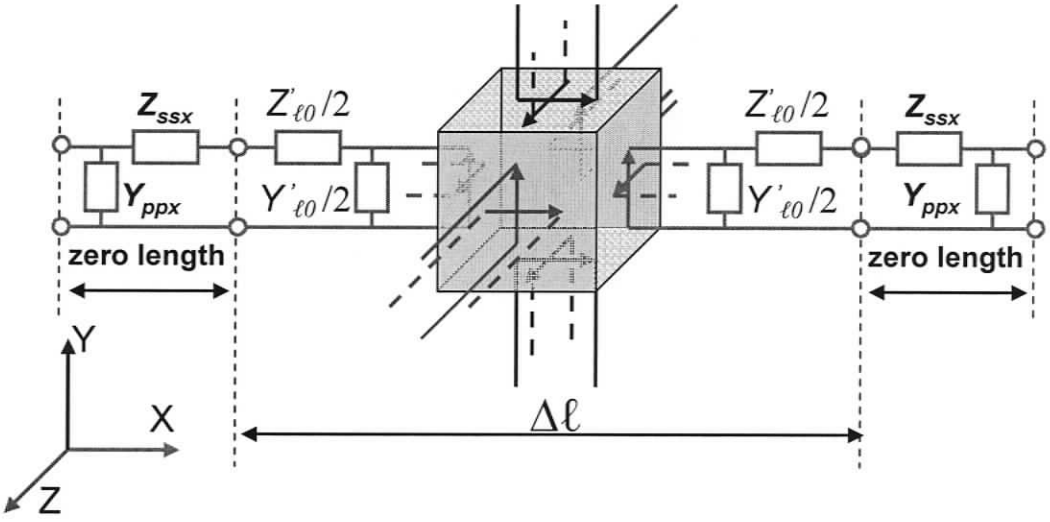

Figure 5.8 SCN node with inter-cell networks to represent material properties in 3D TLM.

Solving (5.12) and (5.13) for Z_{ssx} and Y_{ppx} yields:

$$Z_{ssx} = \frac{j\omega\Delta\ell(\mu_m - \mu_0)}{4} \qquad Y_{ppx} = \frac{j\omega\Delta\ell(\varepsilon_m - \varepsilon_0)}{4} \tag{5.14}$$

Positive Z_{ssx} and Y_{ppx} can be represented by a lumped inductor ($Z_{ssx} = j\omega L_{ssx}$) and a lumped capacitor ($Y_{ppx} = j\omega C_{ppx}$) respectively. Hence:

$$L_{ssx} = \frac{\Delta\ell(\mu_m - \mu_0)}{4} \qquad C_{ppx} = \frac{\Delta\ell(\varepsilon_m - \varepsilon_0)}{4} \tag{5.15}$$

On the other hand, negative Z_{ssx} and Y_{ppx} can be represented by a lumped capacitor ($Z_{ssx} = 1/j\omega C_{ssx}$) and a lumped inductor ($Y_{ppx} = 1/j\omega L_{ppx}$) respectively. Hence:

$$C_{ssx} = -\frac{4}{\omega^2(\mu_m - \mu_0)\Delta\ell} \qquad L_{ppx} = -\frac{4}{\omega^2(\varepsilon_m - \varepsilon_0)\Delta\ell} \tag{5.16}$$

Again, note that when Z_{ssx} and Y_{ppx} are positive, the capacities and inductance of the inter-cell network are independent of frequency, when Z_{ssx} and Y_{ppx} are negative, they are frequency dependent.

5.4 Realization of inter-cell networks in TLM

In both 2D and 3D TLM networks, the reactive elements of the inter-cell network can be represented either by reactive short stubs or by time domain differential equations [61]. An example for the first approach is shown in Figure 5.9.

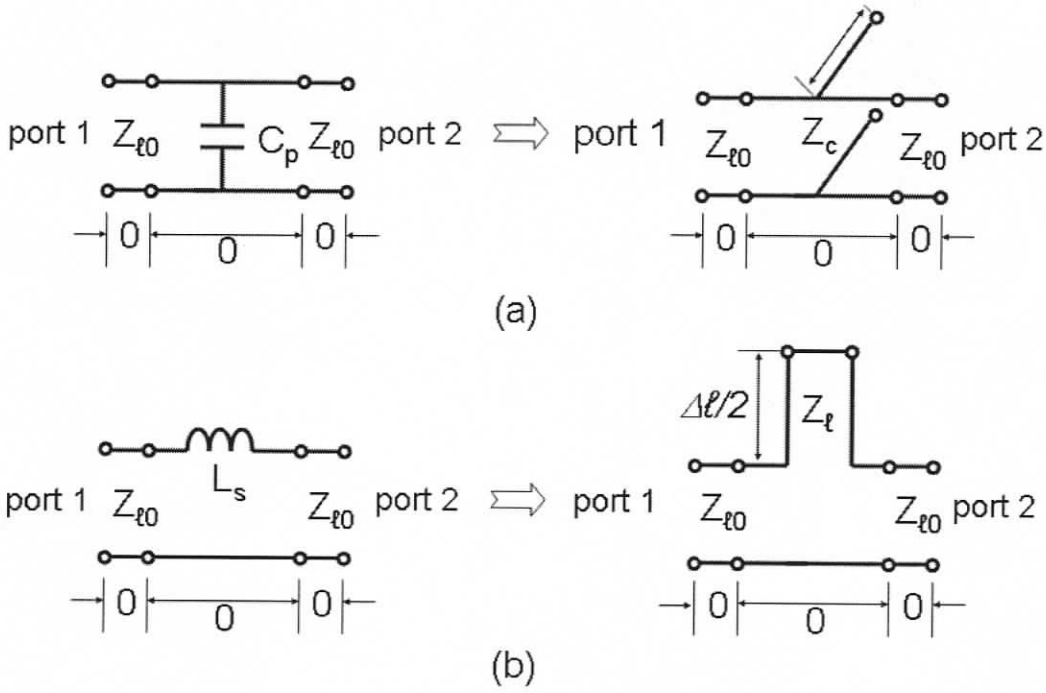

Figure 5.9 Transmission line representations of lumped reactive elements. (a) shunt capacitor, (b) series inductor.

A shunt capacitor is typically represented by an open-circuited shunt stub of length $\Delta\ell/2$ and impedance Z_c as shown in Figure 5.9 (a). Similarly, a series inductor is

represented by a short-circuited series stub of length $\Delta\ell/2$ and impedance $Z_{\ell 0}$ as shown in Figure 5.9 (b). Δl is the size of a TLM cell. With the assumption that it is much smaller than the wavelength, the characteristic impedances of the stub lines are $Z_c = \frac{\Delta l}{2 \cdot v_{\ell 0} \cdot C_s}$, $Z_\ell = \frac{2 \cdot v_{\ell 0} \cdot L_p}{\Delta l}$, where $v_{\ell 0}$ is the phase velocity of the TLM impulses on the link lines for 2D shunt node and 3D SCN node, respectively. The equivalent stub model of the lumped element inter-cell network is shown in Figure 5.10. Here $Z_{\ell 0}$ is the characteristic impedance of the host link line ($Z_{\ell 0} = \sqrt{2}\eta_0$ for the 2D shunt node, and $Z_{\ell 0} = \eta_0$ for 3D SCN node).

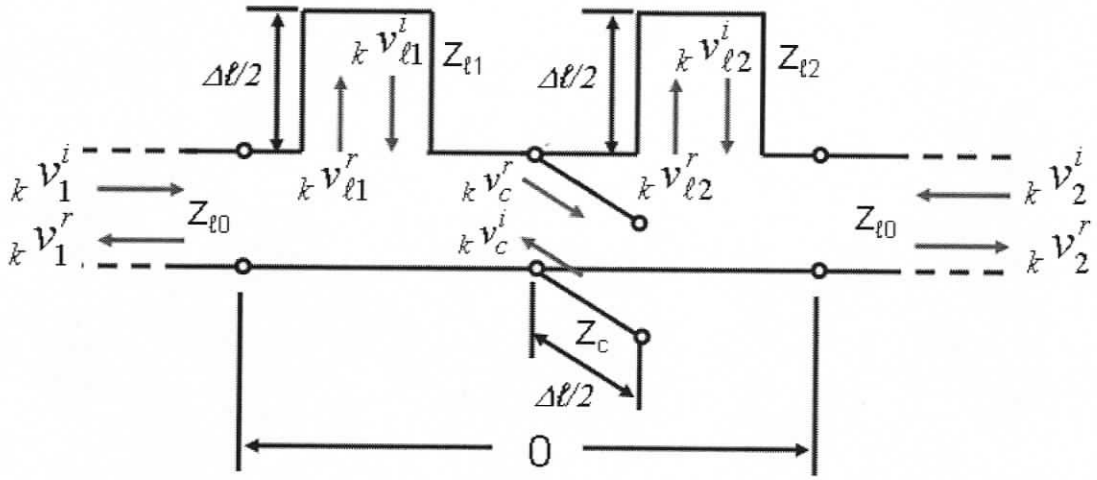

Figure 5.10 The equivalent stub model of the lumped element inter-cell network for modeling lossless materials with positive ε and μ.

Figure 5.10 is an inter-cell network for modeling arbitrary positive permittivity and permeability, realized by means of series and shunt stubs. It is a five-port junction in which three inner ports are terminated by the reactive stubs. The impulse scattering matrix of this junction is:

$$
{}_k\begin{bmatrix} v_1 \\ v_2 \\ v_{\ell 1} \\ v_{\ell 2} \\ v_c \end{bmatrix}^r = \begin{bmatrix} \alpha & \beta & \chi & -\beta & \delta \\ \beta & \alpha & -\beta & \chi & \delta \\ \kappa & -\tau & \vartheta & \tau & -\zeta \\ -\tau & \kappa & \tau & \vartheta & -\zeta \\ \xi & \xi & -\xi & -\xi & \gamma \end{bmatrix} \cdot {}_k\begin{bmatrix} v_1 \\ v_2 \\ v_{\ell 1} \\ v_{\ell 2} \\ v_c \end{bmatrix}^i \tag{5.17}
$$

where

$$\alpha = \frac{Z_\ell + Z_a - Z_{\ell 0}}{Z_\ell + Z_a + Z_{\ell 0}} \qquad \beta = \frac{2 \cdot Z_a \cdot Z_{\ell 0}}{(Z_\ell + Z_a + Z_{\ell 0}) \cdot (Z_\ell + Z_{\ell 0})} \qquad \chi = \frac{2 \cdot Z_{\ell 0}}{Z_\ell + Z_a + Z_{\ell 0}}$$

$$\delta = \frac{2 \cdot Z_b \cdot Z_{\ell 0}}{(Z_c + Z_b) \cdot (Z_\ell + Z_{\ell 0})} \qquad \kappa = \frac{2 \cdot Z_\ell}{Z_\ell + Z_a + Z_{\ell 0}} \qquad \tau = \frac{2 \cdot Z_a \cdot Z_\ell}{(Z_\ell + Z_a + Z_{\ell 0}) \cdot (Z_\ell + Z_{\ell 0})}$$

$$\vartheta = \frac{Z_0 + Z_a - Z_\ell}{Z_\ell + Z_a + Z_{\ell 0}} \qquad \zeta = \frac{2 \cdot Z_b \cdot Z_\ell}{(Z_c + Z_b) \cdot (Z_\ell + Z_{\ell 0})} \qquad \xi = \frac{2 \cdot Z_a}{Z_\ell + Z_a + Z_{\ell 0}}$$

$$\gamma = \frac{Z_b - Z_c}{Z_b + Z_c} \qquad Z_a = \frac{(Z_\ell + Z_{\ell 0}) \cdot Z_c}{Z_\ell + Z_c + Z_{\ell 0}} \qquad Z_b = \frac{Z_\ell + Z_{\ell 0}}{2}$$

The incident and reflected impulses at the inner ports are related by virtue of the delay and reflection in the stubs:

$${}_k v^i_{\ell 1} = -{}_{k-1} v^r_{\ell 1} \qquad {}_k v^i_{\ell 2} = -{}_{k-1} v^r_{\ell 2} \qquad {}_k v^i_c = {}_{k-1} v^r_c$$

5.5 Dispersion analysis of TLM models with inter-cell networks

The principal source of error in explicit time-stepping algorithms, such as TLM, is the discretization of the continuous field variables by sampling in space and time. In order to answer the question how accurately these TLM models with inter-cell networks predict the wave properties of the physical materials, we need to evaluate the discrepancy between the properties of a coarse TLM model and a smooth isotropic material.

Regardless of the type of node, the dispersion properties of all TLM schemes can be formulated using the same general matrix notation. Consider an infinite array of nodes – 2D or 3D, as the case may be. Designate any node as the central node c. In a 2D mesh, node c has four ports, each being connected to one port of a neighboring node by a link network (see Figure 5.11). In a 3D mesh, node c is surrounded by six nodes and connected to them by six orthogonal pairs of link networks, or twelve links in all. The following dispersion analysis employs the approach outlined previously by Nielsen and Hoefer [62][63]. Note that the inter-cell network must be taken into account by means of the link network scattering matrix **C**. The square or cubic unit cells such that $dx = dy = dz = d = \Delta\ell$ in the following derivations are assumed [64].

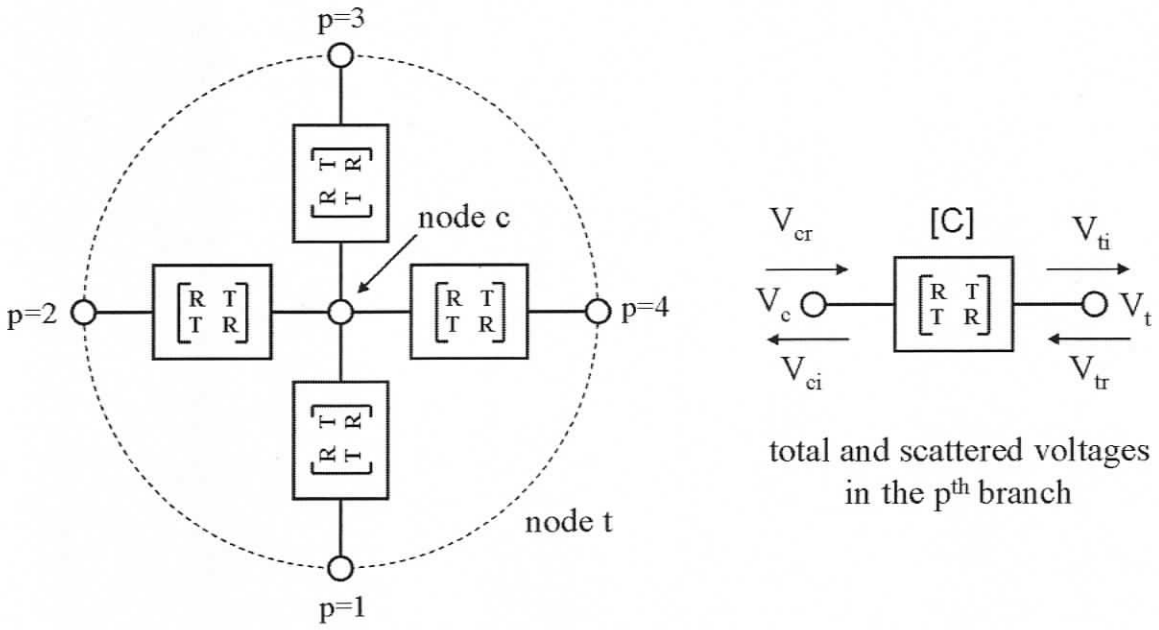

Figure 5.11 In 2D TLM, the central node c is connected to the four-port conglomerate node t by link networks which are characterized by a link scattering matrix **C**. In 3D we have 6 pairs of orthogonally polarized ports per node, requiring 12 link networks.

For the purpose of compact vector formulation it is convenient to define a virtual conglomerate node, which we shall call node t, that encompasses all the ports of the surrounding nodes connected to the node c. The following notations are used in the derivation of the general dispersion relation.

$\mathbf{V_c}$ --- the total voltage vector at the ports of node c;

$\mathbf{V_t}$ --- the total voltage vector at the ports of node t;

$\mathbf{V_{ci}}$ --- the vector of all incident voltages at node c;

$\mathbf{V_{ti}}$ --- the vector of all incident voltages at node t;

$\mathbf{V_{cr}}$ --- the vector of all reflected voltages at node c;

$\mathbf{V_{tr}}$ --- the vector of all reflected voltages at node t.

Note that in the dispersion analysis all voltages are monochromatic at a single frequency rather than Dirac-type impulses used in the actual TLM simulation. The relationship between the total voltage vectors and the incident and reflected voltage vectors is

$$\mathbf{V_c} = \mathbf{V_{ci}} + \mathbf{V_{cr}} \tag{5.18}$$

$$\mathbf{V_t} = \mathbf{V_{ti}} + \mathbf{V_{tr}} \tag{5.19}$$

The scattering matrix **S** of node c relates the vectors of incident and reflected voltages

$$\mathbf{V}_{cr} = \mathbf{S} \cdot \mathbf{V}_{ci} \tag{5.20}$$

S is identical to the impulse scattering matrix used in the formulation of the underlying TLM algorithm, even though the dispersion analysis is carried out in the frequency domain. This is due to the fact that the impulse response of the node contains all frequency components and is thus valid simultaneously at all frequencies.

The link network scattering matrix **C** relates the vectors of incident and reflected voltages at nodes c and t as follows

$$\mathbf{V}_{ci} = \mathbf{R} \cdot \mathbf{V}_{cr} + \mathbf{T} \cdot \mathbf{V}_{tr} \tag{5.21}$$

$$\mathbf{V}_{ti} = \mathbf{T} \cdot \mathbf{V}_{cr} + \mathbf{R} \cdot \mathbf{V}_{tr} \tag{5.22}$$

Introducing (5.22) into (5.19) yields

$$\mathbf{V}_{t} = \mathbf{T} \cdot \mathbf{V}_{cr} + \mathbf{R} \cdot \mathbf{V}_{tr} + \mathbf{V}_{tr} \tag{5.23}$$

And combining (5.20) and (5.21) yields

$$\mathbf{V}_{cr} = (\mathbf{I} - \mathbf{S} \cdot \mathbf{R})^{-1} \cdot \mathbf{S} \cdot \mathbf{T} \cdot \mathbf{V}_{tr} \tag{5.24}$$

I is the identity matrix. Equation (5.24) allows us to express the conglomerate node voltage vector $\mathbf{V}_t$ in (5.23) as a function of $\mathbf{V}_{tr}$.

$$\mathbf{V}_{t} = \left(\mathbf{I} + \mathbf{R} + \mathbf{T} \cdot (\mathbf{I} - \mathbf{S} \cdot \mathbf{R})^{-1} \cdot \mathbf{S} \cdot \mathbf{T}\right) \mathbf{V}_{tr} = \mathbf{W} \cdot \mathbf{V}_{tr} \tag{5.25}$$

On the other hand, by combining (5.18), (5.20) and (5.24) we obtain:

$$\mathbf{V}_{c} = \left(\mathbf{S}^{-} + \mathbf{I}\right) \cdot (\mathbf{I} - \mathbf{S} \cdot \mathbf{R})^{-1} \cdot \mathbf{S} \cdot \mathbf{T} \cdot \mathbf{V}_{tr} = \mathbf{Q} \cdot \mathbf{V}_{tr} \tag{5.26}$$

These expressions define the matrices **W** and **Q**; they depend on the scattering properties of the underlying TLM nodes and the nature of the circuits (inter-cell networks) that link adjacent nodes to each other. These links are symmetrical two-ports and can contain both transmission line sections and lumped elements or their equivalent stubs.

An additional relation between node voltages is obtained by the application of Floquet's theorem, assuming that for a time-harmonic excitation a wave of the form

$$\mathbf{V} = \mathbf{A}e^{-\mathbf{j}k_{mx}\mathbf{x}}e^{-\mathbf{j}k_{my}\mathbf{y}}e^{-\mathbf{j}k_{mz}\mathbf{z}} \tag{5.27}$$

exists in the structure. This expression allows us to relate the voltage vectors at the nodes c and t by the following matrix equation:

$$\mathbf{V}_t = \mathbf{P} \cdot \mathbf{V}_c \tag{5.28}$$

where **P** is given below for the 2D shunt and 3D SCN cases. Combination of equations (5.25), (5.26) and (5.28) yields:

$$\mathbf{V}_c = \mathbf{Q} \cdot \mathbf{W}^{-1} \cdot \mathbf{V}_t = \mathbf{Q} \cdot \mathbf{W}^{-1} \cdot \mathbf{P} \cdot \mathbf{V}_c \tag{5.29}$$

The corresponding singular value equation

$$\det\left(\mathbf{Q} \cdot \mathbf{W}^{-1} \cdot \mathbf{P} - \mathbf{I}\right) = 0 \tag{5.30}$$

is an implicit function of the propagation constants along the mesh axes, the properties of the link network and of frequency. It yields the desired general dispersion relation.

For the 2D case depicted in Figure 5.11 and the numbering scheme shown there, we obtain the following **P** matrix:

$$\mathbf{P} = \begin{bmatrix} e^{jk_{my}d} & 0 & 0 & 0 \\ 0 & e^{jk_{mx}d} & 0 & 0 \\ 0 & 0 & e^{-jk_{my}d} & 0 \\ 0 & 0 & 0 & e^{-jk_{mx}d} \end{bmatrix} \tag{5.31}$$

where d is the distance between nodes (cell size or mesh parameter). An analogous **P** matrix of size 12 x 12 is obtained for 3D SCN TLM meshes; the placement of the terms in the matrix depends on the port numbering scheme used. Using the original port numbering scheme used by Johns [57], the matrix **P** has zero entries except for the following elements:

$$\begin{aligned} P_{1,12} &= P_{5,7} = e^{jk_{my}d}, & P_{7,5} &= P_{12,1} = e^{-jk_{my}d}, \\ P_{2,9} &= P_{4,8} = e^{jk_{mz}d}, & P_{8,4} &= P_{9,2} = e^{-jk_{mz}d}, \\ P_{3,11} &= P_{6,10} = e^{jk_{mx}d}, & P_{10,6} &= P_{11,3} = e^{-jk_{mx}d}. \end{aligned} \tag{5.32}$$

In (5.31) and (5.32), k_{mx}, k_{my} and k_{mz} represent the three components of the propagation vector $\boldsymbol{k_m}$ of the Floquet wave in the TLM network, and d is the mesh parameter $\Delta\ell$.

The link network scattering matrix **C** must also be derived before the dispersion properties can be computed. The link network for 3D metamaterial models and the numerical solutions for the dispersion relation are given in Section 6.3.

Specific solutions of the general dispersion relation for TLM models with inter-cell networks will be presented and discussed in Chapter 6.

5.6 Summary

An inter-cell network framework for modeling material properties in TLM has been presented. The implementation method and the dispersion analysis have been described.

The inter-cell network framework provides a method for embedding lumped or distributed features and material with special properties into the TLM field space. Since the element behavior is introduced at the inter-cell network level, the TLM impulse scattering matrix remains unchanged. The properties of inter-cell networks can be described by various means, such as equivalent circuits, differential equations, behavioral models, experimental data, or even nonlinear SPICE modules.

Applications of the inter-cell network concept to the modeling of metamaterials with negative refractive index and of magnetized ferrite will be demonstrated in the following chapters.

Chapter 6

Modeling of Metamaterials with Negative Refractive Index in TLM

Chapter 5 describes an inter-cell network that can be used to model materials with special wave properties in TLM. The approach is employed in this chapter to model metamaterial behavior in TLM, in particular the phenomena of negative phase velocity and negative refraction in materials with negative refractive index. The dispersion properties of the metamaterial models are also presented before the validation section at the end of this chapter.

6.1 Introduction

6.1.1 Metamaterials

The investigation of artificial materials has attracted considerable attention worldwide for decades. As the name implies, artificial materials are man-made and cannot be found in nature. The first attempt at exploring the concept of "artificial" materials began in the late nineteenth century when, in 1898, Jagadis Chunder Bose conducted the first microwave experiment on twisted structures (after [65]).

In the late 1960's, Veselago [66] discussed a new class of artificial materials with negative refractive index (metamaterials); his seminal paper was purely speculative and aimed at predicting the wave solutions of Maxwell's equations in a medium in which the constitutive parameters μ and ε were both negative. Veselago predicted that in such a medium the electric field, the magnetic field and the phase velocity would form a left-handed rather than a right-handed triplet as shown in Figure 6.1. (He referred to these materials as "left-handed" for this reason). He also predicted that the phase velocity

would be opposite to the group velocity and the flow of energy, and that negative refraction would occur at interfaces between "regular" materials and materials with negative μ and ε (Figure 6.2). Consequently, such left-handed materials could focus electromagnetic waves emitted by a point source situated outside the medium. (This phenomenon will be discussed further in section 6.4). By virtue of these unusual properties, such materials could have many revolutionary applications in the microwave and optical ranges such as novel antennas, couplers and planar lenses [67],[68],[69].

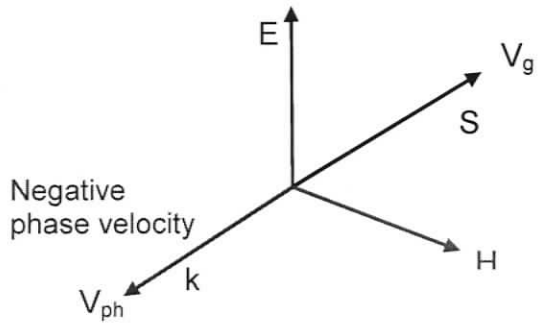

Figure 6.1 The phase velocity v_{ph} is opposite to the group velocity v_g and the flow of energy, indicated by the Poynting vector S, in metamaterials with negative μ_r and ε_r (left-handed materials).

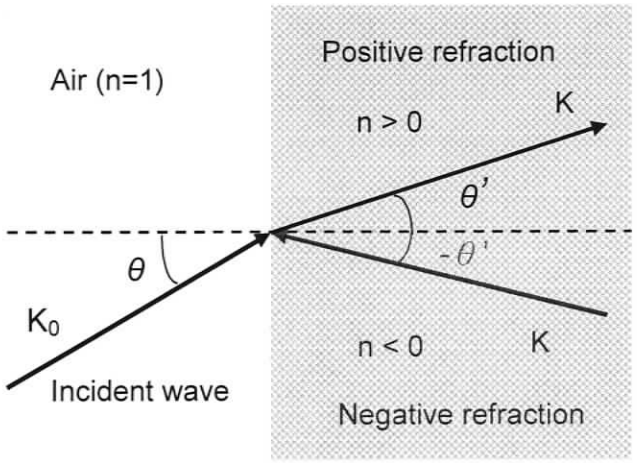

Figure 6.2 Waves are refracted at a negative angle in left-handed metamaterials

6.1.2 Realization and models of metamaterials

Veselago's paper remained without consequence for thirty years simply because no materials with the required properties were known. However, Veselago demonstrated that materials with negative μ and ε had to be frequency-dispersive, implying some intrinsic energy storage capability similar to that found in plasmas. The first realizations of

artificial materials with negative μ and ε emerged in 2000 when Smith et al. [70],[71] created periodic arrays of thin wire strips and split ring resonators and demonstrated experimentally that they had indeed a negative refractive index at the resonant frequency of the constituent elements. However, such composite materials are difficult to manufacture and exhibit a negative refractive index only over a narrow bandwidth due to their resonant nature.

Caloz *et al.* [72], Eleftheriades *et al.* [73],[74] and Oliner [75] independently proposed an alternative way of realizing 2D metamaterials that are non-resonant and have a much wider bandwidth than those based on thin wires and split ring resonators. Their metamaterial models consist of a host transmission line network with embedded lumped series capacitors and shunt inductors. A realization by Iyer and Eleftheriades in the form of a reactively loaded microstrip network is shown in Figure 6.3. A detailed wave analysis and experimental measurements of wave propagation on this two-dimensional periodic structure were reported by Eleftheriades *et al.* [77] in 2002, confirming beyond doubt that it has indeed negative phase velocity and refractive index over a wide frequency range for which the wavelength is large compared to the cell size. It is also obvious that the topology of the structure is identical to that of a 2D TLM shunt network which is periodically loaded with series capacitors and shunt inductors. This inspired So *et al.* to create a TLM model that is, in fact, a computational incarnation of Iyer's and Eleftheriades' microstrip realization. The first successful implementation of this computational 2D-TLM model of metamaterials was reported in 2004 [76].

In 2003, several groups had reported FDTD models of metamaterials [77],[78] that were based on phenomenological Drude models for dispersive negative constitutive parameters. Ziolkowski *et al.* [77] demonstrated the interactions of pulsed and continuous wave (CW) Gaussian beams with double negative (DNG) metamaterials by using such a FDTD model. The focusing effect and the negative angle of refraction behavior are also demonstrated in their paper. Using the FDTD method together with a PML (Perfectly-Matched Layer), Correia *et al.* [78] verified that energy and wave propagation point in opposite directions inside a metamaterial slab, as predicted by Veselago.

In 2005, Hoefer *et al.* [79] and Eleftheriades *et al.* [80] independently proposed a 3D model of metamaterials. Figure 6.4 depicts the unit cells of periodically loaded 1D, 2D and 3D transmission line networks with left-handed wave properties that have been realized so far [64]. The exact location of the reactive elements along the transmission lines can vary for technological reasons, but is not critical, causing only small changes in the electromagnetic properties of the periodic network. Again, the similarity between these unit cells and the corresponding TLM node topologies is obvious.

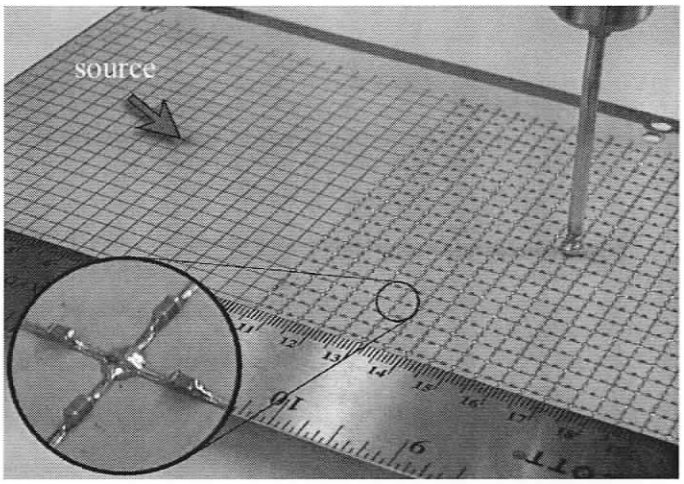

Figure 6.3 Metamaterial model realized by A. K. Iyer and G.V. Eleftheriades at the University of Toronto. It consists of a 2D microstrip mesh loaded periodically with lumped series capacitors and shunt inductors.

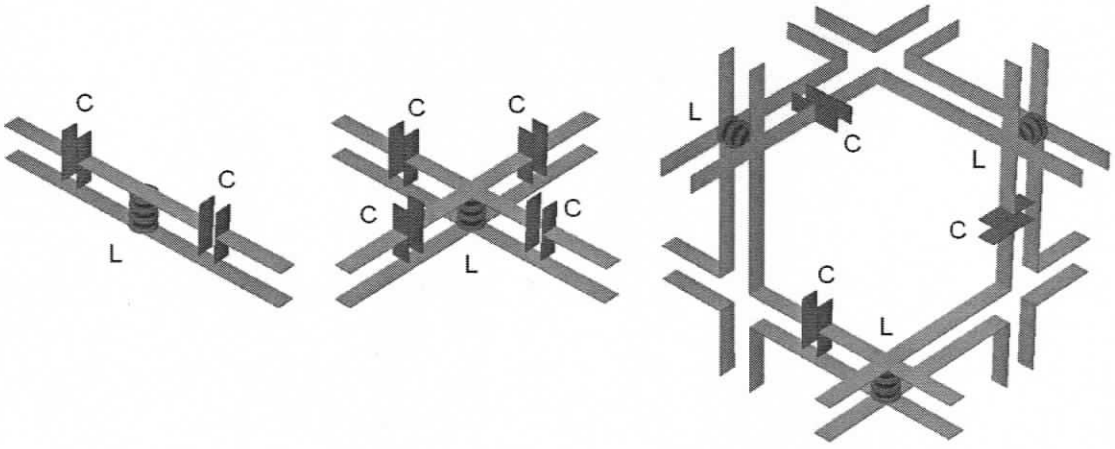

Figure 6.4 Unit cells of 1D (a), 2D (b) and 3D (c) periodically loaded transmission line structures with left-handed wave properties.

6.1.3 TLM models of metamaterials

Traditionally, material properties are introduced in TLM by modifying the scattering procedure at the nodes. This approach requires a new impulse scattering matrix to be derived for the nodes. To implement a metamaterial in 2D-Shunt TLM with air as the hosting medium, a 9×9 impulse scattering matrix is needed [81]. A similar scattering matrix for the 3D-SCN TLM would be of size 27×27; such a huge scattering matrix is not easy to derive.

In this section the inter-cell network approach is employed to introduce the negative permittivity and permeability through interface scattering matrices at the cell boundaries. The implementation preserves the original 12x12 node scattering matrix; and the metamaterial property is realized by a 6x6 interface scattering matrix. In order to handle interface and boundary conditions [82], five types of special inter-cell scattering matrices are needed. These are derived in the following sections for 3D SCN TLM. Since the derivation of the 2D shunt node inter-cell network model of metamaterials is similar to that for the 3D SCN model, it has not been included in this dissertation.

6.2 Determination of the inter-cell network for metamaterials

6.2.1 Inter-cell network modeling of metamaterials

The design of a metamaterial begins with the choice of its intrinsic wave impedance Z_{0m} and its refractive index n_m. Since $Z_{0m} = \sqrt{\mu_m / \varepsilon_m}$ and $n_m = -c\sqrt{\mu_m \varepsilon_m}$, the constitutive parameters of the metamaterial can be expressed as $\mu_m = \frac{n_m Z_{0m}}{c}$ and $\varepsilon_m = \frac{n_m}{Z_{0m} c}$. Substituting μ_m and ε_m into (5.14), both Z_{ssx} and Y_{ppx} (which are negative) can be found. Furthermore, equation (5.16) is employed to obtain the values of the inter-cell network elements in the 3D SCN TLM models with this implementation.

Inter-cell networks are inserted between two SCN nodes along the x-, y-, and z-direction for both polarizations [83]. This involves additional processing of impulses exchanged between neighboring nodes. The inter-cell network inserted between two adjacent cells with identical properties is a single equivalent T element as shown in Figure 6.5; where $C = C_{ssx}$ and $L = L_{ppx}/2$. For a given operating frequency and mesh

parameter $\Delta\ell$ the values of C_{ssx} and L_{ppx} can be calculated using equation (5.16) for 3D SCN nodes.

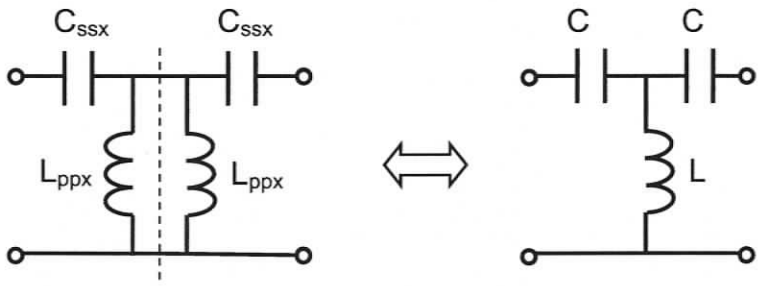

Figure 6.5 Equivalent inter-cell networks for modeling of metamaterials.

The most natural way to implement series capacitances and shunt inductances in TLM is to model them by open- and short-circuited stubs of length $\Delta\ell/2$ and derive an equivalent impulse scattering matrix at the boundary between two cells. This is shown in Figure 6.6 using the same method as described in Section 5.4.

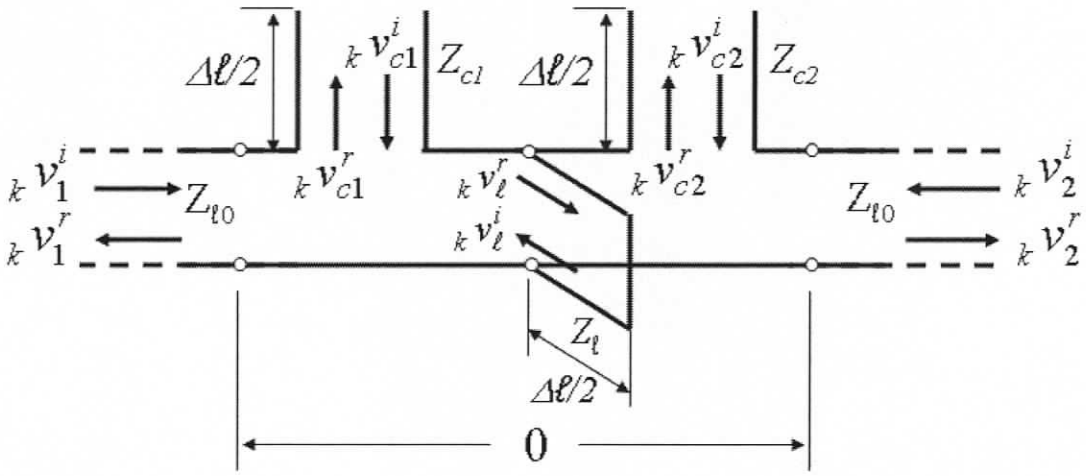

Figure 6.6 The equivalent stub model of the lumped element inter-cell network for modeling negative ε and μ, $Z_{\ell 0}$ is the characteristic impedance of the host like line.

The characteristic impedances of these stubs are related to the series capacitance C and shunt inductance L by the following expressions

$$Z_c = \frac{\Delta\ell}{2Cv_\ell} \qquad Z_\ell = \frac{2Lv_\ell}{\Delta\ell} \tag{6.1}$$

The inter-cell network and its equivalent TLM circuit are shown in Figure 6.7. The scattering matrix is given in equation (6.2).

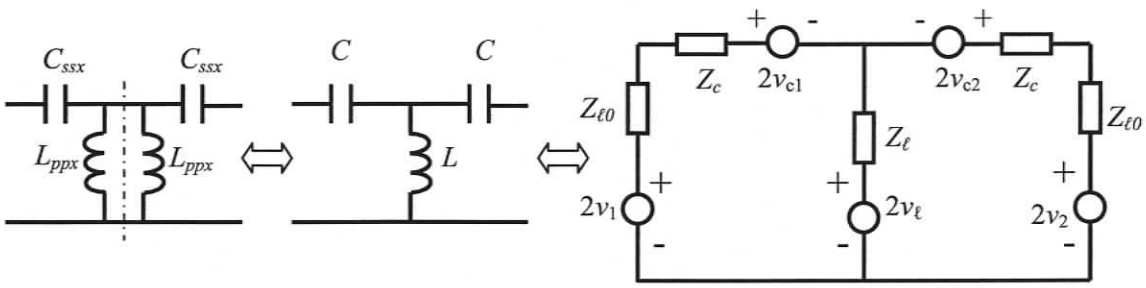

Figure 6.7 Inner inter-cell network for modeling metamaterials, and its equivalent circuit in TLM

$$ {}_k\begin{bmatrix} v_1 \\ v_2 \\ v_{c1} \\ v_{c2} \\ v_\ell \end{bmatrix}^r = \begin{bmatrix} \alpha & \beta & \chi & -\beta & \delta \\ \beta & \alpha & -\beta & \chi & \delta \\ \kappa & -\tau & \vartheta & \tau & -\zeta \\ -\tau & \kappa & \tau & \vartheta & -\zeta \\ \xi & \xi & -\xi & -\xi & \gamma \end{bmatrix} \cdot {}_k\begin{bmatrix} v_1 \\ v_2 \\ v_{c1} \\ v_{c2} \\ v_\ell \end{bmatrix}^i \tag{6.2} $$

where

$$ \alpha = \frac{Z_c + Z_a - Z_{\ell 0}}{Z_c + Z_a + Z_{\ell 0}} \qquad \beta = \frac{2 \cdot Z_a \cdot Z_{\ell 0}}{(Z_c + Z_a + Z_{\ell 0}) \cdot (Z_c + Z_{\ell 0})} \qquad \chi = \frac{2 \cdot Z_{\ell 0}}{Z_c + Z_a + Z_{\ell 0}} $$

$$ \delta = \frac{2 \cdot Z_b \cdot Z_{\ell 0}}{(Z_\ell + Z_b) \cdot (Z_c + Z_{\ell 0})} \qquad \kappa = \frac{2 \cdot Z_c}{Z_c + Z_a + Z_{\ell 0}} \qquad \tau = \frac{2 \cdot Z_a \cdot Z_c}{(Z_c + Z_a + Z_{\ell 0}) \cdot (Z_c + Z_{\ell 0})} $$

$$ \vartheta = \frac{Z_{\ell 0} + Z_a - Z_c}{Z_c + Z_a + Z_{\ell 0}} \qquad \zeta = \frac{2 \cdot Z_b \cdot Z_c}{(Z_\ell + Z_b) \cdot (Z_\ell + Z_{\ell 0})} \qquad \xi = \frac{2 \cdot Z_a}{Z_c + Z_a + Z_{\ell 0}} $$

$$ \gamma = \frac{Z_b - Z_\ell}{Z_b + Z_\ell} \qquad Z_a = \frac{(Z_c + Z_{\ell 0}) \cdot Z_\ell}{Z_c + Z_\ell + Z_{\ell 0}} \qquad Z_b = \frac{Z_c + Z_{\ell 0}}{2} $$

$$ {}_k v_{c1}^i = {}_{k-1} v_{c1}^r \qquad {}_k v_{c2}^i = {}_{k-1} v_{c2}^r \qquad {}_k v_\ell^i = -{}_{k-1} v_\ell^r $$

$$ Z_c = \frac{\Delta \ell}{2 C v_{\ell 0}} \qquad Z_\ell = \frac{2 L v_{\ell 0}}{\Delta \ell} \qquad L = \frac{L_{ppx}}{2} $$

In addition to the above scattering matrix, four more inter-cell network scattering matrices are needed to handle interfaces between the metamaterial and various types of boundaries, namely the electric wall, magnetic wall, regular dielectric material interface, and absorbing boundary. These matrices are derived in the following section.

6.2.2 Inter-cell network for the metamaterial-electric wall interface

The electric boundary inter-cell network and its TLM equivalent circuit are shown in Figure 6.8; the corresponding scattering matrix is given in equation (6.3)

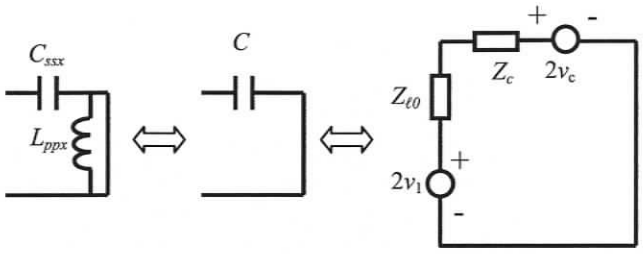

Figure 6.8 Electric boundary inter-cell network and its equivalent circuit in TLM

$$ {}_k\begin{bmatrix} v_1 \\ v_c \end{bmatrix}^r = \begin{bmatrix} e_{11} & e_{12} \\ e_{21} & e_{22} \end{bmatrix} . {}_k\begin{bmatrix} v_1 \\ v_c \end{bmatrix}^i \tag{6.3} $$

where

$$ e_{11} = \frac{Z_c - Z_{\ell 0}}{Z_c + Z_{\ell 0}} = -e_{22} \qquad e_{12} = \frac{2Z_{\ell 0}}{Z_c + Z_{\ell 0}} \qquad e_{21} = \frac{2Z_c}{Z_c + Z_{\ell 0}} $$

$$ Z_c = \frac{\Delta \ell}{2Cv_{\ell 0}} \qquad {}_k v_c^i = {}_{k-1} v_c^r $$

6.2.3 Inter-cell network for the metamaterial - magnetic wall interface

The magnetic boundary inter-cell network and its TLM equivalent circuit are shown in Figure 6.9; the corresponding scattering matrix is given in equation (6.4):

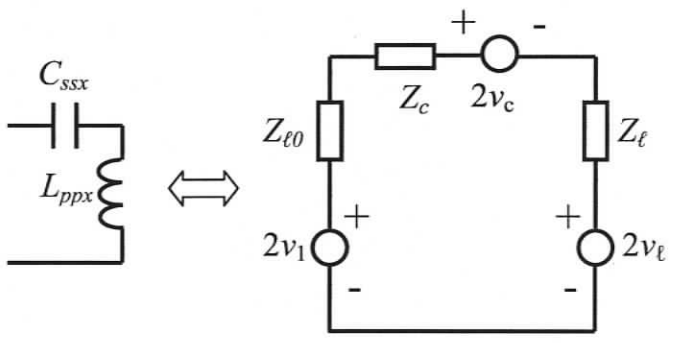

Figure 6.9 Magnetic boundary inter-cell network and its equivalent circuit in TLM

$$\begin{bmatrix} v_1 \\ v_c \\ v_\ell \end{bmatrix}_k^r = \begin{bmatrix} m_{11} & m_{12} & m_{13} \\ m_{21} & m_{22} & m_{23} \\ m_{31} & m_{32} & m_{33} \end{bmatrix} \cdot \begin{bmatrix} v_1 \\ v_c \\ v_\ell \end{bmatrix}_k^i \tag{6.4}$$

where

$$m_{11} = \frac{Z_\ell + Z_c - Z_{\ell 0}}{Z_c + Z_{\ell 0} + Z_\ell} \qquad m_{12} = m_{13} = \frac{2Z_{\ell 0}}{Z_c + Z_{\ell 0} + Z_\ell}$$

$$m_{21} = -m_{23} = \frac{2Z_c}{Z_c + Z_{\ell 0} + Z_\ell} \qquad m_{22} = \frac{Z_\ell + Z_{\ell 0} - Z_c}{Z_c + Z_{\ell 0} + Z_\ell}$$

$$m_{31} = -m_{32} = \frac{2Z_\ell}{Z_c + Z_{\ell 0} + Z_\ell} \qquad m_{33} = \frac{Z_c + Z_{\ell 0} - Z_\ell}{Z_c + Z_{\ell 0} + Z_\ell}$$

$$Z_c = \frac{\Delta\ell}{2C_{ssx}v_{\ell 0}} \qquad Z_\ell = \frac{2L_{ppx}v_{\ell 0}}{\Delta\ell} \qquad {}_k v_\ell^i = -{}_{k-1}v_\ell^r \qquad {}_k v_c^i = {}_{k-1}v_c^r$$

6.2.4 Inter-cell network for the metamaterial - absorbing boundary interface

The absorbing boundary inter-cell network and its TLM equivalent circuit are shown in Figure 6.10; the corresponding scattering matrix is given in equation (6.5).

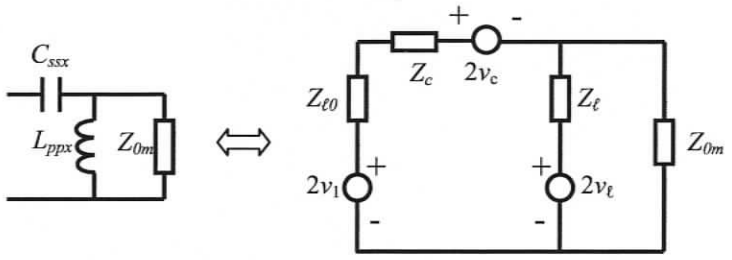

Figure 6.10 Absorbing boundary inter-cell network and its equivalent circuit in TLM, Z_{om} is the matched load impedance at the design frequency.

$$\begin{bmatrix} v_1 \\ v_c \\ v_\ell \end{bmatrix}_k^r = \begin{bmatrix} a_{11} & a_{12} & a_{13} \\ a_{21} & a_{22} & a_{23} \\ a_{31} & a_{32} & a_{33} \end{bmatrix} \cdot \begin{bmatrix} v_1 \\ v_c \\ v_\ell \end{bmatrix}_k^i \tag{6.5}$$

where

$$a_{11}=\frac{Z_z+Z_c-Z_{\ell 0}}{Z_c+Z_{\ell 0}+Z_z} \qquad a_{12}=\frac{2Z_{\ell 0}}{Z_c+Z_{\ell 0}+Z_z} \qquad a_{13}=\frac{(2-Z_\ell\cdot I_a)\cdot Z_{\ell 0}}{Z_c+Z_{\ell 0}}$$

$$a_{21}=\frac{2Z_c}{Z_c+Z_{\ell 0}+Z_z} \qquad a_{22}=\frac{Z_z+Z_{\ell 0}-Z_c}{Z_c+Z_{\ell 0}+Z_z} \qquad a_{23}=\frac{(Z_\ell\cdot I_a-2)\cdot Z_c}{Z_c+Z_{\ell 0}}$$

$$a_{31}=\frac{2Z_z}{Z_c+Z_{\ell 0}+Z_z} \qquad a_{32}=\frac{-2Z_z}{Z_c+Z_{\ell 0}+Z_z} \qquad a_{33}=1-Z_\ell\cdot I_a$$

$$I_a=\frac{2}{(Z_\ell+Z_{0m}(Z_c+Z_{\ell 0}))\cdot(Z_{0m}+Z_c+Z_{\ell 0})} \qquad Z_z=\frac{Z_{0m}\cdot Z_\ell}{Z_\ell+Z_{0m}}$$

$$Z_c=\frac{\Delta\ell}{2C_{ssx}v_{\ell 0}} \qquad Z_\ell=\frac{2L_{ppx}v_{\ell 0}}{\Delta\ell} \qquad {}_k v_\ell^i=-{}_{k-1}v_\ell^r \qquad {}_k v_c^i={}_{k-1}v_c^r$$

6.2.5 Inter-cell network for the metamaterial- air interface

The inter-cell network (for the metamaterial-air interface) and its TLM equivalent circuit are shown in Figure 6.11; the corresponding scattering matrix is given in equation (6.6):

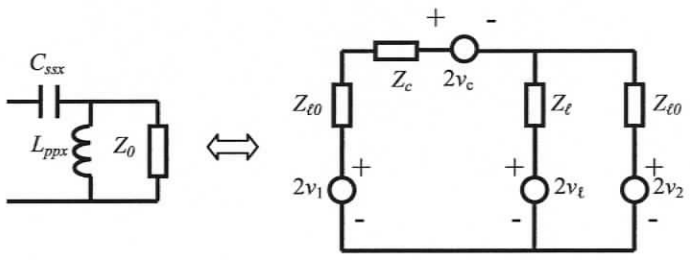

Figure 6.11 Interface inter-cell network (between the metamaterial and the air) and its equivalent circuit in TLM

$$\begin{bmatrix} v_1 \\ v_2 \\ v_c \\ v_\ell \end{bmatrix}^r = \begin{bmatrix} d_{11} & d_{12} & d_{13} & d_{14} \\ d_{21} & d_{22} & d_{23} & d_{24} \\ d_{31} & d_{32} & d_{33} & d_{34} \\ d_{41} & d_{42} & d_{43} & d_{44} \end{bmatrix}_k \cdot \begin{bmatrix} v_1 \\ v_2 \\ v_c \\ v_\ell \end{bmatrix}^i \qquad (6.6)$$

where

$$d_{11}=\frac{Z_\ell Z_c+Z_0Z_c-Z_0^2}{(Z_0+Z_\ell)(Z_0+Z_c)+Z_0Z_\ell} \qquad d_{21}=\frac{2Z_\ell Z_0}{(Z_0+Z_\ell)(Z_0+Z_c)+Z_0Z_\ell}$$

$$d_{31}=\frac{2Z_c(Z_\ell+Z_0)}{(Z_0+Z_\ell)(Z_0+Z_c)+Z_0Z_\ell} \qquad d_{41}=\frac{2Z_\ell Z_0}{(Z_0+Z_\ell)(Z_0+Z_c)+Z_0Z_\ell}$$

$$d_{12}=\frac{2Z_\ell Z_0}{(Z_0+Z_\ell)(Z_0+Z_c)+Z_0Z_\ell} \qquad d_{22}=\frac{Z_\ell Z_c-Z_0Z_c-Z_0^2}{(Z_0+Z_\ell)(Z_0+Z_c)+Z_0Z_\ell}$$

$$d_{32}=\frac{-2Z_\ell Z_c}{(Z_0+Z_\ell)(Z_0+Z_c)+Z_0Z_\ell} \qquad d_{42}=\frac{2Z_\ell(Z_c+Z_0)}{(Z_0+Z_\ell)(Z_0+Z_c)+Z_0Z_\ell}$$

$$d_{13}=\frac{2Z_0(Z_\ell+Z_0)}{(Z_0+Z_\ell)(Z_0+Z_c)+Z_0Z_\ell} \qquad d_{23}=\frac{-2Z_\ell Z_0}{(Z_0+Z_\ell)(Z_0+Z_c)+Z_0Z_\ell}$$

$$d_{33}=\frac{Z_0^2-Z_\ell Z_c-Z_0Z_c+2Z_0Z_\ell}{(Z_0+Z_\ell)(Z_0+Z_c)+Z_0Z_\ell} \qquad d_{43}=\frac{-2Z_\ell Z_0}{(Z_0+Z_\ell)(Z_0+Z_c)+Z_0Z_\ell}$$

$$d_{14}=\frac{2Z_0^2}{(Z_0+Z_\ell)(Z_0+Z_c)+Z_0Z_\ell} \qquad d_{24}=\frac{2Z_0(Z_c+Z_0)}{(Z_0+Z_\ell)(Z_0+Z_c)+Z_0Z_\ell}$$

$$d_{34}=\frac{-2Z_0Z_c}{(Z_0+Z_\ell)(Z_0+Z_c)+Z_0Z_\ell} \qquad d_{44}=\frac{Z_0^2-2Z_\ell Z_0+Z_0Z_c-Z_cZ_\ell}{(Z_0+Z_\ell)(Z_0+Z_c)+Z_0Z_\ell}$$

$$Z_c=\frac{\Delta\ell}{2C_{ssx}v_{\ell 0}} \qquad Z_\ell=\frac{2L_{ppx}v_{\ell 0}}{\Delta\ell} \qquad {}_kv_\ell^i=-{}_{k-1}v_\ell^r \qquad {}_kv_c^i={}_{k-1}v_c^r$$

6.2.6 General inter-cell network between two different materials

To model the interface between two adjacent metamaterials with different properties, a general 6×6 inter-cell network scattering matrix is needed. The general inter-cell network (6×6) and its TLM equivalent circuit are shown in Figure 6.12. The general 6×6 inter-cell network scattering matrix is given in equation (6.7).

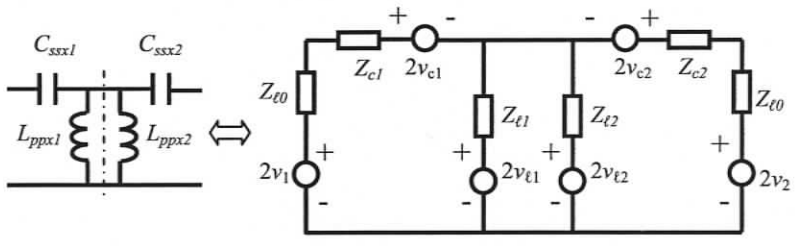

Figure 6.12 General inter-cell network (6×6) and its equivalent circuit in TLM

$$\begin{bmatrix} v_1 \\ v_2 \\ v_{c1} \\ v_{c2} \\ v_{\ell 1} \\ v_{\ell 2} \end{bmatrix}_k^r = \begin{bmatrix} S_{11} & S_{12} & S_{13} & S_{14} & S_{15} & S_{16} \\ S_{21} & S_{22} & S_{23} & S_{24} & S_{25} & S_{26} \\ S_{31} & S_{32} & S_{33} & S_{34} & S_{35} & S_{36} \\ S_{41} & S_{42} & S_{43} & S_{44} & S_{45} & S_{46} \\ S_{51} & S_{52} & S_{53} & S_{54} & S_{55} & S_{56} \\ S_{61} & S_{62} & S_{63} & S_{64} & S_{65} & S_{66} \end{bmatrix} \cdot \begin{bmatrix} v_1 \\ v_2 \\ v_{c1} \\ v_{c2} \\ v_{\ell 1} \\ v_{\ell 2} \end{bmatrix}_k^i \tag{6.7}$$

where

$$Z_a = \frac{(Z_{c2} + Z_{\ell 0}) Z_{\ell 1} Z_{\ell 2}}{(Z_{c2} + Z_{\ell 0})(Z_{\ell 1} + Z_{\ell 2}) + Z_{\ell 1} Z_{\ell 2}} \qquad Z_b = \frac{(Z_{c1} + Z_{\ell 0}) Z_{\ell 1} Z_{\ell 2}}{(Z_{c1} + Z_{\ell 0})(Z_{\ell 1} + Z_{\ell 2}) + Z_{\ell 1} Z_{\ell 2}}$$

$$Z_d = \frac{(Z_{c2} + Z_{\ell 0}) Z_{\ell 2}}{Z_{c2} + Z_{\ell 0} + Z_{\ell 2}} \qquad Z_e = \frac{(Z_{c1} + Z_{\ell 0}) Z_{\ell 1}}{Z_{c1} + Z_{\ell 0} + Z_{\ell 1}}$$

$$S_{11} = \frac{Z_{c1} + Z_a - Z_{\ell 0}}{Z_{c1} + Z_a + Z_{\ell 0}} \qquad S_{21} = \frac{2 Z_a Z_{\ell 0}}{(Z_{c1} + Z_a + Z_{\ell 0})(Z_{c2} + Z_{\ell 0})}$$

$$S_{31} = \frac{2 Z_{c1}}{Z_{c1} + Z_a + Z_{\ell 0}} \qquad S_{41} = \frac{-2 Z_a Z_{c2}}{(Z_{c1} + Z_a + Z_{\ell 0})(Z_{c2} + Z_{\ell 0})}$$

$$S_{51} = S_{61} = \frac{2 Z_a}{Z_{c1} + Z_a + Z_{\ell 0}} \qquad S_{12} = \frac{2 Z_b Z_{\ell 0}}{(Z_{c2} + Z_b + Z_{\ell 0})(Z_{c1} + Z_{\ell 0})}$$

$$S_{22} = \frac{Z_b + Z_{c2} - Z_{\ell 0}}{Z_{c2} + Z_b + Z_{\ell 0}} \qquad S_{32} = \frac{-2 Z_b Z_{c1}}{(Z_{c2} + Z_b + Z_{\ell 0})(Z_{c1} + Z_{\ell 0})}$$

$$S_{42} = \frac{2 Z_{c2}}{Z_{c2} + Z_b + Z_{\ell 0}} \qquad S_{52} = S_{62} = \frac{2 Z_b}{Z_{c2} + Z_b + Z_{\ell 0}}$$

$$S_{13} = \frac{2 Z_{\ell 0}}{Z_{c1} + Z_a + Z_{\ell 0}} \qquad S_{23} = \frac{-2 Z_a Z_{\ell 0}}{(Z_{c1} + Z_a + Z_{\ell 0})(Z_{c2} + Z_{\ell 0})}$$

$$S_{33} = \frac{Z_{\ell 0} + Z_a - Z_{c1}}{Z_{c1} + Z_a + Z_{\ell 0}} \qquad S_{43} = \frac{2 Z_a Z_{c2}}{(Z_{c1} + Z_a + Z_{\ell 0})(Z_{c2} + Z_{\ell 0})}$$

$$S_{53} = S_{63} = \frac{-2 Z_a}{Z_{c1} + Z_a + Z_{\ell 0}} \qquad S_{14} = \frac{-2 Z_b Z_{\ell 0}}{(Z_{c2} + Z_b + Z_{\ell 0})(Z_{c1} + Z_{\ell 0})}$$

$$S_{24} = \frac{2 Z_{\ell 0}}{Z_{c2} + Z_b + Z_{\ell 0}} \qquad S_{34} = \frac{2 Z_b Z_{c1}}{(Z_{c2} + Z_b + Z_{\ell 0})(Z_{c1} + Z_{\ell 0})}$$

$$S_{44} = \frac{Z_{\ell 0} + Z_b - Z_{c2}}{Z_{c2} + Z_b + Z_{\ell 0}} \qquad S_{54} = S_{64} = \frac{-2Z_b}{Z_{c2} + Z_b + Z_{\ell 0}}$$

$$S_{15} = \frac{2Z_d Z_{\ell 0}}{(Z_{c1} + Z_{\ell 0})Z_d + (Z_{c1} + Z_d + Z_{\ell 0})Z_{\ell 1}}$$

$$S_{25} = \frac{2(Z_{c1} + Z_{\ell 0})Z_d Z_{\ell 0}}{[(Z_{c1} + Z_{\ell 0})Z_d + (Z_{c1} + Z_d + Z_{\ell 0})Z_{\ell 1}](Z_{c2} + Z_{\ell 0})}$$

$$S_{35} = \frac{-2Z_d Z_{c1}}{(Z_{c1} + Z_{\ell 0})Z_d + (Z_{c1} + Z_d + Z_{\ell 0})Z_{\ell 1}}$$

$$S_{45} = \frac{-2(Z_{c1} + Z_{\ell 0})Z_d Z_{c2}}{[(Z_{c1} + Z_{\ell 0})Z_d + (Z_{c1} + Z_d + Z_{\ell 0})Z_{\ell 1}](Z_{c2} + Z_{\ell 0})}$$

$$S_{55} = \frac{(Z_{c1} + Z_{\ell 0})Z_d - (Z_{c1} + Z_d + Z_{\ell 0})Z_{\ell 1}}{(Z_{c1} + Z_{\ell 0})Z_d + (Z_{c1} + Z_d + Z_{\ell 0})Z_{\ell 1}}$$

$$S_{65} = \frac{2(Z_{c1} + Z_{\ell 0})Z_d}{(Z_{c1} + Z_{\ell 0})Z_d + (Z_{c1} + Z_d + Z_{\ell 0})Z_{\ell 1}}$$

$$S_{16} = \frac{2(Z_{c2} + Z_{\ell 0})Z_e Z_{\ell 0}}{[(Z_{c2} + Z_{\ell 0})Z_e + (Z_{c2} + Z_e + Z_{\ell 0})Z_{\ell 2}](Z_{c1} + Z_{\ell 0})}$$

$$S_{26} = \frac{2Z_e Z_{\ell 0}}{(Z_{c2} + Z_{\ell 0})Z_e + (Z_{c2} + Z_e + Z_{\ell 0})Z_{\ell 2}}$$

$$S_{36} = \frac{-2(Z_{c2} + Z_{\ell 0})Z_e Z_{c1}}{[(Z_{c2} + Z_{\ell 0})Z_e + (Z_{c2} + Z_e + Z_{\ell 0})Z_{\ell 2}](Z_{c1} + Z_{\ell 0})}$$

$$S_{46} = \frac{-2Z_e Z_{c2}}{(Z_{c2} + Z_{\ell 0})Z_e + (Z_{c2} + Z_e + Z_{\ell 0})Z_{\ell 2}}$$

$$S_{56} = \frac{2(Z_{c2} + Z_{\ell 0})Z_e}{(Z_{c2} + Z_{\ell 0})Z_e + (Z_{c2} + Z_e + Z_{\ell 0})Z_{\ell 2}} \qquad Z_{\ell 1} = \frac{2L_{ppx1} v_{\ell 0}}{\Delta \ell} \qquad Z_{c1} = \frac{\Delta \ell}{2C_{ssx1} v_{\ell 0}}$$

$$S_{66} = \frac{(Z_{c2} + Z_{\ell 0})Z_e - (Z_{c2} + Z_e + Z_{\ell 0})Z_{\ell 2}}{(Z_{c2} + Z_{\ell 0})Z_e + (Z_{c2} + Z_e + Z_{\ell 0})Z_{\ell 2}} \qquad Z_{\ell 2} = \frac{2L_{ppx2} v_{\ell 0}}{\Delta \ell} \qquad Z_{c2} = \frac{\Delta \ell}{2C_{ssx2} v_{\ell 0}}$$

$${}_k v_{\ell 1}^i = -{}_{k-1} v_{\ell 1}^r \qquad {}_k v_{c1}^i = {}_{k-1} v_{c1}^r \qquad {}_k v_{\ell 2}^i = -{}_{k-1} v_{\ell 2}^r \qquad {}_k v_{c2}^i = {}_{k-1} v_{c2}^r$$

6.3 Dispersion analysis

6.3.1 Numerical dispersion analysis for the SCN metamaterial model

A general dispersion equation (5.30) for TLM meshes with inter-cell network has been derived in Chapter 5. Before solving the general dispersion equation, the link network scattering matrix **C** must be derived. Figure 6.13 shows the inter-cell network for the 3D metamaterial model. In TLM, the reactive elements are implemented as open and shorted stubs of length $\Delta\ell/2$ [64].

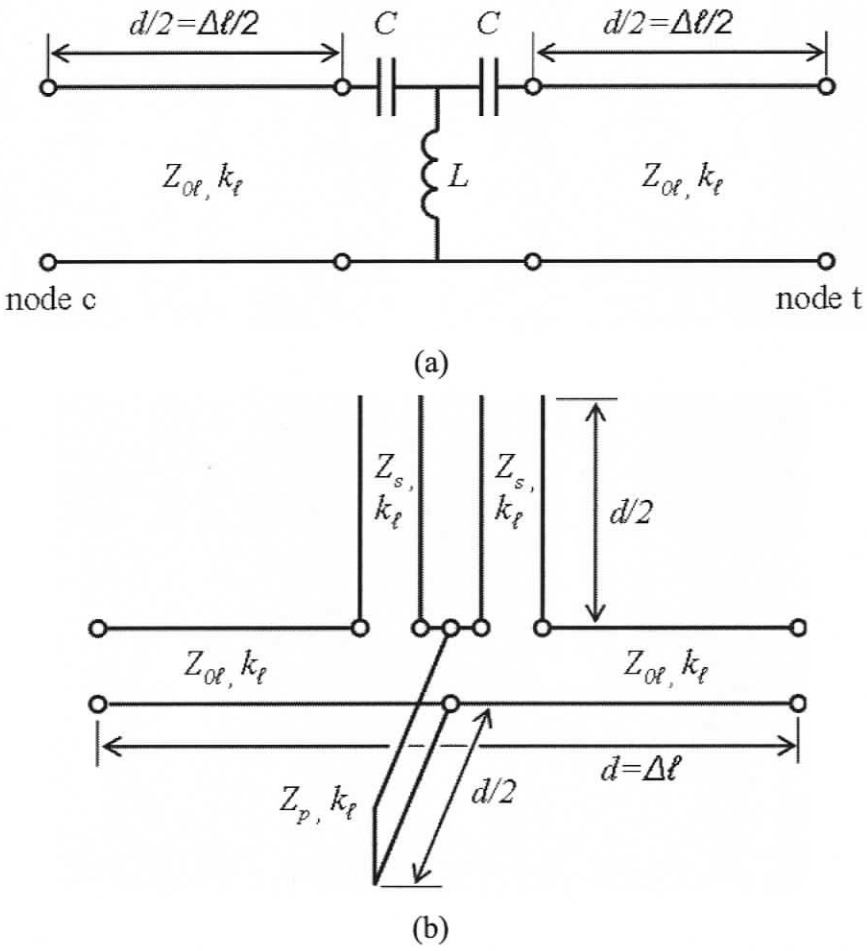

Figure 6.13 Link network inserted between nodes of a 3D mesh to model a negative refractive index material. (a) Lumped element implementation. (b) The TLM link network with reactive stub representation of the lumped elements.

The characteristic impedances Z_s and Z_p of the reactive stubs are related to the lumped elements C and L are as:

$$Z_s = \frac{\Delta\ell}{2Cv_{\ell 0}} \quad \text{and} \quad Z_p = \frac{2Lv_{\ell 0}}{\Delta\ell} \tag{6.8}$$

$$\text{where} \quad C = \frac{-4}{\omega^2(\mu_m - \mu_0)\Delta\ell} \quad \text{and} \quad L = \frac{-2}{\omega^2(\varepsilon_m - \varepsilon_0)\Delta\ell} \tag{6.9}$$

In this case ε_m and μ_m are the negative constitutive parameters of the metamaterial at the design frequency ω. The required scattering matrix **C** of the link network can be obtained by cascading the ABCD matrices of the individual reactive elements and then transforming the overall ABCD matrix into the S-matrix.

Even though the derivation of the link network scattering matrix **C** is straightforward, it is quite difficult to extract a general closed-form singular value expression with the above procedure from the dispersion equation (5.30). In order to assess the dispersion characteristic as functions of the mesh parameter, direction of wave propagation and the type of link network inserted between the nodes, equation (5.30) can be solved numerically using the Matlab matrix solver. Once the P matrix is solved numerically, the propagation constant in the metamaterial at various frequencies can be computed.

This procedure has been used to compute the propagation constant of the SCN metamaterial model shown in Figure 6.13 for $\varepsilon_r = \mu_r = -1$ (refractive index n = –1, intrinsic impedance $\eta_m = \eta_0 = 377\Omega$) at *30 GHz*.

At the design frequency, *30 GHz*, the theoretical phase velocity in this material is equal and opposite in sign to the velocity of light in free space, as long as the cell size of the material is much smaller than the guided wavelength. As the cell size increases, the phase velocity deviates from this asymptotic value due to the discretization error and becomes dependent on the direction of propagation with respect to the mesh axes (directional dispersion).

The usual rule of thumb recommends that the cell size of time- and space-discrete models should not exceed one-tenth of the spatial wavelength. We have thus selected a cell size $\Delta\ell$ = *1 mm*, or $\lambda/10$, at the design frequency of *30 GHz*. At this coarse mesh resolution, the two models in Figure 6.13 would show visible differences in their wave properties.

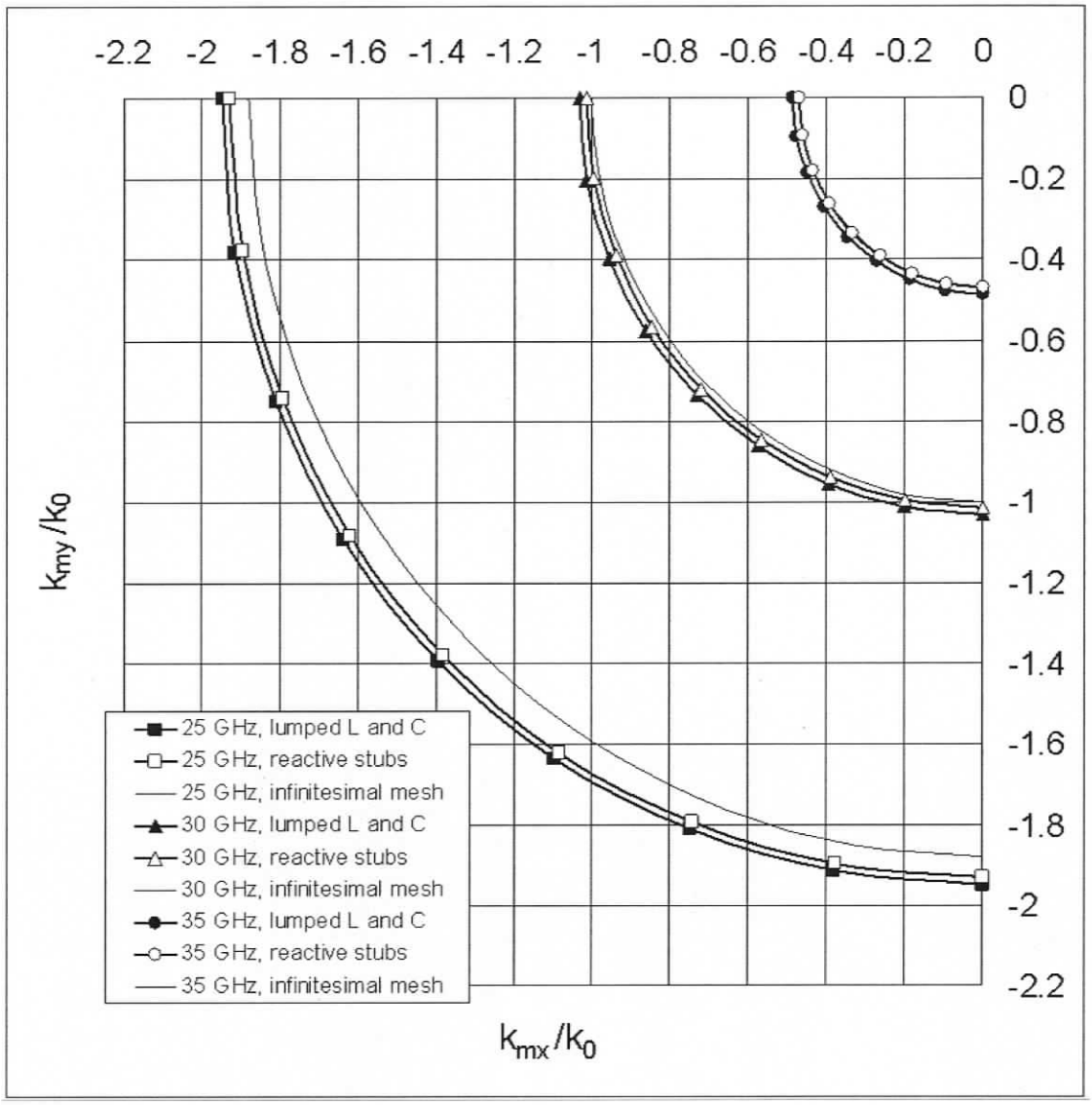

Figure 6.14 Polar plot of the normalized propagation vector $\boldsymbol{k_m/k_0}$ in a transmission line network with periodic reactive loading that models a metamaterial with $\varepsilon_r = \mu_r = -1$ at 30 GHz. The cell size is 1 mm, and propagation is in the xy plane (3D SCN network with lumped element and stub implementations of the inter-cell network).

Figure 6.14 shows the polar plots of the normalized propagation vector $\boldsymbol{k_m/k_0}$ for the 3D symmetrical condensed metamaterial models at 25, 30 and 35 GHz. Propagation in the xy-plane is shown in this case, both models have a *1mm* mesh resolution, and the reactive elements were evaluated at the *30GHz* design frequency. The curves with markers correspond to the lumped element and stub implementations of the node link networks shown in Figure 6.13. The curves without markers in each group represent the asymptotic limit of the propagation vector for infinitesimal cell size and are perfect

circles. Note that, unlike in a regular material, the magnitude of the propagation vector increases as frequency decreases, due to the anomalous dispersion in the metamaterial.

The deviation of the curves from the circular asymptotic limit represents the additional dispersion contributed by the finite discretization. The difference between the marked curves is due to the dispersive nature of the reactive stubs that model the series capacitance and shunt inductance in the link network. These differences are more pronounced at 25 GHz where the guided wavelength is reduced to about *6mm,* or $6\Delta\ell$. Furthermore, one can notice the presence of directional dispersion which causes the curves to deviate from a perfect circle. To better visualize this directional dispersion, a polar plot for 30 GHz on an expanded radial scale is drawn in Figure 6.15. The figure clearly shows that the dispersion error is largest in diagonal direction and smallest along the mesh axes, just like in the corresponding unloaded SCN TLM method.

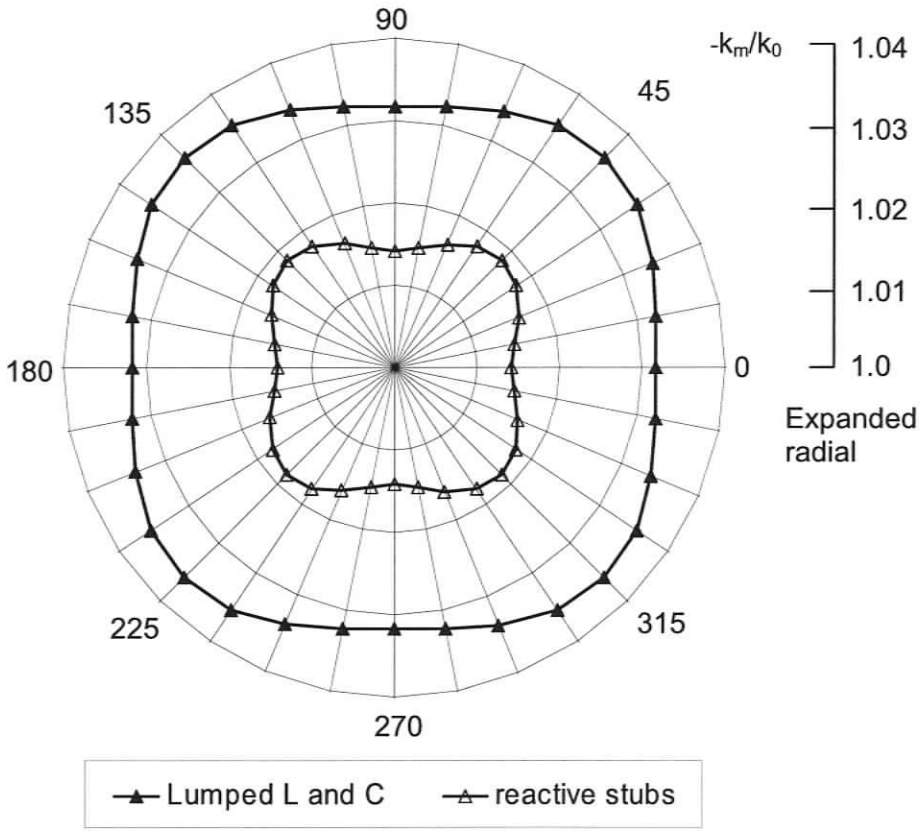

Figure 6.15 Polar plot of the normalized propagation vector $-k_m/k_0$ at 30 GHz on an expanded radial scale that emphasizes the directional dispersion in the metamaterial. (3D SCN TLM network with lumped element and stub implementations of the inter-cell network).

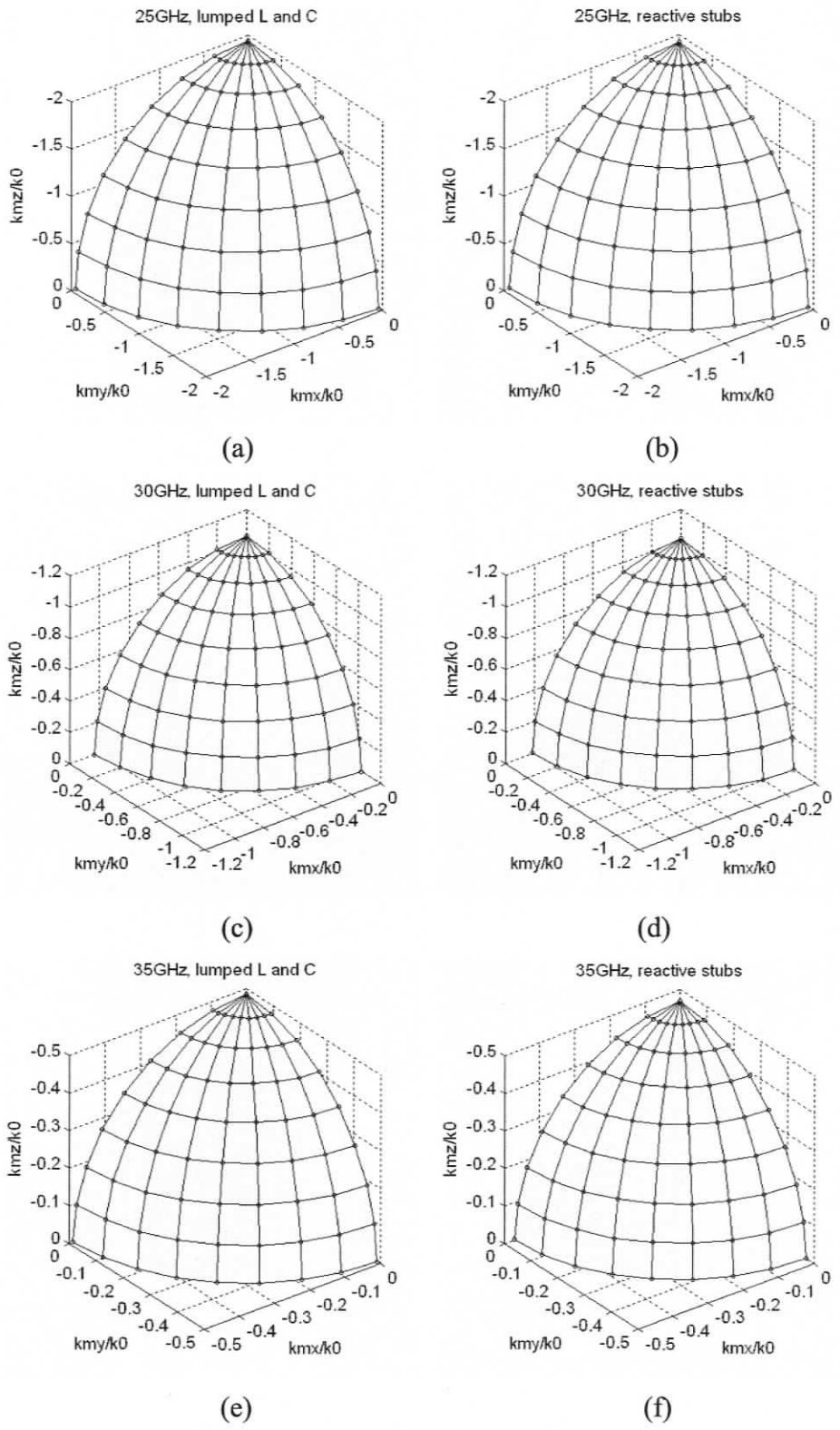

Figure 6.16 Dispersion surfaces of the normalized propagation vector in a 3D symmetrical condensed TLM model of metamaterial at 25, 30 and 35 GHz. $\Delta\ell = 1$ mm. $\varepsilon_r = \mu_r = -1$ at 30 GHz. Lumped element and stub models are compared.

Figure 6.14 and Figure 6.15 also show that the stub implementation gives results that lie roughly half-way between the asymptotic limit $-k_m/k_0 = 1$, and the lumped element implementation results.

Figure 6.16 shows the three-dimensional dispersion surface of the normalized propagation vector for the 3D symmetrical condensed metamaterial model at 25, 30 and 35 GHz. The surfaces are almost spherical at 30 GHz and become slightly deformed as the spatial wavelength in the material gets shorter. The plots in Figure 6.14 represent the intersections of these dispersion surfaces with the principal planes of the 3D mesh.

6.3.2 Closed-form expressions for dispersion along the mesh axes

Since in a general situation, the direction of the propagation vector is not known, it is sufficient to estimate the maximum dispersion error margin by computing the dispersion characteristics in the direction of the mesh axes. In this situation, the periodic structure can be represented by a one-dimensional equivalent circuit, or the axial equivalent circuit, for which a dispersion relation can be found in closed form [64]. The following sections summarize the axial wave properties of the 3D expanded node metamaterial model and compare the result with that of the 3D SCN node implementation.

A. Axial Dispersion Properties of the 3D Distributed Node Model

The axial equivalent circuit of a unit cell of the 3D distributed node model is shown in Figure 6.17. In the figure and following expressions, the index ℓ designates a parameter of the link lines, the index m designates a parameter of the metamaterial (the periodic structure), and the index 0 designates a property of free space.

The voltages and currents at the terminals of the axial equivalent circuit are related by the ABCD matrix of the constituent circuit elements as follows:

$$\begin{bmatrix} V_i \\ I_i \end{bmatrix} = \begin{bmatrix} 1 & 0 \\ Y_{in} & 1 \end{bmatrix} \cdot \begin{bmatrix} \cos\phi & jZ_{0\ell}\sin\phi \\ jY_{0\ell}\sin\phi & \cos\phi \end{bmatrix} \cdot \begin{bmatrix} 1 & \dfrac{1}{2j\omega C} \\ 0 & 1 \end{bmatrix} \cdot \begin{bmatrix} 1 & 2jZ_{0\ell}\tan\phi \\ 0 & 1 \end{bmatrix} \cdot \begin{bmatrix} 1 & \dfrac{1}{2j\omega C} \\ 0 & 1 \end{bmatrix} \cdot \begin{bmatrix} \cos\phi & jZ_{0\ell}\sin\phi \\ jY_{0\ell}\sin\phi & \cos\phi \end{bmatrix} \cdot \begin{bmatrix} 1 & 0 \\ Y_{in} & 1 \end{bmatrix} \cdot \begin{bmatrix} V_{i+1} \\ I_{i+1} \end{bmatrix} \tag{6.10}$$

with $Y_{in} = \frac{1}{Z_{in}} + \frac{1}{2j\omega L}$; $Z_{in} = -jZ_{0\ell}\cot\phi$; $\phi = k_\ell \cdot \Delta\ell/2 = k_0\Delta\ell/4$.

Equation (6.10) is then set equal to a relationship expressed in terms of a Floquet wave in the metamaterial:

$$\begin{bmatrix} V_i \\ I_i \end{bmatrix} = \begin{bmatrix} \cos(k_m\Delta\ell) & jZ_m\sin(k_m\Delta\ell) \\ jY_m\sin(k_n\Delta\ell) & \cos(k_m\Delta\ell) \end{bmatrix} \cdot \begin{bmatrix} V_{i+1} \\ I_{i+1} \end{bmatrix} \tag{6. 11}$$

which leads to the following dispersion relation

$$\cos(k_m\Delta\ell) = 1 - 8\sin^2(\frac{k_\ell\Delta\ell}{2}) - \frac{\cos^2(\frac{k_\ell\Delta\ell}{2}) + \cos(\frac{k_\ell\Delta\ell}{2})}{2\omega^2 \cdot C \cdot L} + \frac{2Z_{0\ell}\sin(\frac{k_\ell\Delta\ell}{2}) \cdot \cos(\frac{k_\ell\Delta\ell}{2})}{\omega \cdot L} + \frac{3\sin(\frac{k_\ell\Delta\ell}{2}) \cdot \cos(\frac{k_\ell\Delta\ell}{2}) + \sin(\frac{k_\ell\Delta\ell}{2})}{\omega \cdot C \cdot Z_{0\ell}} \tag{6.12}$$

which becomes with the approximations $\cos(k_\ell\Delta\ell/2) \approx 1$ and $\sin(k_\ell\Delta\ell/2) \approx (k_\ell\Delta\ell/2)$

$$(k_m\Delta\ell)^2 \approx 4(k_\ell\Delta\ell)^2 + \frac{2}{\omega^2 \cdot C \cdot L} - \frac{2Z_{0\ell}k_\ell\Delta\ell}{\omega \cdot L} - \frac{4k_\ell\Delta\ell}{\omega \cdot C \cdot Z_{0\ell}} \tag{6.13}$$

Equation (6.13) is equivalent to the dispersion relation derived by Grbic and Eleftheriades [80]. C and L in expressions (6.12) and (6.13) are given by (6.9).

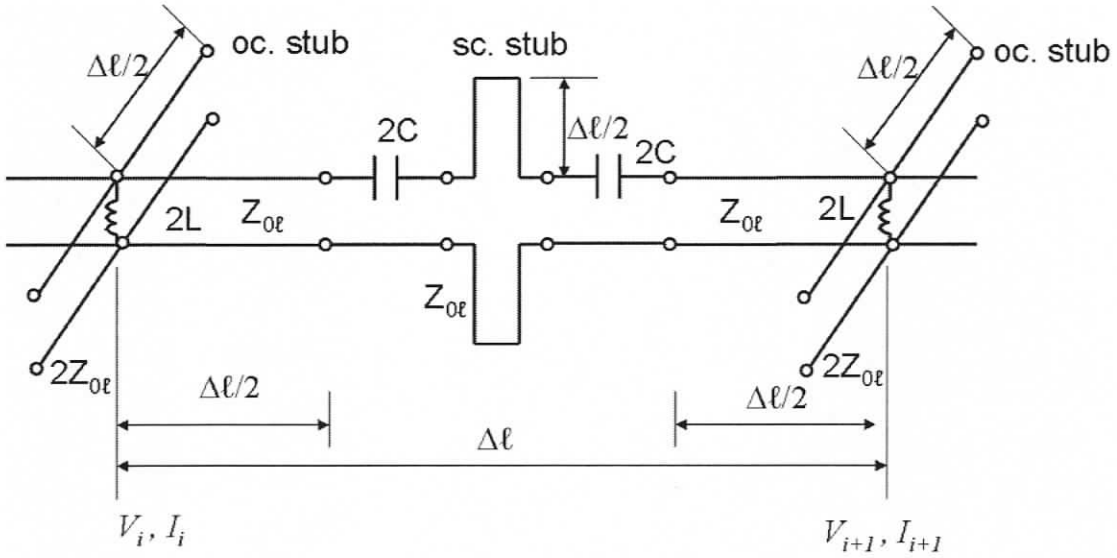

Figure 6.17 Axial equivalent network of the 3D expanded node model of metamaterials. The shunt stub impedances and inductors at the terminals *i* and *i+1* are doubled in value since adjacent cells share these elements.

B. Axial Dispersion Properties of the 3D Symmetrical Condensed Node Model

The axial equivalent circuit of a unit cell of the 3D symmetrical condensed node model with inter-cell network is shown in Figure 6.18.

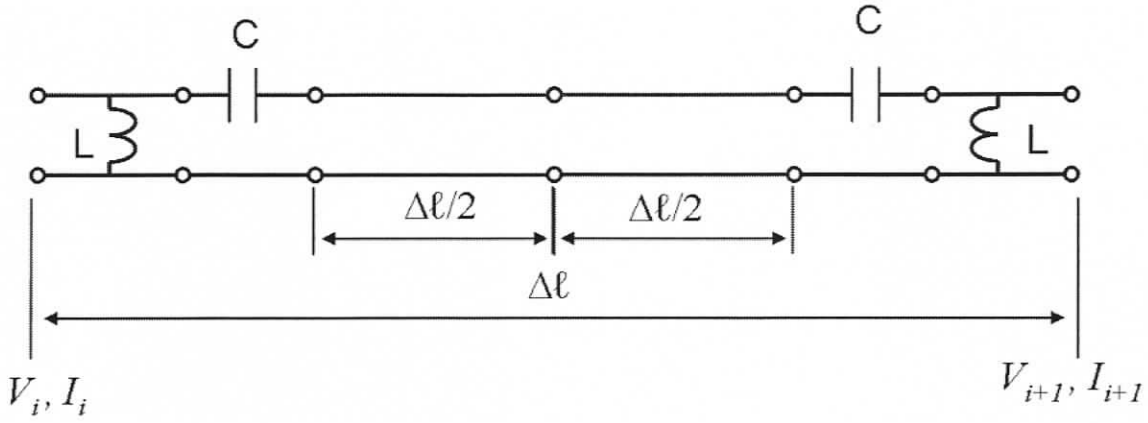

Figure 6.18 Axial equivalent network of the 3D symmetrical condensed node model of metamaterials with negative refractive index. The shunt impedances at the terminals *i* and *i+1* are doubled in value since adjacent cells share these elements.

Using the same index system as in the 3D expanded node cases, we can write the dispersion equation of 3D SCN node in terms of the ABCD parameters of the equivalent circuit as follows:

$$\begin{bmatrix} V_i \\ I_i \end{bmatrix} = \begin{bmatrix} 1 & 0 \\ \dfrac{1}{j\omega L} & 1 \end{bmatrix} \cdot \begin{bmatrix} 1 & \dfrac{1}{j\omega C} \\ 0 & 1 \end{bmatrix} \cdot \begin{bmatrix} \cos\phi & jZ_{0\ell}\sin\phi \\ jY_{0\ell}\sin\phi & \cos\phi \end{bmatrix} \cdot \begin{bmatrix} 1 & \dfrac{1}{j\omega C} \\ 0 & 1 \end{bmatrix} \cdot \begin{bmatrix} 1 & 0 \\ \dfrac{1}{j\omega L} & 1 \end{bmatrix} \cdot \begin{bmatrix} V_{i+1} \\ I_{i+1} \end{bmatrix} \tag{6.14}$$

with $Z_{0\ell} = \eta_0 = \sqrt{\mu_0 / \varepsilon_0}$; $\phi = k_\ell \cdot \Delta\ell = k_0 \Delta\ell / 2$.

Equating (6.14) and (6.11) yields the dispersion equation

$$\cos(k_m \Delta\ell / 2) = \cos(k_m \Delta\ell) - \frac{\cos(k_\ell \Delta\ell)}{2\omega^2 \cdot C \cdot L} + \frac{Z_{0\ell}\sin(k_\ell \Delta\ell)}{4\omega \cdot L} + \frac{\sin(k_\ell \Delta\ell)}{\omega \cdot C \cdot Z_{0\ell}} - \frac{\sin(k_\ell \Delta\ell)}{4\omega^3 \cdot L \cdot C^2 \cdot Z_{0\ell}} \tag{6.15}$$

which can be solved for the propagation constant k_m in the metamaterial:

$$k_m = \frac{2}{\Delta\ell}\cos^{-1}\left[\cos(k_\ell \Delta\ell) - \frac{\cos(k_\ell \Delta\ell)}{2\omega^2 \cdot C \cdot L} + \frac{Z_{0\ell}\sin(k_\ell \Delta\ell)}{4\omega \cdot L} + \frac{\sin(k_\ell \Delta\ell)}{\omega \cdot C \cdot Z_{0\ell}} - \frac{\sin(k_\ell \Delta\ell)}{4\omega^3 \cdot L \cdot C^2 \cdot Z_{0\ell}}\right]. \tag{6.16}$$

C and L in expressions (6.15) and (6.16) are given by (6.9).

6.4 Validation of TLM metamaterial models and their dispersion properties

Numerical models of metamaterials can be validated in three ways.

a) Comparison with experimental measurements,

b) Comparison with other independent numerical methods,

c) Comparison with exact analytical solutions of canonical problems.

Experimental validation ensures that the model captures all the essential and relevant features of a physical metamaterial, i. e. a man-made periodic structure such as the reactively loaded microstrip network by Eleftheriades *et al.* [60]. However, measurements are always affected by error, and it is thus important to know the error margins of both the measurement and the model under test to ensure validation. The same applies to validation by comparison with other numerical methods. As long as the error margins of both the test and reference results overlap, they are most likely to be valid. However, the reference model should be different and independent from the tested model to ensure that both models are not affected by the same common error.

Exact analytical solutions of canonical problems are error-free since they do not involve mathematical or numerical approximations, but they represent ideal situations and exist only for a few specific geometries. Asymptotic solutions obtained by extrapolation of numerical solutions to infinitesimal cell size are also reliable validation references, as demonstrated in Chapter 3 on singularity correction, provided that they have been obtained using explicit iterative methods such as FDTD or TLM. Analytical and asymptotic reference solutions are particularly useful for the validation of dispersion analysis since they represent, by definition, the ideal solution in the absence of dispersion.

Given the strengths and weaknesses of the three validation approaches, it is best practice to employ more than one of them to test new models and algorithms.

6.4.1 Dispersion validation results

Figure 6.19 shows the approximate closed-form expressions for the normalized propagation constant k_m/k_0 in axial direction vs. frequency for the 3D expanded node, and

the 3D symmetrical condensed node models. Superimposed on the figure are three values (black squares) obtained by exact numerical solution of the dispersion equation (5.30).

The constitutive parameters and the cell size are the same as in the previous examples. The two models have slightly different characteristics at 1mm cell size. Exact values are obtained with the numerical solution of equation (5.30) and the closed-form equation for the 3D symmetrical condensed node at 25, 30 and 35 GHz. The closed-form dispersion equation for the 3D expanded node yields slightly higher values than the 3D SCN node. The approximate expressions are thus perfectly adequate for predicting the guided wavelength in the metamaterial as long as $\Delta\ell/\lambda$ is smaller than 0.1.

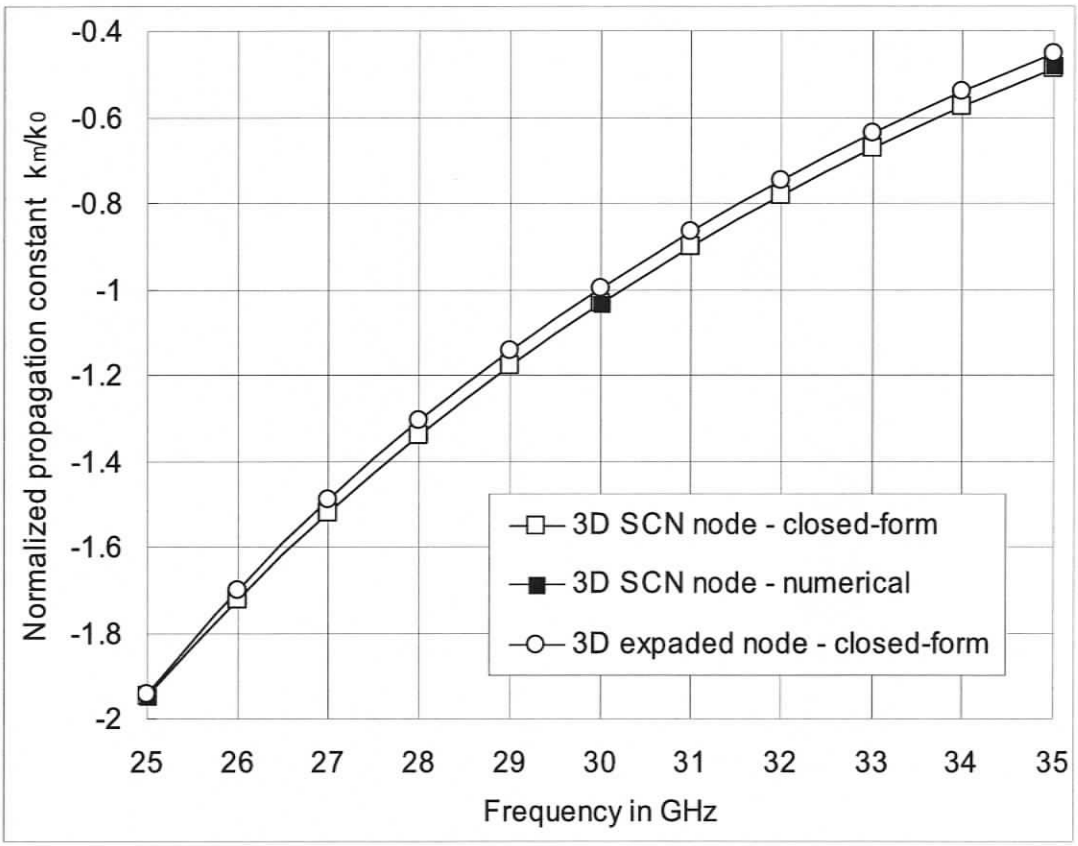

Figure 6.19 Comparison of approximate closed-form dispersion equations for 3D metamaterial models with exact numerical solutions of the dispersion equation (5.30). $\Delta\ell$ = 1 mm. $\varepsilon_r = \mu_r = -1$ at 30 GHz. Models containing lumped L and C elements are compared.

The 3D symmetrical condensed node model has been implemented in MEFiSTo-3D Pro, the TLM field solver of Faustus Scientific Corporation. To validate the general dispersion analysis result, the following numerical experiments were performed to

compute the dispersion of the propagation vector for the same parameters that were used in the analysis. In the MEFiSTo simulation a wideband signal was launched from a point source. Pairs of closely spaced probes were placed along radial directions at 0, 14, 26.57 and 45 degrees with respect to the x-axis in the xy-plane. The phase shift between the probe signals was then computed using the S21 [Degree] feature of MEFiSTo and the normalized propagation vector was obtained from that phase shift. Table 6.1 shows that MEFiSTo data and the results of the dispersion analysis for the 3D symmetrical condensed node model are in good agreements with each other.

3D SCN Node	Propagation angle [deg]	K_m/K_0 Dispersion	K_m/K_0 MEFiSTo	Difference (%)
f=25GHz	0	-1.9308	-1.9312	-0.0246
	14	-1.9357	-1.9363	-0.0298
	26.57	-1.9436	-1.9455	-0.0982
	45	-1.9528	-1.9531	-0.0157
f=30GHz	0	-1.0141	-1.0147	-0.0672
	14	-1.0150	-1.0157	-0.0764
	26.57	-1.0169	-1.0176	-0.0689
	45	-1.0182	-1.0192	-0.0962
f=35GHz	0	-0.4705	-0.4693	0.2.39
	14	-0.4706	-0.4689	-0.366
	26.57	-0.4707	-0.4691	-0.345
	45	-0.4710	-0.4687	0.481

Table 6.1 The normalized propagation constant k_m/k_0 in the 3D symmetrical condensed node model of the metamaterial obtained with the general dispersion equation (5.30) and with MEFiSTo-3D Pro at three frequencies and four propagation angles with respect to the x-axis. The link network has been realized by means of reactive stubs in both cases.

In order to further validate the 3D SCN TLM inter-cell network model of metamaterials, several TE and TM eigenfrequencies of a rectangular waveguide cavity (as shown in Figure 6.20) filled with a fictitious metamaterial of $\varepsilon_r = \mu_r = -1.5$ have been computed analytically. They thus represent canonical validation reference values. From Chapter 5 it is known that the inter-cell metamaterial network is frequency dependent. Therefore C and L of the inter-cell network, shown in Figure 6.5, need to be pre-calculated for each of the expected eigenfrequencies. Table 6.2 gives the required values of the series capacitances and shunt inductances at several theoretical resonant

frequencies for a cubic mesh of 1 mm^3 cell size. The exact theoretical resonant frequencies are then compared in Table 6.3 with those obtained by 3D TLM analysis of the same cavity. Since the direction of propagation is known for each resonant mode of the cavity, the dispersion error of the TLM model of the metamaterial can be verified exactly for the specific angles of propagation with respect to the mesh axes. The comparison shows that the dispersion error is similar to the error affecting the modeling of regular materials with the traditional TLM method.

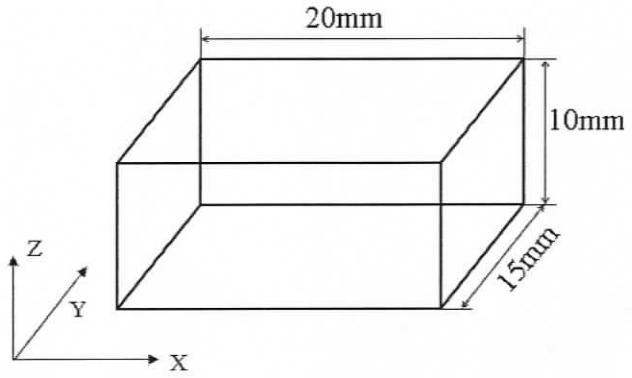

Figure 6.20 The geometry of the test cavity filled with fictitious metamaterial of $\varepsilon_r = \mu_r = -1.5$.

	μ_r	ε_r	f (GHz)	C	L	λ_g(mm)
TE_{101}	-1.5	-1.5	8.3277	4.6506E-13	3.3002E-8	40.00
TE_{102}	-1.5	-1.5	12.0103	2.2358E-13	1.5867E-8	20.00
TM_{111}	-1.5	-1.5	13.0082	1.9060E-13	1.3526E-8	40.00
TM_{112}	-1.5	-1.5	15.6241	1.3212E-13	9.3757E-9	20.00

Table 6.2 The values of the inter-cell network elements required for modeling a metamaterial with $\varepsilon_r = \mu_r = -1.5$ at the first four theoretical resonant frequencies for $\Delta\ell = 1$mm.

Res. Frequency (GHz)	TE_{101}	TE_{102}	TM_{111}	TM_{112}
Theoretical:	8.3277	12.0103	13.0082	15.6241
Computed with TLM:	8.3367	12.0345	13.0310	15.6880
Difference (%)	0.11	0.20	0.18	0.41

Table 6.3 Comparison between theoretical and computed eigenfrequencies of the cavity shown in Figure 6.20 when filled with metamaterial of $\varepsilon_r = \mu_r = -1.5$. $\Delta\ell$=1mm.

6.4.2 Wave transmission through a metamaterial slab

The following numerical experiment is designed to demonstrate the property of negative phase velocity in metamaterials predicted by Veselago. The electric field traveling in x-direction through a parallel plate waveguide filled partially with air and metamaterial is computed. The geometry of the waveguide is shown in Figure 6.21. A 1 mm resolution TLM mesh was used in both the air and metamaterial subsections. At the operating frequency of 10 GHz the refractive index of the metamaterial is $n_m = -2$, and its characteristic impedance is 376.7 Ω.

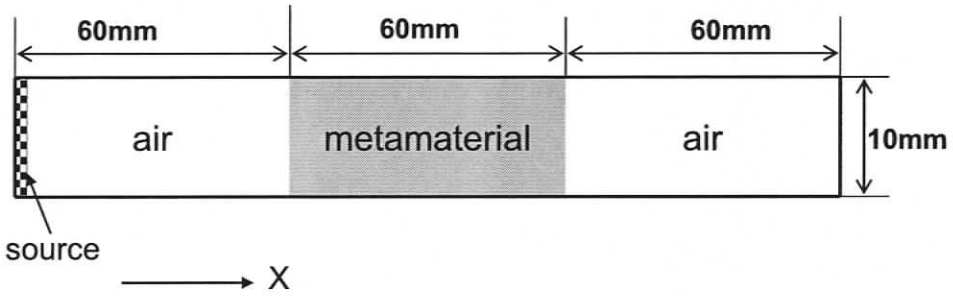

Figure 6.21 Parallel plate waveguide filled with air and metamaterial and excited by a 10GHz sinusoidal signal.

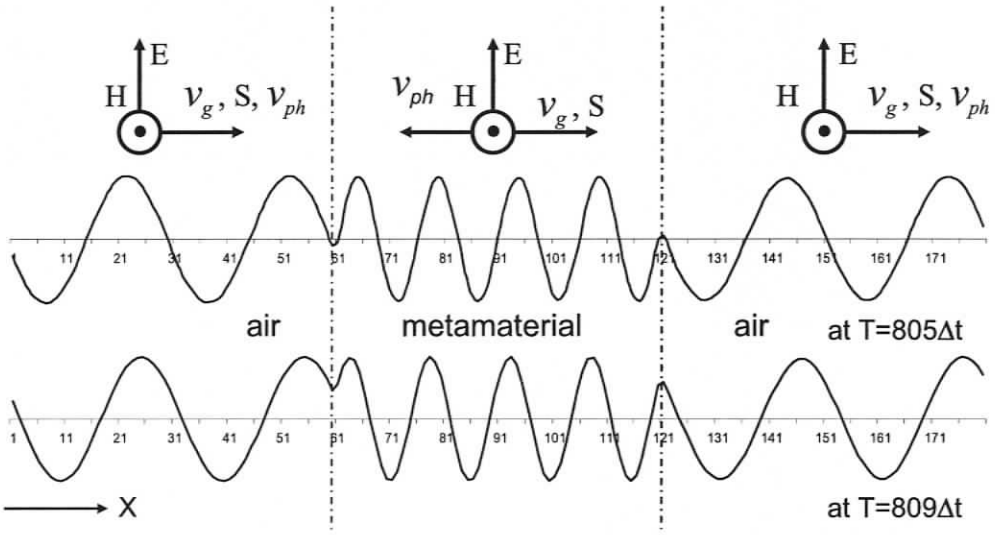

Figure 6.22 Snapshots of the electric field at two time steps for a 10 GHz sinusoidal wave propagating across the air and metamaterial sections

Two snapshots of the electric field propagating through the waveguide are shown in Figure 6.22. Note that the power flows in the positive x-direction while the phase velocity in the metamaterial section is in the negative x-direction. By comparing the relative positions of the zeros and maxima in the two snapshots in Figure 6.22 one notes that

a) the wavelength in the metamaterial is half that in air;

b) the phase velocity is negative and half the velocity in air;

c) all subsections are matched since no scattering occurs at the material interfaces.

These observations confirm that the TLM model of metamaterial exhibits the analytically predicted behavior.

6.4.3 Focusing of a monochromatic wave in metamaterials

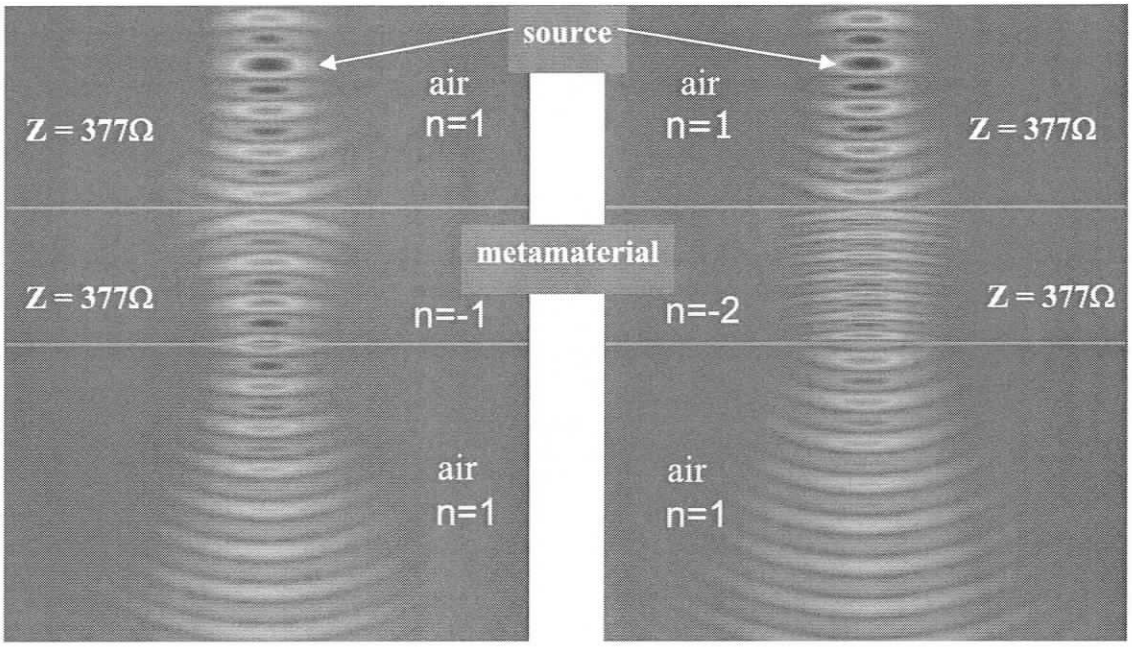

Figure 6.23 Two snapshots of a monochromatic Gaussian beam propagating through air and a metamaterial slab. The beams are normally incident on the interface between air and metamaterial with n= –1 and n= –2, respectively.

One of the essential properties of negative refractive index metamaterials predicted by Veselago [66] is the ability to focus an incident wavefront by means of a planar (non-curved) slab of metamaterial. To verify this property in the TLM metamaterial model, the propagation of a monochromatic Gaussian beam through a metamaterial slab was simulated. The beam was launched from a source in air above the slab. Snapshots of the computed electric field are shown in Figure 6.23 for two values of the negative refractive index of the slab.

The wave impedances of the air and the metamaterial were the same for both n = –1 and n = –2 to ensure an impedance match at the interfaces. In regular materials with positive refractive index, such as air, the beam width becomes wider as it propagates. However, in the metamaterial slab the beam is re-focused and the wave-fronts are curved forward as opposed to the wave-fronts in air. The simulation clearly reveals the focusing effect in the metamaterial slab as well as its negative phase velocity (visible only in an animated display of the simulation results). However, the direction of the flow of energy is still positive because energy is transferred to the other side of the slab. Also note that the wavelength in the slab with refractive index n = –2 is half the wavelength in both the air (n = +1) and the slab with n = –1, as predicted by theory.

6.4.4 Negative refraction in metamaterials

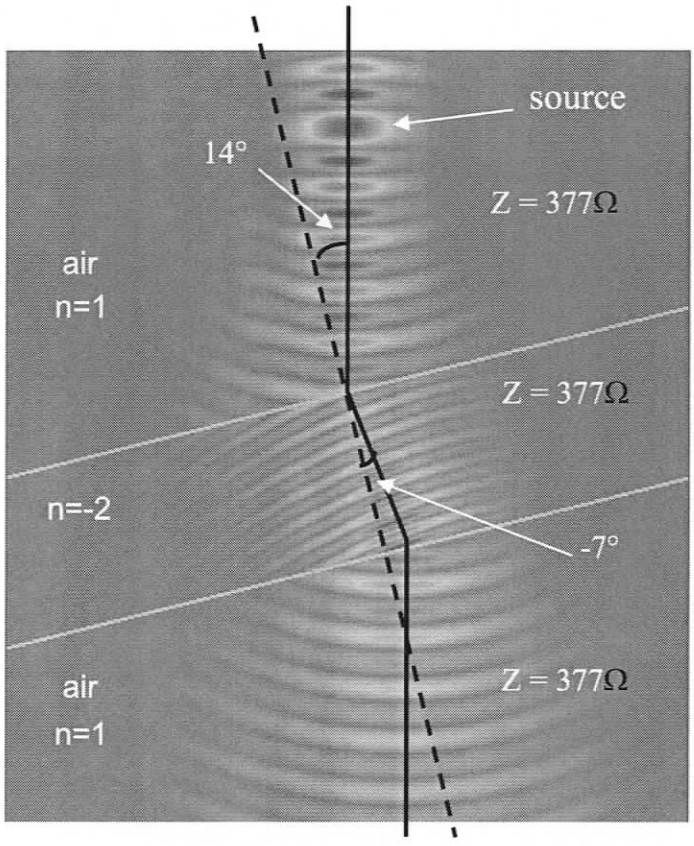

Figure 6.24 Snapshot of a monochromatic Gaussian beam incident at an angle of 14 degrees on a metamaterial slab. The numerical experiment yields a refracted angle of –7 degrees, as predicted by Snell's law. In this example a cell size of 0.125mm is used to discrete the entire computational domain.

In this example the TLM model is validated by computing the negative refracted angle for an oblique incidence of a monochromatic beam, and comparing it with the theoretical angle predicted by Snell's law. Figure 6.24 shows a 100 GHz monochromatic Gaussian beam incident at 14 degrees on the metamaterial slab. Again, the wave impedances of the air and the metamaterial with n = –2 are the same in order to maintain an impedance match at the interfaces between the air and the metamaterial. Snell's law predicts a refracted angle $\theta_2 = \sin^{-1}[(n_1/n_2) \sin \theta_1] = -7$ degrees, which is equal to the simulation result shown in Figure 6.24.

6.4.5 Validation of sub-wavelength focusing

One of the most remarkable properties of a metamaterial slab is its ability to recreate an image with a resolution higher than the wavelength. This property has been predicted by Veselago [66], analytically treated by Pendry [84] (Figure 6.25) in a controversial paper, and confirmed by simulations performed by Grbic and Eleftheriades [85].

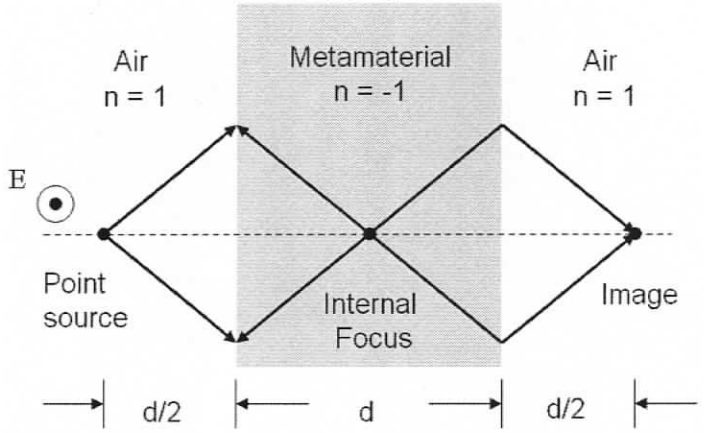

Figure 6.25 Pendry's Perfect Lens consisting of a slab of metamaterial of refractive index –1. The ray diagram predicts perfect focusing due to the negative refraction of the wave incident on the lens. (TE case) (after [84]).

Figure 6.26 shows several phases of the dynamic build-up of the electric field in "Pendry's Perfect Lens" [84] simulated with the 3D SCN TLM Model. The modeling parameters are as follows: Metamaterial Slab: Thickness d = 21 mm, Refractive index $n = -1$, Wave impedance $Z_m = \eta_o$, ($\mu_r = \varepsilon_r = -1$); Air: Refractive index $n = +1$, Wave impedance $Z_{air} = \eta_o$, ($\mu_r = \varepsilon_r = +1$).

The source point is situated at *d/2* from the air-metamaterial interface and emits a monochromatic cylindrical wave of frequency 16.31 GHz.

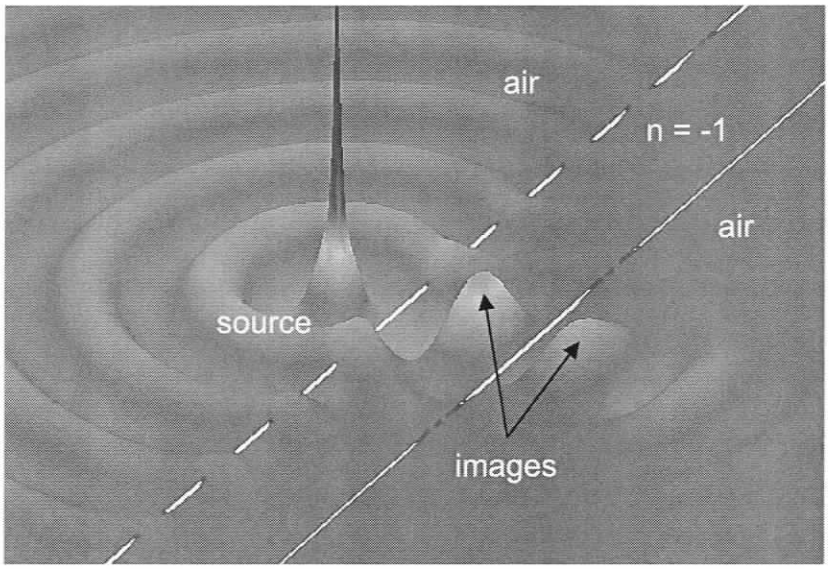

(a) Electric Field at t = 500 ps

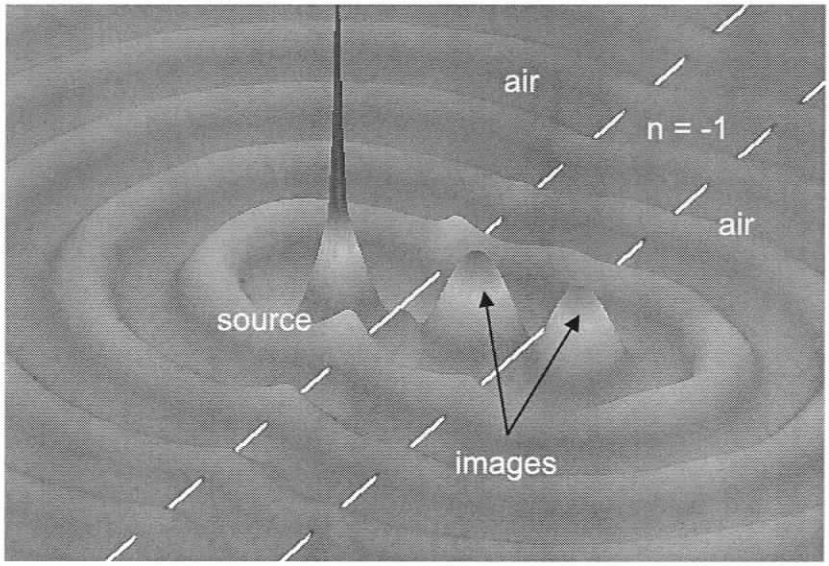

(b) Electric Field at t = 1361 ps

Figure 6.26 Two phases of the dynamic build-up of the electric field in "Pendry's Perfect Lens" (Figure 6.25) simulated with the 3D SCN TLM Model. t = 0 is the time at which the excitation is started at the source. This simulation confirms the results reported in [66], [84] and [85].

The sequence of field plots in Figure 6.26 also shows the progressive build-up of evanescent fields at the air-metamaterial interfaces towards the formation of two images of the source, one situated in the center of the slab (inner focus) and one in the air on the

opposite side of the slab. The transmitted wave pattern is that of a cylindrical wave emanating from the source image on the right side of the lens. These results confirm the predictions by Veselago [66] and Pendry [84] and simulation results published by Grbic and Eleftheriades [85].

6.5 Conclusions

A new model of metamaterials has been developed and implemented. The wave properties of this 3D SCN TLM model of metamaterials with negative refractive index have been analyzed and validated against analytical solutions (cavity resonances, Snell's law of refraction, Pendry's analytical treatment of focusing by a slab) and independent simulations by Eleftheriades *et al.* The general dispersion relation for periodic transmission line networks with embedded lumped elements and reactive stubs has been formulated as a singular value equation and solved numerically using Matlab's symbolic matrix solver. Results obtained with the singular value equation formulation agree well with the corresponding TLM computations. The dispersion analysis result reveals that the SCN structure exhibits strongest dispersion along the diagonal mesh direction; this reflects the behavior of the unloaded TLM networks upon which the metamaterial models are based. Since in most practical simulations the direction of wave propagation is not known, the dispersion error margin can be predicted by evaluating approximate closed-form expressions for axial propagation. Such expressions have been presented and validated in this chapter against full-wave numerical experiments; they are derived using lumped embedded elements and are equivalent to expressions available in the literature.

Chapter 7

Modeling of Gyromagnetic Materials in TLM

In this chapter, the inter-cell network concept described in Chapter 5 is used to model dispersive and non-reciprocal gyromagnetic materials in TLM.

7.1 Introduction

Gyromagnetic materials are widely used in nonreciprocal and control devices such as isolators, circulators, phase shifters, switches, and tunable resonators and filters. The special properties of those devices reside in the tensor magnetic constitutive parameters of gyromagnetic materials; the constitutive parameters can be changed by external DC magnetic bias fields. However, the analytical study of electromagnetic wave interaction with gyromagnetic materials is a challenging task. Therefore, numerical techniques such as TLM and FDTD are often used to model the material.

Two groups of approaches have been reported in FDTD. In the first group, Maxwell's equations are coupled with Gilbert's equation of motion to describe the gyromagnetic material properties in the time domain [86], [87],[88]. In the second group, the ferrites are characterized in the frequency domain by the Polder tensor [89],[90]. Some work on modeling of gyromagnetic materials with the TLM method has also been reported [91], [92], [93]. Yaich and Khalladi [91] use the time domain susceptibility functions $x(t)$ and $k(t)$, which are obtained by inverse Fourier transform of the permeability tensor $[\mu(\omega)]$, to describe the anisotropic and dispersive properties of gyromagnetic material. In that approach three supplementary stubs are added to the standard (18x18) SCN node. Current sources describing the gyromagnetic properties are introduced in these extra stubs. De Menezes and Hoefer [92] here reported a state-variable technique to model gyromagnetic

materials. Those two methods change the scattering process at the node. In this chapter, a new approach is introduced in which the scattering procedure at the TLM nodes remains unchanged, but an inter-cell network is inserted between neighboring nodes to model the properties of gyromagnetic material.

7.2 Theory of the proposed model

Gyromagnetic material has a permeability tensor which can be expressed in the frequency domain as follows [94].

$$\mu = \mu_0 \cdot \begin{bmatrix} \mu_1 & j\kappa & 0 \\ -j\kappa & \mu_1 & 0 \\ 0 & 0 & 1 \end{bmatrix} \tag{7.1}$$

where

$$\mu_1 = 1 + \frac{\omega_0 \omega_m}{\omega_0^2 - \omega^2}; \quad \kappa = \frac{\omega \omega_m}{\omega_0^2 - \omega^2}; \quad \omega_0 = H_i \gamma; \text{ and } \omega_m = M_s \gamma. \tag{7.2}$$

γ is the gyromagnetic ratio, M_s and H_i denote saturation magnetization and static biasing magnetic field polarized in the z-direction.

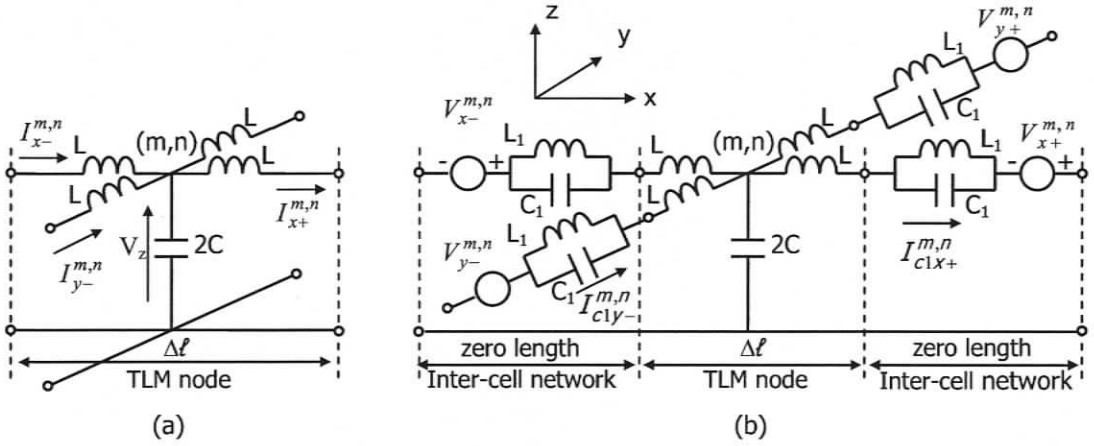

Figure 7.1 TLM 2D shunt node (a) in the case of simple dielectric (b) in the case of modeling gyromagnetic material properties by using inter-cell networks. Here m and n denote the location of a cell along the x- and y-directions.

Gwarek and Moryc [89] have reported a 2D lumped equivalent circuit approach to model magnetized ferrite; the equivalent circuit in their model is very similar to the 2D TLM shunt node. With the availability of the inter-cell network developed in Chapter 5, their idea can be implemented in TLM [95].

Figure 7.1 depicts a unit cell of a 2D TLM shunt network. The gyromagnetic material properties are introduced by the LC resonator and voltage source controlled by current flowing through the capacitor of the perpendicular arms. The values of the capacitor C and the inductor L obtained using TLM theory are given in (7.3).

$$L = \mu_0 \cdot \frac{1}{2}\Delta\ell\,, \qquad 2C = \varepsilon \cdot \Delta\ell \tag{7.3}$$

L_1 and C_1 as well as the relationship between the voltage sources and the currents flowing through the capacitance for a lossless case are derived as follows. The wave equations of a two-dimensional wave with three field components E_z, H_x, and H_y propagating between two electric planes at z = 0 and $z = \Delta\ell$ can be transformed into circuit equations as shown in (7.4).

$$-\frac{\partial E_z}{\partial x} = -\mu_0 \frac{\partial H_y}{\partial t} = -j\omega\mu_0 H_y \Rightarrow -j\omega L(I_{x-}^{m,n} + I_{x+}^{m,n}) = V^{m+1,n} - V^{m,n} \tag{7.4a}$$

$$\frac{\partial E_z}{\partial y} = -\mu_0 \frac{\partial H_x}{\partial t} = -j\omega\mu_0 H_x \Rightarrow -j\omega L(I_{y-}^{m,n} + I_{y+}^{m,n}) = V^{m,n+1} - V^{m,n} \tag{7.4b}$$

$$\frac{\partial H_y}{\partial x} - \frac{\partial H_x}{\partial y} = -j\omega\varepsilon E_z \Rightarrow$$

$$-2j\omega C V^{m,n} = I_{x+}^{m+1,n} + I_{x-}^{m+1,n} - I_{x+}^{m,n} - I_{x-}^{m,n} + I_{y+}^{m+1,n} + I_{y-}^{m+1,n} - I_{y+}^{m,n} - I_{y-}^{m,n} \tag{7.4c}$$

where

$$V^{m,n} = \Delta\ell \cdot E_z \qquad (x = m\,\Delta\ell,\ y = n\,\Delta\ell)$$

$$\frac{1}{2}(I_{x+}^{m,n} + I_{x-}^{m,n}) = I_x^{m,n} = \Delta\ell \cdot H_y \quad (x = m\,\Delta\ell,\ y = n\,\Delta\ell)$$

$$\frac{1}{2}(I_{y+}^{m,n} + I_{y-}^{m,n}) = I_y^{m,n} = -\Delta\ell \cdot H_x \quad (x = m\,\Delta\ell,\ y = n\,\Delta\ell)$$

Substituting equations (7.1) and (7.2) into Maxwell's equations for the 2D TM case ($E_x = 0$, $E_y = 0$ and $H_z = 0$) gives

$$-\frac{\partial E_z}{\partial x} = -j\omega\mu_0(\mu_1 H_y - j\kappa H_x) \Rightarrow$$

$$-j\omega L[(1+\beta)(I_{x-}^{m,n} + I_{x+}^{m,n}) + j\frac{\omega}{4\cdot\omega_0}\beta(I_{y+}^{m,n} + I_{y-}^{m,n} + I_{y+}^{m+1,n} + I_{y-}^{m+1,n})] = V^{m+1,n} - V^{m,n} \tag{7.5a}$$

$$\frac{\partial E_z}{\partial y} = -j\omega\mu_0(\mu_1 H_x + j\kappa H_y) \Rightarrow$$

$$-j\omega L[(1+\beta)(I_{y-}^{m,n} + I_{y+}^{m,n}) - j\frac{\omega}{4\cdot\omega_0}\beta(I_{x+}^{m,n} + I_{x-}^{m,n} + I_{x+}^{m,n+1} + I_{x-}^{m,n+1})] = V^{m,n+1} - V^{m,n} \qquad (7.5b)$$

where $\beta = \frac{\omega_0\omega_m}{\omega_0^2 - \omega^2}$ corresponds to a parallel LC circuit resonating at $\omega_0^2 = 1/(L_1 \cdot C_1)$ with $L_1 / L = \omega_m / \omega_0$, $I_y^{m+0.5,n} = \frac{1}{2}(I_y^{m,n} + I_y^{m+1,n})$ and $I_x^{m,n+0.5} = \frac{1}{2}(I_x^{m,n} + I_x^{m,n+1})$ since we can not obtain $I_y^{m+0.5,n}$ and $I_x^{m,n+0.5}$ directly. Equation (7.4c) remains valid because the magnetization is along the z-axis. The second term of (7.5a) can be written as in (7.6a) because the voltage across the LC resonator as well as the voltage across the capacitor C_1 ($V_{c1}^{m,n}$) is proportional to that current flowing through the whole resonator multiplied by $j\omega$, The current flowing through the capacitor C_1 ($V_{c1}^{m,n}$) is proportional to the voltage multiplied by $j\omega$.

$$\begin{aligned} V_x^{m+0.5,n} &= V_{x+}^{m,n} + V_{x-}^{m+1,n} \\ &= \frac{-j^2\omega^2 L\beta(I_{y-}^{m,n} + I_{y+}^{m,n} + I_{y-}^{m+1,n} + I_{y+}^{m+1,n})}{4\cdot\omega_0} = \frac{j\omega}{2\cdot 2\cdot\omega_0}\cdot(-j\omega)L\beta(I_{y-}^{m,n} + I_{y+}^{m,n} + I_{y-}^{m+1,n} + I_{y+}^{m+1,n}) \\ &= -\frac{-j\omega}{2\cdot\omega_0}(V_{c1y-}^{m,n} + V_{c1y+}^{m,n} + V_{c1y-}^{m+1,n} + V_{c1y+}^{m+1,n}) = \frac{-1}{2\cdot\omega_0\cdot C1}(I_{c1y-}^{m,n} + I_{c1y+}^{m,n} + I_{c1y-}^{m+1,n} + I_{c1y+}^{m+1,n}) \end{aligned} \qquad (7.6a)$$

$$\begin{aligned} V_y^{m,n+0.5} &= V_{y+}^{m,n} + V_{y-}^{m,n+1} \\ &= \frac{j^2\omega^2 L\beta(I_{x-}^{m,n} + I_{x+}^{m,n} + I_{x-}^{m,n+1} + I_{x+}^{m,n+1})}{4\cdot\omega_0} = \frac{-j\omega}{2\cdot 2\cdot\omega_0}\cdot(-j\omega)L\beta(I_{x-}^{m,n} + I_{x+}^{m,n} + I_{x-}^{m,n+1} + I_{x+}^{m,n+1}) \\ &= -\frac{-j\omega}{2\cdot\omega_0}(V_{c1x-}^{m,n} + V_{c1y+}^{m,n} + V_{c1x-}^{m,n+1} + V_{c1y+}^{m,n+1}) = \frac{1}{2\cdot\omega_0\cdot C1}(I_{c1x-}^{m,n} + I_{c1x+}^{m,n} + I_{c1x-}^{m,n+1} + I_{c1x+}^{m,n+1}) \end{aligned} \qquad (7.6b)$$

In the above formula, m and n denote the node location along the x- and y-directions. Note that the inter-cell networks are frequency independent, but the voltage sources involve a simultaneous coupling between x- and y-directions at each time step.

7.3 Implementation

For ease of implementation and efficiency of execution, the current-controlled voltage sources in adjacent unit cells are combined to form a single voltage source.

Figure 7.2 depicts the source together with its corresponding LC resonators; the three components in series form the inter-cell network that describes the material properties.

The voltage amplitude of the source in the inter-cell network is just a series combination of the two adjacent ones:

$$V_x^{m+0.5,n}{}_x = V_{x+}^{m,n} + V_{x-}^{m+1,n} \tag{7.7}$$

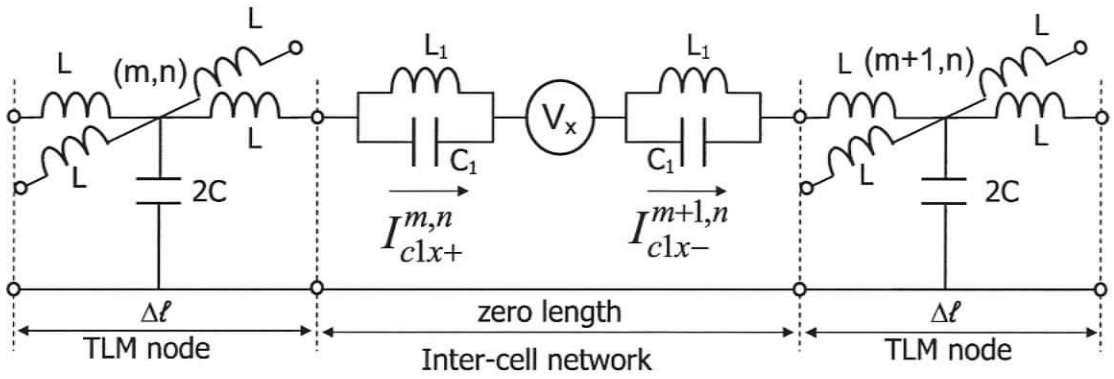

Figure 7.2 The inter-cell network describing the properties of gyromagnetic materials is located at the cell boundary between two standard 2D TLM shunt nodes and is the same in x- and y-direction.

Therefore, in order to update the voltage sources in the inter-cell network, $V_{k,x}$ and $V_{k,y}$ are updated using the following sequence of operations:

1) At t = $k\Delta t$, all $I_{k,c1y-}^{m,n}$ and $I_{k,c1y+}^{m,n}$ are updated based on $I_{k-2,c1y-}^{m,n}$, $I_{k-1,c1y-}^{m,n}$, $I_{k-2,c1y+}^{m,n}$ and $I_{k-1,c1y+}^{m,n}$ using central difference approximation. Then $V_{k,x}^{m+0.5,n}$ is updated using (7.6a) based on $I_{k,c1y-}^{m,n}$ and $I_{k,c1y+}^{m,n}$.

2) All $I_{k,c1x-}^{m,n}$ and $I_{k,c1x+}^{m,n}$ are updated based on $V_{k,x}^{m,n}$ and the reflected impulse voltages at the corresponding branches of the nodes.

3) All $V_{k,y}^{m,n+0.5}$ are updated using (7.6b) based on $I_{k,c1x-}^{m,n}$ and $I_{k,c1x+}^{m,n}$.

5) All $I_{k,c1y-}^{m,n}$ and $I_{k,c1y+}^{m,n}$ are updated based on $V_{k,y}^{m,n}$ and the reflected impulse voltages at the corresponding branches of the nodes.

6) Repeat 1) to 5) at the next time step t = $(k+1)\Delta t$.

The inter-cell network for the gyromagnetic material and its TLM equivalent circuit are shown in Figure 6.7. The scattering matrix given in equation (7.8) is for the x-direction; where $Z_{\ell 0}$ denotes the characteristic impedance of the host TLM link lines. The scattering matrix for the y-direction can be derived in a similar manner.

$$\begin{bmatrix} v_1 \\ v_2 \\ v_{\ell 1} \\ v_{\ell 2} \\ v_{c1} \\ v_{c2} \end{bmatrix}_k^r = \begin{bmatrix} S_{11} & S_{12} & S_{13} & S_{14} & S_{15} & S_{16} & S_{17} \\ S_{21} & S_{22} & S_{23} & S_{24} & S_{25} & S_{26} & S_{27} \\ S_{31} & S_{32} & S_{33} & S_{34} & S_{35} & S_{36} & S_{37} \\ S_{41} & S_{42} & S_{43} & S_{44} & S_{45} & S_{46} & S_{47} \\ S_{51} & S_{52} & S_{53} & S_{54} & S_{55} & S_{56} & S_{57} \\ S_{61} & S_{62} & S_{63} & S_{64} & S_{65} & S_{66} & S_{67} \end{bmatrix} \cdot \begin{bmatrix} v_1 \\ v_2 \\ v_{\ell 1} \\ v_{\ell 2} \\ v_{c1} \\ v_{c2} \\ v_x \end{bmatrix}_k^i \tag{7.8}$$

where

$$Z_a = \frac{Z_c Z_\ell}{(Z_c + Z_\ell)} \qquad \text{bb} = 2Z_c Z_{\ell 0} + Z_c Z_a + 2Z_\ell Z_{\ell 0} + Z_\ell Z_a + Z_\ell Z_c$$

$$S_{11} = S_{31} = -S_{41} = S_{51} = -S_{61} = \frac{Z_a}{Z_a + Z_{\ell 0}} \qquad S_{21} = \frac{Z_{\ell 0}}{Z_a + Z_{\ell 0}}$$

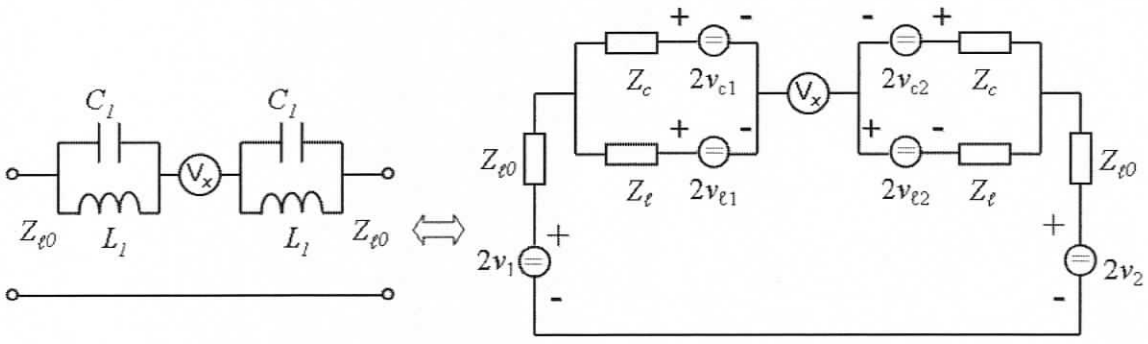

Figure 7.3 Inner inter-cell network for gyromagnetic materials and its equivalent circuit in TLM.

$$S_{22} = -S_{32} = S_{42} = -S_{52} = S_{62} = \frac{Z_a}{Z_a + Z_{\ell 0}} \qquad S_{12} = \frac{Z_{\ell 0}}{Z_a + Z_{\ell 0}}$$

$$S_{33} = \frac{2Z_c Z_{\ell 0} + Z_c Z_a - 2Z_\ell Z_{\ell 0} - Z_\ell Z_a - Z_c Z_\ell}{bb} \qquad S_{13} = -S_{23} = \frac{2Z_{\ell 0} Z_c}{bb}$$

$$S_{43} = S_{63} = \frac{2Z_a Z_c}{bb} \qquad S_{53} = \frac{2Z_c(2Z_{\ell 0} + Z_a)}{bb}$$

$$S_{14} = -S_{24} = \frac{-2Z_{\ell 0} Z_c}{bb} \qquad S_{34} = S_{54} = \frac{2Z_a Z_c}{bb}$$

$$S_{44} = \frac{2Z_c Z_{\ell 0} + Z_c Z_a - 2Z_\ell Z_{\ell 0} - Z_\ell Z_a - Z_c Z_\ell}{bb} \qquad S_{64} = \frac{2Z_c(2Z_{\ell 0} + Z_a)}{bb}$$

$$S_{15} = -S_{25} = \frac{2Z_{\ell 0} Z_\ell}{bb} \qquad S_{35} = \frac{2Z_\ell(2Z_{\ell 0} + Z_a)}{bb}$$

$$S_{55} = \frac{-2Z_c Z_{\ell 0} - Z_c Z_a + 2Z_\ell Z_{\ell 0} + Z_\ell Z_a - Z_c Z_\ell}{bb} \qquad S_{45} = S_{65} = \frac{2Z_a Z_\ell}{bb}$$

$$S_{16} = -S_{26} = \frac{-2Z_{\ell 0} Z_\ell}{bb} \qquad S_{36} = \frac{2Z_a Z_\ell}{bb} = S_{56}$$

$$S_{66} = \frac{-2Z_c Z_{\ell 0} - Z_c Z_a + 2Z_\ell Z_{\ell 0} + Z_\ell Z_a - Z_c Z_\ell}{bb} \qquad S_{46} = \frac{2Z_\ell(2Z_{\ell 0} + Z_a)}{bb}$$

$$S_{37} = -S_{47} = S_{57} = -S_{67} = \frac{Z_a}{2(Z_a + Z_{\ell 0})} \qquad S_{17} = -S_{27} = \frac{-Z_{\ell 0}}{2(Z_a + Z_{\ell 0})}$$

$$v_x = \frac{I_{cy+}^{m,n} + I_{cy+}^{m+1,n} + I_{cy-}^{m,n} + I_{cy-}^{m+1,n}}{2 \cdot \omega_0 C_1}$$

$$I_{cy+} = \frac{Z_\ell(v_1 - v_2)}{(Z_{\ell 0} + Z_a)(Z_\ell + Z_c)} + \frac{2(2Z_{\ell 0} + Z_a)}{bb} v_{\ell 1} + \frac{2Z_c Z_\ell}{bb(Z_c + Z_\ell)} v_{\ell 2}$$
$$- \frac{2(2Z_{\ell 0} + Z_a + Z_\ell)}{bb} v_{c1} + \frac{2Z_\ell^2}{bb(Z_c + Z_\ell)} v_{c2} + \frac{Z_\ell \cdot v_x}{2(Z_{\ell 0} + Z_a)(Z_\ell + Z_c)} \qquad {}_k v_{\ell 1}^i = -_{k-1} v_{\ell 1}^r$$

$$I_{cy-} = \frac{Z_\ell(v_2 - v_1)}{(Z_{\ell 0} + Z_a)(Z_\ell + Z_c)} + \frac{2Z_c Z_\ell}{bb(Z_c + Z_\ell)} v_{\ell 1} + \frac{2(2Z_{\ell 0} + Z_a)}{bb} v_{\ell 2}$$
$$+ \frac{2Z_\ell^2}{bb(Z_c + Z_\ell)} v_{c1} - \frac{2(2Z_{\ell 0} + Z_a + Z_\ell)}{bb} v_{c2} - \frac{Z_\ell \cdot v_x}{2(Z_{\ell 0} + Z_a)(Z_\ell + Z_c)} \qquad {}_k v_{c1}^i = {}_{k-1} v_{c1}^r$$

$$Z_c = \frac{\Delta\ell}{2C_1 v_{\ell 0}} \qquad Z_\ell = \frac{2L_1 v_{\ell 0}}{\Delta\ell} \qquad {}_k v_{c2}^i = {}_{k-1} v_{c2}^r \qquad {}_k v_{\ell 2}^i = -{}_{k-1} v_{\ell 2}^r$$

Similar to the situation in modeling metamaterials with inter-cell network, four more inter-cell boundary scattering networks are needed, These networks are derived in the following section.

At the present time, this gyromagnetic modeling approach has only been implemented in 2D TLM. The implementation has been validated by comparing the simulation results with analytical calculations and with data taken from the literature. Following the procedure in the previous chapter and in [96], this gyromagnetic inter-cell concept can be extended to 3D SCN TLM with some modifications.

7.4 Boundary conditions for gyromagnetic materials

7.4.1 Electric boundary

The inter-cell network for gyromagnetic material at an electric boundary and its equivalent circuit in TLM are shown in Figure 7.4; the corresponding scattering matrix is given in equation (7.9).

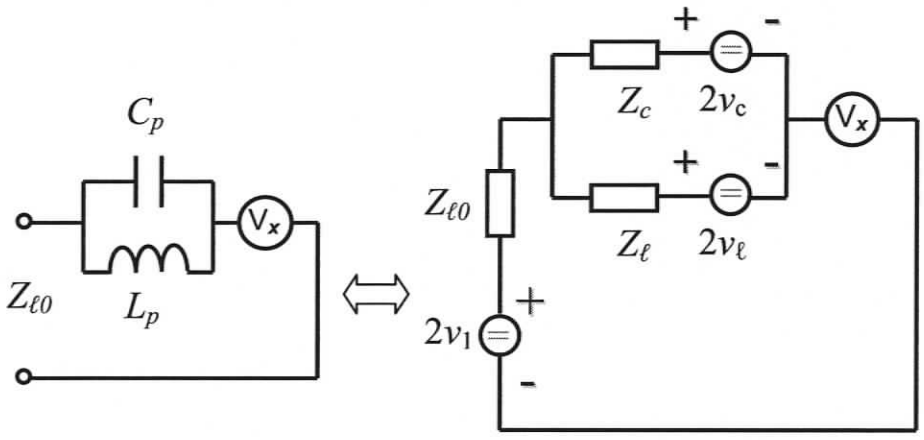

Figure 7.4 Electric boundary inter-cell network of gyromagnetic material and its equivalent circuit in TLM

$$\begin{bmatrix} v_1 \\ v_\ell \\ v_c \end{bmatrix}^r_k = \begin{bmatrix} e_{11} & e_{12} & e_{13} & e_{14} \\ e_{21} & e_{22} & e_{23} & e_{24} \\ e_{31} & e_{32} & e_{33} & e_{34} \end{bmatrix} \cdot \begin{bmatrix} v_1 \\ v_\ell \\ v_c \\ v_x \end{bmatrix}^i_k \tag{7.9}$$

where

$$Z_a = \frac{Z_c Z_\ell}{(Z_c + Z_\ell)} \qquad ee = Z_c Z_{\ell 0} + Z_\ell Z_{\ell 0} + Z_\ell Z_c$$

$$e_{11} = \frac{Z_a - Z_{\ell 0}}{Z_a + Z_{\ell 0}} \qquad e_{21} = e_{31} = \frac{2Z_a}{Z_a + Z_{\ell 0}}$$

$$e_{12} = e_{32} = \frac{2Z_{\ell 0} Z_c}{ee} \qquad e_{22} = \frac{(Z_c Z_{\ell 0} - Z_\ell Z_{\ell 0} - Z_\ell Z_c)}{ee}$$

$$e_{13} = e_{23} = \frac{2Z_{\ell 0} Z_\ell}{ee} \qquad e_{33} = \frac{(Z_\ell Z_{\ell 0} - Z_c Z_{\ell 0} - Z_\ell Z_c)}{ee}$$

$$e_{14} = \frac{-Z_{\ell 0}}{Z_a + Z_{\ell 0}} \qquad e_{24} = e_{34} = \frac{Z_a}{Z_a + Z_{\ell 0}} \qquad v_x = \frac{I^{m,n}_{cy+} + I^{m,n}_{cy-}}{2 \cdot \omega_0 C_1}$$

$$I^{m,n}_{cy-} = \frac{2Z_\ell v_1}{(Z_{\ell 0} + Z_a)(Z_\ell + Z_c)} + \frac{2Z_{\ell 0}}{ee} v_\ell + \frac{2(Z_{\ell 0} + Z_\ell)}{ee} v_c - \frac{Z_\ell \cdot v_x}{(Z_{\ell 0} + Z_a)(Z_\ell + Z_c)}$$

(for boundary located at y- position)

$$I^{m,n}_{cy+} = \frac{2Z_\ell v_1}{(Z_{\ell 0} + Z_a)(Z_\ell + Z_c)} + \frac{2Z_{\ell 0}}{ee} v_\ell - \frac{2(Z_{\ell 0} + Z_\ell)}{ee} v_c + \frac{Z_\ell \cdot v_x}{(Z_{\ell 0} + Z_a)(Z_\ell + Z_c)}$$

(for boundary located at y- position)

$$Z_c = \frac{\Delta \ell}{2C_{ssx} v_{\ell 0}}, \qquad {}_k v^i_c = {}_{k-1} v^r_c, \qquad Z_\ell = \frac{2L_{ppx} v_{\ell 0}}{\Delta \ell}, \qquad {}_k v^i_\ell = -{}_{k-1} v^r_\ell$$

7.4.2 Magnetic boundary

Because the inter-cell network for gyromagnetic material is a series network, the whole inter-cell network at a magnetic boundary is open-circuited. Therefore it has no effect on the computation process.

7.4.3 Absorbing boundary

The inter-cell network for gyromagnetic material at an absorbing boundary, and its equivalent circuit in TLM are shown in Figure 7.5; the corresponding scattering matrix is given in equation (7.10). Here Z_{0m} is the characteristic impedance of the waveguide at a given frequency and for a particular mode.

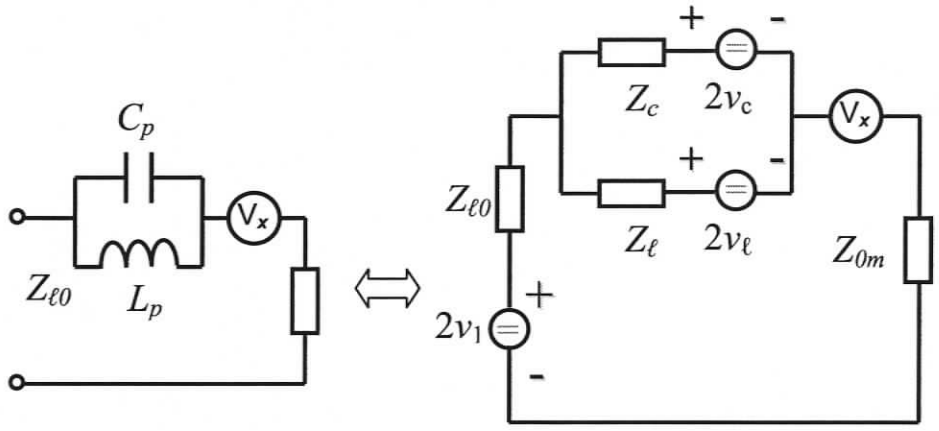

Figure 7.5 Absorbing boundary inter-cell network and its equivalent circuit in TLM.

$$\begin{bmatrix} v_1 \\ v_\ell \\ v_c \end{bmatrix}^r_k = \begin{bmatrix} a_{11} & a_{12} & a_{13} & a_{14} \\ a_{21} & a_{22} & a_{23} & a_{24} \\ a_{31} & a_{32} & a_{33} & a_{34} \end{bmatrix} \cdot \begin{bmatrix} v_1 \\ v_\ell \\ v_c \\ v_x \end{bmatrix}^i_k \tag{7.10}$$

where

$$Z_a = \frac{Z_c Z_\ell}{(Z_c + Z_\ell)} \qquad aa = Z_c Z_{0m} + Z_c Z_0 + Z_\ell Z_{0m} + Z_\ell Z_{\ell 0} + Z_\ell Z_c$$

$$a_{11} = \frac{Z_a + Z_{0m} - Z_{\ell 0}}{Z_a + Z_{0m} + Z_{\ell 0}} \qquad a_{21} = a_{31} = \frac{2Z_a}{Z_a + Z_{0m} + Z_{\ell 0}}$$

$$a_{12} = \frac{2Z_{\ell 0} Z_c}{aa} \qquad a_{22} = \frac{(Z_c Z_{0m} + Z_c Z_{\ell 0} - Z_\ell Z_{0m} - Z_\ell Z_{\ell 0} - Z_\ell Z_c)}{aa}$$

$$a_{13} = \frac{2Z_{\ell 0} Z_\ell}{aa} \qquad a_{33} = \frac{(Z_\ell Z_{0m} + Z_\ell Z_{\ell 0} - Z_c Z_{0m} - Z_c Z_{\ell 0} - Z_\ell Z_c)}{aa}$$

$$a_{23} = \frac{2(Z_{\ell 0} + Z_{0m})Z_\ell}{aa} \qquad a_{32} = \frac{2(Z_{\ell 0} + Z_{0m})Z_c}{aa}$$

$$a_{24} = a_{34} = \frac{Z_a}{Z_a + Z_{0m} + Z_{\ell 0}} \qquad a_{14} = \frac{-Z_{\ell 0}}{Z_a + Z_{0m} + Z_{\ell 0}} \qquad v_x = \frac{I_{cy+}^{m,n} + I_{cy-}^{m,n}}{2 \cdot \omega_0 C_1}$$

$$I_{cy-}^{m,n} = \frac{2Z_\ell v_1}{(Z_{\ell 0} + Z_{0m} + Z_a)(Z_\ell + Z_c)} + \frac{2(Z_{\ell 0} + Z_{0m})}{aa} v_\ell + \frac{2(Z_{\ell 0} + Z_{0m} + Z_\ell)}{aa} v_c$$
$$- \frac{Z_\ell \cdot v_x}{(Z_{\ell 0} + Z_{0m} + Z_a)(Z_\ell + Z_c)}$$

(for boundary located at y- position)

$$I_{cy+}^{m,n} = \frac{2Z_\ell v_1}{(Z_{\ell 0} + Z_{0m} + Z_a)(Z_\ell + Z_c)} + \frac{2(Z_{\ell 0} + Z_{0m})}{aa} v_\ell - \frac{2(Z_{\ell 0} + Z_{0m} + Z_\ell)}{aa} v_c$$
$$+ \frac{Z_\ell \cdot v_x}{(Z_{\ell 0} + Z_{0m} + Z_a)(Z_\ell + Z_c)}$$

(for boundary located at y- position)

$$Z_c = \frac{\Delta \ell}{2C_{ssx} v_{\ell 0}} \qquad Z_\ell = \frac{2L_{ppx} v_{\ell 0}}{\Delta \ell} \qquad {}_k v_\ell^i = -_{k-1} v_\ell^r \qquad {}_k v_c^i = {}_{k-1} v_c^r$$

7.5 Simulation results

The above gyromagnetic model has been implemented. A number of canonical cases are used to validate the theory and implementation. In the first test example, the dominant mode (TE_{10}) phase constant in a ferrite filled rectangular waveguide is computed. Table 7.1 shows that the computed results agree well with exact analytical results and results from the literature. Figure 7.6 depicts the waveguide used in the example; the material properties of the ferrite are assumed as $\varepsilon_r = 9$, $4\pi M_s = 2000$ Gauss, and $H_i = 200$ Oersted as in [89]. The width of the waveguide is 22.86 mm. The wave propagates in the x-direction and the DC biasing is applied in the z-direction.

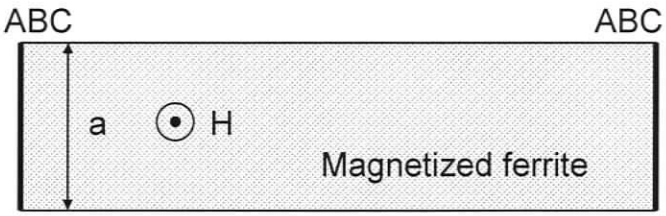

Figure 7.6 Top view of a rectangular waveguide comprising magnetized ferrite.

Freq. (GHz)	β (rad/m) (analytical)	β (rad/m) (Our TLM data)	Error in TLM (our data) (%)	Error in FDTD [86] (%)
6.63	83.075	83.664	0.71	-0.16
6.911	151.462	152.248	0.52	-1.85
7.207	200.938	202.683	0.87	-1.16
7.604	254.303	255.908	0.63	-0.42
8.003	300.294	303.536	1.08	0.15
8.601	361.278	365.302	1.11	0.36

Table 7.1 Simulation results for the phase constant, compared with theoretical calculations and simulation results from the literature. Here a cell size of 2.286 mm is used in both TLM and FDTD.

In the second example the phase constant of the dominant mode is calculated in the same rectangular waveguide when partially filled with magnetized ferrite as shown in Figure 7.7 (a); the magnetized ferrite occupies one-third of the width. The structure is discretized with a mesh of 0.3048 mm resolution. Like in the previous example, the DC magnetization biasing is in the z-direction. The results are compared with the exact theoretical calculations in Table 7.2.

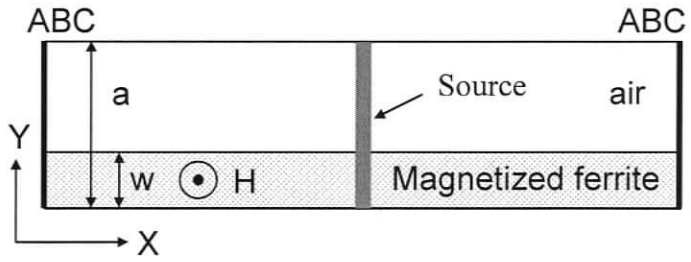

Figure 7.7 Top view of a rectangular waveguide partially loaded with magnetized ferrite (the following waveguide and ferrite parameters were assumed: a = 22.86 mm, w=a/3, $\varepsilon_r = 9$, $4\pi M_s = 2000$ Gauss, and $H_i = 200$ Oersted).

	Freq. (GHz)	β (rad/m) (analytical)	β (rad/m) (calculated)	Error (%)
Forward (+x)	6.696	+200	+201.11	0.56
	7.669	+300	+299.48	-0.17
	10.57	+500	+498.23	-0.35
Backward (-x)	7.376	-100	-99.11	-0.89
	8.188	-200	-200.14	0.07
	9.128	-300	-298.76	-0.41
	11.32	-500	-502.78	0.56

Table 7.2 Forward and backward phase constants in partially filled waveguide, compared with theoretical calculations.

In the third example, the nonreciprocal properties of gyromagnetic materials are used to validate the modeling algorithm. A 7.669GHz sinusoidal wave is launched at the center of a rectangular waveguide partially filled with magnetized ferrite biased in the z-direction. The waveguide contains 400 unit cells along the propagation direction and is terminate by absorbing boundaries at both ends as shown in Figure 7.7 (b). A snapshot of the electric field distribution in longitudinal direction at time step $k = 5000$ is shown in Figure 7.8. It is clear that in the same waveguide, the phase constants are different for forward and backward wave propagation.

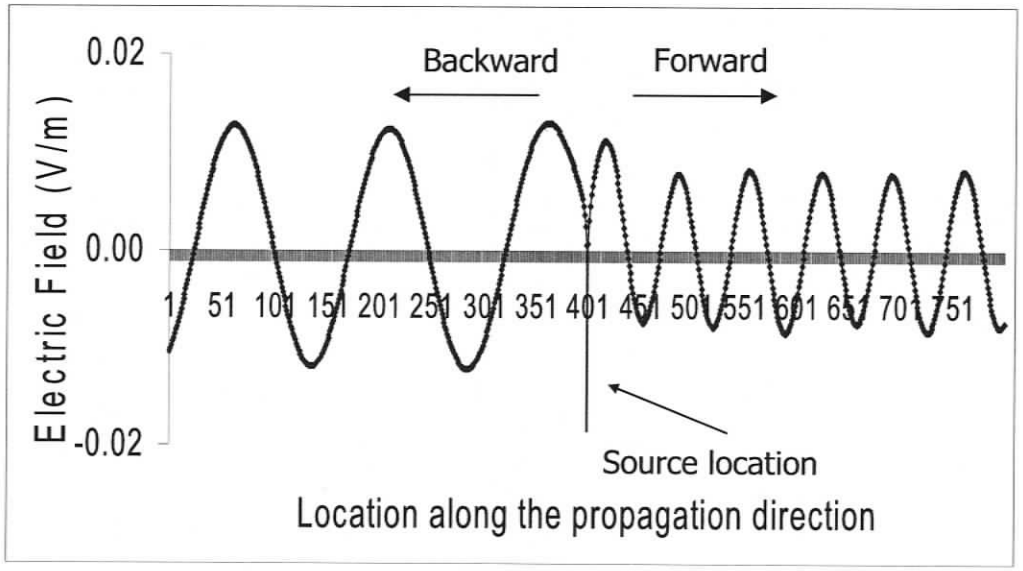

Figure 7.8 Field distribution in a partially ferrite-loaded rectangular waveguide. The source is placed at the center, launching a forward and a backward wave.

7.6 Conclusions

A new TLM model for gyromagnetic materials using inter-cell networks has been developed. The nonreciprocal and dispersive properties are introduced by means of lumped parallel capacitor-inductor resonators and current-controlled voltage sources. This approach is different from the conventional stub model because the magnetic properties are realized using inter-cell networks. The theory and implementation of the new model have been validated by comparing computed data with analytical results for phase constants in completely and partially ferrite-filled rectangular waveguides. The modeling error is compatible with that reported in the literature and is within the typical error affecting the numerical modeling of regular materials. The correctness of the theory and implementation has been further confirmed by the nonreciprocal result obtained in one of the test cases.

Chapter 8

Conclusions and Further Work

8.1 Conclusions

Time domain modeling of electromagnetic problems and the design of microwave and high speed circuits are very challenging and complex tasks. The principal objectives of this dissertation are therefore to reduce the computational burden of field computations without decreasing the accuracy of numerical results, and to enhance the TLM method such that it can be used to solve more complex and hybrid problems. More specifically, this dissertation is devoted to the study of multilevel modeling techniques for time domain analysis of microwave and high speed circuits that can overcome some of the difficulties. The following novel contributions have been made in the course of this research.

1) A new methodology for singularity correction in TLM has been developed. In this approach the permittivity and permeability in the cells close to a field singularity are modified by a scalar correction factor. This correction turns out to be equally effective for quasi-TEM, TE-, TM- and hybrid field excitations of the singularity. Validation results show that the proposed correction method reduces the singularity error by typically one order of magnitude without significant penalty in terms of computational burden. This approach is applicable to structures with both homogeneous and inhomogeneous material properties in the singularity region.

2) A bridge linking circuit simulation and field analysis in the time-domain has been created, implemented and tested. It employs two distinct procedures, which are the embedding of current-coupled lumped networks into three-dimensional TLM field models, and the use of an Analog Behavioral Model (ABM) module that allows the introduction of field-based device modules into circuit simulators such as PSPICE. The

embedding technique represents a powerful tool for reduced-order representation of substructures within a space-time electromagnetic field model. The Analog Behavioral Model technique offers the capacity to model complex systems containing components represented at various levels, such as lumped circuits, distributed components and field-based models.

3) A general inter-cell network framework for TLM modeling of materials with complex electromagnetic properties have been developed, implemented and tested. This framework provides allows the embedding of linear/nonlinear lumped or distributed features in the field space and the modeling of materials without the need to modify the node scattering matrix. The properties of the inter-cell network can be described by various means, such as equivalent circuits, differential equations, behavioral models, experimental data, or even nonlinear SPICE modules. This inter-cell network modeling approach is a very useful tool for investigating the characteristics of components and devices containing gyromagnetic materials.

4) One particularly successful application of the inter-cell network framework developed in this dissertation is a new 3D model of metamaterials. The simulation results demonstrate the unusual properties of metamaterials with negative refractive index as predicted by the theory. The general dispersion relation for periodic transmission line networks with embedded lumped elements and reactive stubs has been formulated as a singular value equation and solved numerically using Matlab's symbolic matrix solver. Since in most practical simulations the direction of wave propagation is not known, the dispersion error margin can be predicted by evaluating approximate closed-form expressions for axial propagation. Such expressions have been presented and validated in this dissertation as well; they were derived using lumped embedded elements and are equivalent to expressions available in the literature.

5) A new 2D TLM model for gyromagnetic materials using inter-cell networks has been developed and implemented. The nonreciprocal and dispersive properties of the materials are introduced in the TLM cells by means of lumped parallel capacitor-inductor resonators and current controlled voltage sources. The new model has been validated by comparing the computed data with analytical results for phase constants in rectangular

waveguides completely and partially filled with ferrite. The modeling error is compatible with that reported in the literature and is within the typical error affecting the numerical modeling of regular materials. The nonreciprocal behavior of the gyromagnetic material is clearly demonstrated by the differences in field distribution and phase velocity of forward and backward waves in a partially filled waveguide.

8.2 Future work

The approaches and models developed in this dissertation can be extended to other time-domain methods and to a large variety of material modeling and applications. Meanwhile the following further investigations need to be carried out.

Firstly, further investigation of the convergence of the singularity correction method presented in this dissertation should be carried out. The correction procedure is based on the *a priori* knowledge that the singular field distribution is quasi-static, and in principle, the energy at the singularity remains finite, even though some of the field components become infinite at sharp edges and corners. The local character of the singularity fields implies that they are independent of boundary conditions several mesh cells away. Although no instabilities have been observed in the simulations performed so far, even when run for long simulation times, it should be pointed out that when more than one singularity exist and are too close to each other, some concerns about the convergence of the procedure may arise

The second objective of further investigations will be directed towards the implementation of links between commercial circuit simulators such as PSPICE, and time domain field solvers based on the TLM method. In this dissertation a new avenue has been opened for exchanging information between circuit simulation and full-wave field analysis in real time. Although a number of medium-sized examples have been tested, the problems involving very large scale circuits due to the limitations of the free SPICE version we used in this thesis project have not been tackled.

Thirdly, the inter-cell network framework is a general method for modeling material properties, or for introducing other features into field analysis by means of lumped element networks, differential equations, behavior models, etc. The metamaterial model

has been implemented in the commercial TLM-based package, MEFiSTo-3D, which is being used in the industry and academic arenas. The integration of the inter-cell metamaterial model with a general electromagnetic field solver tool will enable the exploration of properties and characteristics of a large variety of components containing metamaterials and greatly facilitate future investigations and technology development.

Finally, the magnetized ferrite model presented in this dissertation is based on 2D TLM, so it can only be employed in 2D simulations. Although the 2D model can solve a large number of electromagnetic problems, extension to a fully 3D magnetized ferrite model should be pursued with the goal to model 3D gyromagnetic materials and devices.

Bibliography

[1] D. Lukashevich, A. Cangellaris, and P. Russer, "Transmission line matrix method reduced order modeling," *in IEEE MTT-S International Microwave Symposium Digest,* Vol. 2, pp. 1125 - 1128, 2003.

[2] G. Kron, "Equivalent Circuits to Represent the Electromagnetic Field Equations," *Physical Review*, vol. 64, pp. 126–128, Aug. 1943.

[3] J. R. Whinnery and S. Ramo, "A New Approach to the Solution of High Frequency Field Problems", *Proc. I. R.E.*, Vol. 32, pp 284–288, May 1944.

[4] J. R. Whinnery, C. Concordia, W. Ridgway, and G. Kron, "Network Analyzer Studies of Electromagnetic Cavity Resonators", *Proc. I. R.E.*, Vol. 32, pp 360–367, June 1944.

[5] P. B. Johns and R. L. Beurle, "Numerical Solution of 2-Dimensional Scattering problems using a Transmission Line Matrix, *Proc. IEE,* Vol. 118, pp. 1203–1208, Sep. 1971.

[6] S. Akhtarzad and P. B. Johns, "Solution of 6-component electromagnetic fields in three space dimensions and time by the T.L.M. method," *Electron. Lett.,* Vol. 10, No. 25/26, pp. 535–537, Dec. 1974.

[7] P. B. Johns, "A Symmetrical Condensed Node for the TLM Method", *IEEE Transactions on Microwave Theory Tech.*, Vol. MTT-35, No. 4, pp 370–377, Apr. 1987.

[8] W. J. R. Hoefer and P. P.M. So, *The Electromagnetic Wave Simulator.* John Wiley & Sons, New York, 1991.

[9] W. J. R. Hoefer, "The Transmission Line Matrix method—Theory and applications," *IEEE Transactions on Microwave Theory Tech.*, vol. MTT-33, pp. 882-893, Oct. 1985.

[10] D. G. Swanson. Jr. and W. J. R. Hoefer, *Microwave Circuit Modeling Using Electromagnetic Field Simulation.* Artech House, Boston • London, 2003, chapter 3 and 7.

[11] T. Itoh, *Numerical techni-ques for Microwave and millimeter.* John Wiley & Sons, New York, 1989, chapter 8.

[12] C. Christopoulos, *The Transmission-Line Modeling Method TLM.* IEEE Press, New York, 1995.

[13] G. Tardioli and W. J. R. Hoefer, "Derivation of the SCN Node Scattering Matrix from the Integral Formulation of Maxwell's Equations", *Proceeding of the Second International Workshop on Transmission Line (TLM) Modeling*, pp. 36-47 Munich, Germany, Oct. 1997.

[14] P. P. M. So, *Modelling of Complex Electromagnetic Structures with TLM — Theory and Practice.* Ph. D. Dissertation, University of Victoria, 1996.

[15] J. S. Nielsen and W. J. R. Hoefer, "Generalized dispersion analysis and spurious modes of 2-D and 3-D TLM formulations", *IEEE Transactions on Microwave Theory and Techniques*, Vol. 41, pp. 1375 – 1384, Aug. 1993.

[16] V. Trenkic, T. M. Benson and C. Christopoulos, "Dispersion analysis of a TLM mesh using a new scattering matrix formulation", *IEEE Microwave and Guided Wave Lett.*, pp. 79 – 80, Mar. 1995.

[17] L.R.A.X. Menezes, and W. J.R. Hoefer, "Accuracy of TLM Solutions of Maxwell's Equations," *IEEE Transaction on Microwave Theory and Tech.*, vol. 44, pp. 2512-2518, Dec. 1996.

[18] T. Kashiwa, M. Uchiya, K. Suzuki, and Y. Kanai, "FDTD analysis of Microwave Circuits Using Edge Condition," *IEEE Transaction on Magnetics*, Vol. 38, pp. 705-708, Mar. 2002.

[19] R. E. Collin, *Field Theory of Guided Waves.* IEEE Press, New York, 1991, 2nd edition.

[20] N.R.S. Simons, R. Siushansian, J. LoVetri, and M. Cuhaci, "Comparison of the transmission-line matrix and finite-difference time-domain methods for a problem containing a sharp metallic edge" *IEEE Transactions on Microwave Theory and Tech.*, Vol. 47 , pp. 2042-2045, Oct. 1999.

[21] J.L. Herring, C. Christopoulos, "Multigrid transmission-line modeling method for solving electromagnetic field problems," *Electronics Letters*, Vol. 27, Issue 20, pp. 1794-1795, Sep. 1991.

[22] P. Sewell, J. Wykes, A. Vukovic, D.W.P. Thomas, T.M. Benson, and C. Christopoulos, "Multi-grid interface in computational electromagnetics," *Electronics Letters*, Vol. 40, pp.162-163, Feb. 2004.

[23] S. A. Meade and C. J. Railton, "Efficient implementation of the spectral domain method including precalculated corner basis functions," *IEEE Transactions on Microwave Theory and Tech.*, Vol.42 , pp.1678 – 1684, Sep. 1994.

[24] N.-H. Huynh and W. Heinrich, "FDTD accuracy improvement by incorporation of 3D edge singularities," *in IEEE MTT-S International Microwave Symposium Digest*, Vol.4, pp.1573 – 1576, 1999.

[25] T. I. Kosmanis, N. V. Kantartzis, and T. D. Tsiboukis, "A hybrid FDTD wavelet-Galerkin technique for the numerical analysis of field singularities inside waveguides," *IEEE Transactions on Magnetics*, Vol.36, pp. 902 - 906, July 2000.

[26] S. M. Foroughipour and K. P. Esselle, "The theory of a singularity-enhanced FDTD method for diagonal metal edges," *IEEE Transactions on Antennas and Propagation*, Vol.51, pp.312 – 321, Feb. 2003.

[27] G. Tardioli, L. Cascio, M. Righi, and W. J.R. Hoefer, "Special 3D-TLM corner nodes for singular field regions," *in IEEE MTT-S International Microwave Symposium Digest*, pp.317-320, Vol. 1, 1997.

[28] J. L. Herring and W.J.R Hoefer, "Compensation of coarseness error in TLM modeling of microwave structures with the symmetrical condensed node," *in IEEE MTT-S International Microwave Symposium Digest*, pp. 23-26, 1995.

[29] M. Celuch-Marcysiak, "Local stereoscopic field singularity models for FDTD analysis of guided wave problems," *in IEEE MTT-S International Microwave Symposium Digest*, Vol.2 , pp.1137 - 1140, 2003.

[30] L. Cascio, G. Tardioli, T. Rozzi, and W. J.R. Hoefer, "A Quasi-static Modification of TLM at Knife edge and 90° wedge singularities," *in IEEE MTTS International Microwave Symposium Digest*, pp.443-446, 1996.

[31] C. J. Railton, "The Inclusion of Fringing Capacitance and Inductance in FDTD for the Robust Accurate Treatment of Material Discontinuities," *in IEEE MTT-S International Symposium Digest*, pp.391-394, 2000.

[32] U. Mueller, P. So and W. J.R. Hoefer, "The Compensation of coarseness error in 2D TLM modeling of microwave structures," *in IEEE MTT-S International Microwave Symposium Digest*, pp.373-376, 1992.

[33] I.J. Craddock, C.J. Railton, "A new technique for the stable incorporation of static field solutions in the FDTD method for the analysis of thin wires and narrow strips," *IEEE Transactions on Microwave Theory and Tech.*, Vol. 46 , pp.1091-1096, Aug. 1998.

[34] S.-C. Wu, N.G. Alexopoulos and O. Fordham, "Feeding structure contribution to radiation by patch antennas with rectangular boundaries", *IEEE Transactions on Antennas and Propagation*, Vol. 40, pp. 1245 – 1249, Oct. 1992.

[35] T. Kashiwa, M. Uchiya, K. Suzuki, and Y. Kanai, "FDTD analysis of microwave circuits using edge condition", *IEEE Transactions on Magnetics*, Vol. 38, pp. 705 – 708, Mar. 2002.

[36] W. Sui, D. A. Chirstensen and C. H. Durney, "Extending the two-dimensional FD-TD method to hybrid electromagnetic systems with active and passive limped elements," *IEEE Transaction on Microwave Theory and Tech.*, vol. 40, pp. 724–730, Apr. 1992.

[37] V. A. Thomas, M. E. Jones, M. Piket-May, A. Taflove, and E. Harrigan, "The use of SPICE lumped circuits as sub-grid models for FDTD analysis," *IEEE Microwave Guided Wave Lett.*, Vol. 4, pp. 141–143, May 1994.

[38] C.-N. Kuo, R.-B. Wu, B. Houshm and T. Itoh, "Modeling of microwave active devices using the FDTD analysis based on the voltage-source approach," *IEEE Microwave Guided Wave Lett.*, Vol. 6, no. 5, pp. 199–201, May 1996.

[39] P. Russer, P. P. M. So and W. J.R. Hoefer, "Modeling of nonlinear active regions in TLM," *IEEE Microwave and Guided Wave Lett.*, Vol.1, pp.10 - 13, Jan. 1991.

[40] L. Cascio, and W. J.R. Hoefer, "Modification of the 3D-TLM scattering matrix to model nonlinear devices in graded and heterogeneous regions," *in IEEE MTT-S International Microwave Symposium Digest*, Vol. 2, pp.897 – 900, 1998.

[41] A. Nishizawa, G. Kobidze, and S. Tanabe, "Hybrid FDTD-SPICE analysis of radiated emission from PCB with integrated circuits," *in IEEE International Symposium on Electromagnetic Compatibility*, Vol.1, pp. 559 – 563, 2001.

[42] N. Orhanovic, R. Raghuram, N. Matsui, "Full wave analysis of planar interconnect structures using FDTD-SPICE," *in Electronic Components and Technology Conference Proceedings,* pp. 489 – 494, 2001.

[43] S. K. Ip and F.Y. Chang, "Extending SPICE with FDTD and generalized characteristic model for coupled microstrip lines simulation," *in IEEE MTT-S International Microwave Symposium Digest*, Vol. 3, pp. 2077 - 2080, 2003.

[44] P. P.M. So and W. J.R. Hoefer, "A general framework for SPICE-TLM inter-connection," *in IEEE MTT-S International Microwave Symposium Digest*, Vol. 2, pp. 1123 -1126, June 2002.

[45] J. W. Park, P.P.M. So and W. J.R. Hoefer, "Lumped and Distributed Device Embedding Techniques in Time Domain TLM Field Models," *in IEEE MTT-S International Microwave Symposium Digest*, pp. 2047-2050, June 2001.

[46] L. Cascio, G. Tardioli, and W. J.R. Hoefer, "Modeling of nonlinear active and passive devices in three dimensional TLM networks," *in IEEE MTT-S International Microwave Symposium Digest*, pp. 383-386, 1997.

[47] P. P.M. So and W. J.R. Hoefer, "A TLM-SPICE interconnection framework for coupled field and circuit analysis in the time domain," *IEEE Transaction on Microwave Theory and Tech.*, Vol. pp. 2728 -2733, Dec. 2002.

[48] W. Eberle, G. Vandersteen, P. Wambacq, S. Donnay, G. Gielen, and H. De Man, "Behavioral modeling and simulation of a mixed analog/digital automatic gain control loop in a 5 GHz WLAN receiver," *Europe Conference and Exhibition on Design, Automation and Test*, pp. 642 – 647, 2003.

[49] G. G. E Gielen, "Modeling and analysis techniques for system-level architectural design of telecom front-ends," *IEEE Transaction on Microwave Theory and Techniques,* Vol. 50, pp. 360 – 368, Jan. 2002.

[50] N. Jankovic, T. Pesic and J. Karamarkovic, "1D physically based non-quasi-static analog behavioral BJT model for SPICE," *23rd International Conference on Microelectronics*, Vol. 2, pp. 463 – 468, May 2002.

[51] Wilson, I.M, "Analog behavioral modeling using PSPICE," *Proceedings of the 32nd Midwest Symposium on Circuits and Systems,* vol.2, pp. 981-984, Aug. 1989.

[52] Cordon W. Roberts and Adel S. Sedra, SPICE, 2ed, Oxford University Press, 1997.

[53] Cotorogea, M, "Using analog behavioral modeling in PSpice for the implementation of subcircuit-models of power devices," *IEEE International Power Electronics Congress*, pp.158 – 163, Oct. 1998.

[54] George R. Cooper and Clare D. McGillem, *Methods of Signal and System Analysis,* Holt, Rinehart and Winston, Inc., 1967.

[55] MicroSim Corporation, "PSpice A/D & Basics + Circuit Analysis Software User's Guide," Version 8.0, June, 1997.

[56] W.J.R. Hoefer, "The Transmission Line Matrix method—Theory and applications," *IEEE Transaction on Microwave Theory and Tech.*, vol. MTT-33, pp. 882-893, Oct. 1985.

[57] P. B. Johns, "A symmetrical condensed node for the TLM method," *IEEE Transaction on Microwave Theory and Tech.*, vol. 35, pp. 370-377, Apr. 1987.

[58] P. P.M. So and W. J.R. Hoefer, "Time Domain TLM Modeling of Metamaterials with Negative Refractive Index," *in IEEE MTT-S International Microwave Symposium Digest*, pp. 1779-1782, 2004.

[59] H. Du, P. P. M. So, and W. J. R. Hoefer, "Modeling of materials with negative refractive index using TLM 3D SCN node and inter-cell networks," *in Proceedings of The 10th International Symposium on Antenna Technology and Applied Electromagnetics,* pp. 80-83, Ottawa, Canada, 2004.

[60] G. V. Eleftheriades, A. K. Iyer, and P. C. Kremer. "Planar Negative Refractive Index Media Using Periodically L–C Loaded Transmission Lines," *IEEE Transaction on Microwave Theory and Tech.,* Vol. 50, pp. 2702-2712, Dec. 2002.

[61] C. Christopoulos, *The Transmission-Line Modeling Method TLM.* IEEE Press, New York, 1995.

[62] J. S. Nielsen and W. J. R. Hoefer, "A Complete Dispersion Analysis of the Condensed Node TLM Mesh", *IEEE Transactions on Magnetics*, Vol. 27, pp. 3982-3985, Sep. 1991.

[63] J. S. Nielsen and W. J. R. Hoefer, "Generalized Dispersion Analysis and Spurious Modes of 2-D and 3-D TLM Formulations", *IEEE Transactions on Microwave Theory and Tech.*, vol.41, pp. 1375-1384, Aug. 1993.

[64] W. J. R. Hoefer, H. Du and P. P. M. So, "Wave properties of computational TLM models of metamaterials with negative refractive index", *International Journal of*

Numerical Modelling: Electronic Networks, Devices and Fields, pp. 119-139, Vol.19, Mar.-Apr. 2006.

[65] N. Engheta, "Metamaterials with Negative Permittivity and Permeability: Background, Salient Features, and New Trends", *in IEEE MTT-S International Microwave Symposium Digest*, pp.187 – 190, 2003.

[66] V. G. Veselago, "The electrodynamics of substances with simultaneously negative values of ε and μ," *Sov. Phys.—Usp.*, Vol. 10, pp. 509–514, Jan.–Feb. 1968.

[67] A. Lai, C. Caloz and T. Itoh, "Composite right/left-handed transmission line metamaterials," *IEEE Microwave Magazine*, pp. 34-50, Sep. 2004.

[68] R. Islamand and G. V. Eleftheriades, "Phase-agile branch-line couplers using metamaterial lines," *IEEE Microwave and Wireless Components Letters*, Vol. 14, pp. 340-342, July 2004.

[69] J. B. Pendry and D. R. Smith, "Reversing light: Negative refraction," *Physics Today*, pp.37-44, June 2003.

[70] D. R. Smith, W. J. Padilla, D. C. Vier, S. C. Nemat-Nasser, and S. Schultz, "Composite medium with simultaneously negative permeability and permittivity," *Phys. Rev. Lett.*, vol. 84, pp. 4184–4187, May 2000.

[71] R. A. Shelby, D. R. Smith, and S. Schultz, "Experimental verification of a negative index of refraction," *Science*, vol. 292, pp. 77–79, Apr. 2001.

[72] C. Caloz, H. Okabe, T. Iwai, and T. Itoh, "Transmission line approach of left-handed (LH) materials," *USNC/URSI National Radio Science Meeting*, Vol. 1, p. 39, 2002.

[73] A. K. Iyer and G. V. Eleftheriades, "Negative refractive index metamaterials supporting 2-D waves," *in IEEE MTT-S International Microwave Symposium Digest*, Vol. 2, pp. 1067–1070, 2002.

[74] G. V. Eleftheriades, A. K. Iyer, and P. C. Kremer. "Planar Negative Refractive Index Media Using Periodically L–C Loaded Transmission Lines", *IEEE Transactions on Microwave Theory and Tech.,* Vol. 50, pp. 2702-2712, Dec. 2002.

[75] A. A. Oliner, "A periodic-structure negative-refractive-index medium without resonant elements," *in USNC/URSI Nat. Radio Science Meeting*, San Antonio, pp. 41, 2002.

[76] P.P.M. So and W. J.R. Hoefer, "Time Domain TLM Modeling of Metamaterials with Negative Refractive Index," *in IEEE MTT-S International Microwave Symposium Digest*, pp. 1779-1782, 2004.

[77] R. W. Ziolkowski, "Pulsed and CW Gaussian beam interactions with double negative metamaterial slabs," *Optics Express*, Vol. 11, pp. 662-681, Apr. 2003.

[78] D. Correia, and J.M. Jin, "Theoretical analysis of left-handed metamaterials using FDTD-PML method," *in Proceedings of the 2003 SBMO/IEEE MTT-S*

International, Microwave and Optoelectronics Conference, vol. 2, pp.1033 – 1036, Sep. 2003.

[79] W. J. R. Hoefer, P. P. M. So, D. Thompson and M. M. Tentzeris, "Topology and Design of Wide-Band 3D Metamaterials made of Periodically Loaded Transmission Line Arrays", *in IEEE MTT-S International Microwave Symposium Digest*, pp. 313-316, 2005.

[80] A. Grbic and G.V. Eleftheriades, "A 3-D Negative-Refractive–Index Transmission-Line Medium, *in IEEE Antennas and Propagation Society International Symposium Digest,* vol. 2A, pp.14 – 17, 3-8 July, 2005.

[81] P.P.M. So and W. J.R. Hoefer, "Time Domain TLM Modeling of Metamaterials with Negative Refractive Index," *in IEEE MTT-S International Microwave Symposium Digest*, pp. 1779-1782, 2004.

[82] P.P.M. So, H. Du, and W. J. R. Hoefer, "Modeling of Metamaterials with Negative Refractive Index Using 2D-Shunt and 3D-SCN TLM Networks," *IEEE MTT transaction on Microwave Theory and Tech*, pp. 1496- 1505 Apr., 2005.

[83] H. Du, P. P.M. So, and W. J. R. Hoefer, "Inter-Cell Scattering Framework in TLM for Modeling Material Properties," *in Proceedings of the 34th European Microwave Conference,* pp. 865-868, Oct., 2004.

[84] J. B. Pendry, "Negative refraction makes a perfect lens," *Phys. Rev. Lett.*, vol. 85, pp. 3966–3969, Oct. 2000.

[85] A. Grbic and G.V. Eleftheriades,"Sub-wavelength focusing using a negative-refractive-index transmission-line lens," *IEEE Antennas and Wireless Propagation Letters,* vol. 2, pp. 186-189, 2003.

[86] M. Okoniewski, and E. Okoniewska, "FDTD analysis of magnetized ferrites: a more efficient algorithm," *IEEE Microwave and Guided Wave Lett.,* vol. 4, pp. 169-171, June 1994.

[87] J. A. Pereda, L. A. Vielva, M. A. Solano, A. Vegas, and A. Prieto, "FDTD analysis of magnetized ferrites: application to the calculation of dispersion characteristics of ferrite-loaded waveguides," *IEEE Transactions on Microwave Theory and Tech.,* vol. 48, pp. 2397-2402, December 2000. vol. 43, pp. 350-357, February 1995.

[88] J. A. Pereda, L. A. Vielva, A. Vegas, and A. Prieto, "A treatment of magnetized ferrites using the FDTD method," *IEEE Microwave and Guided Wave Lett.,* vol. 3, pp. 136-138, May 1993.

[89] W. K. Gwarek, and A. Moryc, "An alternative approach to FD-TD analysis of magnetized ferrites," *IEEE Microwave and Wireless Components Letters,* vol. 14, pp. 331-333, July 2004.

[90] K. Kunz and R. Luebbers, *The Finite Difference Time Domain Method for Electromagnetics*, Orlando, FL: CRC Press, 1993, chapter 15.

[91] M. I. Yaich, and M. Khalladi, "An SCN-TLM model for the analysis of ferrite media," *IEEE Microwave and Wireless Components Letters,* vol. 13, pp. 217-219, June 2003.

[92] L. De Menezes, and W. J. R. Hoefer, "Modeling gyromagnetic media in symmetrical condensed node TLM," *in 12th Annual Review of Progress in Applied Computational Electromagnetics Digest*, vol. 1, pp. 294-301, Mar. 1996.

[93] J. Paul, C. Christopoulos, and D. W. P. Thomas, "Generalized material models in TLM-Part 2: Materials with anisotropic properties," *IEEE Transaction on Antennas Propagation*, vol. 47, pp. 1535–1542, Oct. 1999.

[94] D. M. Pozar, *Microwave Engineering*, New York: J. Wiley & Sons, 1998, chapter 9.

[95] H. Du, P. P. M. So, and W. J. R. Hoefer, "Transient Modeling of Gyromagnetic Materials with the TLM Inter-Cell Network Concept," *in IEEE MTT-S International Microwave Symposium Digest*, pp. 321-324, 2005.

[96] H. Du, P. P. M. So, and W. J. R. Hoefer, "Modeling of materials with negative refractive index using TLM 3D SCN node and inter-cell networks," *in Proceedings of the 2004 Antem*, pp. 80-83, July 2004.